Electron reconstruction and identification in the ATLAS experiment using the 2015 and 2016 LHC proton–proton collision data at √s =13 TeV

Aaboud, M., Aad, G., Abbott, B., Abbott, D. C., Abdinov, O., Abeloos, B., … Zwalinski, L.

2019.

Eur. Phys. J. C (2019) 79:639
https://doi.org/10.1140/epjc/s10052-019-7140-6

THE EUROPEAN PHYSICAL JOURNAL C

Regular Article - Experimental Physics

Electron reconstruction and identification in the ATLAS experiment using the 2015 and 2016 LHC proton–proton collision data at $\sqrt{s} = 13$ TeV

ATLAS Collaboration[⋆]

CERN, 1211 Geneva 23, Switzerland

Received: 14 February 2019 / Accepted: 17 July 2019 / Published online: 3 August 2019

Abstract Algorithms used for the reconstruction and identification of electrons in the central region of the ATLAS detector at the Large Hadron Collider (LHC) are presented in this paper; these algorithms are used in ATLAS physics analyses that involve electrons in the final state and which are based on the 2015 and 2016 proton–proton collision data produced by the LHC at $\sqrt{s} = 13$ TeV. The performance of the electron reconstruction, identification, isolation, and charge identification algorithms is evaluated in data and in simulated samples using electrons from $Z \to ee$ and $J/\psi \to ee$ decays. Typical examples of combinations of electron reconstruction, identification, and isolation operating points used in ATLAS physics analyses are shown.

Contents

1 Introduction

Stable particles that interact primarily via the electromagnetic interaction, such as electrons, muons, and photons, are found in many final states of proton–proton (pp) collisions at the Large Hadron Collider (LHC) located at the CERN Laboratory. These particles are essential ingredients of the ATLAS experiment's Standard Model and Higgs-boson physics programme as well as in searches for physics beyond the Standard Model. Hence, the ability to effectively reconstruct electrons[1] originating from the prompt decay of particles such as the Z boson, to identify them as such with high efficiency, and to isolate them from misidentified hadrons, electrons from photon conversions, and non-isolated electrons originating from heavy-flavour decays are all essential steps to a successful scientific programme.

The ATLAS Collaboration has presented electron-performance results in several publications since the start of the high-energy data-taking in 2010 [1–3]. The gradual increase in peak luminosity and the number of overlapping collisions (pile-up) in ATLAS has necessitated an evolution of the electron reconstruction and identification techniques. In addition, the LHC shutdown period of 2013–2014 brought a

⋆ e-mail: atlas.publications@cern.ch

[1] Throughout this paper, the term "electron" usually indicates both electrons and positrons.

new charged-particle detection layer to the centre of ATLAS and a restructuring of the trigger system, both of which impact physics analyses with electrons in the final state. These changes require a new benchmarking of electron-performance parameters. The electron efficiency measurements presented in this paper are from the data recorded during the 2015–2016 LHC pp collision run at centre-of-mass energy $\sqrt{s} = 13$ TeV. During the period relevant to this paper, the LHC circulated 6.5 TeVproton beams with a 25 ns bunch spacing. The peak delivered instantaneous luminosity was $\mathcal{L} = 1.37 \times 10^{34}$ cm^{-2} s^{-1} and the mean number of pp interactions per bunch crossing (hard scattering and pile-up events) was $\langle\mu\rangle = 23.5$. The total integrated luminosity [4] used for most of the measurements presented in this paper is 37.1 fb^{-1}. Another important goal of this paper is to document the methods used by the ATLAS experiment at the start of Run 2 of the LHC (2015 and beyond) to reconstruct, identify, and isolate prompt-electron candidates with high efficiency, as well as to suppress electron-charge misidentification. The methods presented here would be of value to other experiments with similar experimental conditions of fine granularity detection devices but also substantial inactive material in front of the active detector, or with significant activity from pile-up events.

The structure of the paper is described in the following, highlighting additions and new developments with respect to Ref. [3]. Section 2 provides a brief summary of the main components of the detector germane to this paper, with special emphasis on the changes since the 2010-2012 data-taking period. Section 3 itemises the datasets and simulated-event samples used in this paper. Given that the method for calculating efficiencies is common to all measurements, it is described in Sect. 4, before the individual measurements are presented. The algorithms and resulting measurements for electron reconstruction efficiencies are described in Sect. 5, including a detailed discussion of the Gaussian Sum Filter algorithm. Electron identification and the corresponding measurement of efficiencies are described in Sect. 6. New developments here include the optimisation based on simulated events and the treatment of electrons with high transverse momentum. The algorithms used to identify isolated electron candidates and the resulting measured benchmark efficiencies are published for the first time; these are presented in Sect. 7. This paper also presents detailed discussion of studies of the probability to mismeasure the charge of an electron; these are presented in Sect. 8. This section also includes a discussion of the sources of charge misidentification and a new Boosted Decision Tree algorithm that reduces the rate of charge-misidentified electrons significantly. A few examples of combined reconstruction, identification, and isolation efficiencies for typical working points used in ATLAS physics analyses but illustrated with a common $Z \to ee$ sample are shown in Sect. 9. The summary of the work is given in Sect. 10.

2 The ATLAS detector

The ATLAS detector [5] is designed to observe particles produced in the high-energy pp and heavy-ion LHC collisions. It is composed of an inner detector, used for charged-particle tracking, immersed in a 2 T axial magnetic field produced by a thin superconducting solenoid; electromagnetic (EM) and hadronic calorimeters outside the solenoid; and a muon spectrometer. A two-level triggering system reduces the total data-taking rate to approximately 1 kHz. The second level, the high-level trigger (HLT), employs selection algorithms using full-granularity detector information; likelihood-based electron identification and its HLT variant are described in Sect. 6.

The inner detector provides precise reconstruction of tracks within a pseudorapidity range[2] $|\eta| \lesssim 2.5$. The innermost part of the inner detector consists of a high-granularity silicon pixel detector and includes the insertable B-layer [6,7], a new tracking layer closest to the beamline designed to improve impact parameter resolution, which is important primarily for heavy-flavour identification. The silicon pixel detector provides typically four measurement points for charged particles originating in the beam-interaction region. A semiconductor tracker (SCT) consisting of modules with two layers of silicon microstrip sensors surrounds the pixel detector and provides typically eight hits per track at intermediate radii. The outermost region of the inner detector is covered by a transition radiation tracker (TRT) consisting of straw drift tubes filled with a xenon-based gas mixture, interleaved with polypropylene/polyethylene radiators. The TRT offers electron identification capability via the detection of transition-radiation photons generated by the radiators for highly relativistic particles. Some of the TRT modules instead contain an argon-based gas mixture, as mitigation for gas leaks that cannot be repaired without an invasive opening of the inner detector. The presence of this gas mixture is taken into account in the simulation. ATLAS has developed a TRT particle-identification algorithm that partially mitigates the loss in identification power caused by the use of this argon-based gas mixture. For charged particles with transverse momentum $p_{\mathrm{T}} > 0.5$ GeV within its pseudora-

[2] ATLAS uses a right-handed coordinate system with its origin at the nominal interaction point (IP) in the centre of the detector and the z-axis along the beam pipe. The x-axis points from the IP to the centre of the LHC ring, and the y-axis points upwards. Cylindrical coordinates (r, ϕ) are used in the transverse plane, ϕ being the azimuthal angle around the z-axis. The pseudorapidity is defined in terms of the polar angle θ as $\eta = -\ln\tan(\theta/2)$. Angular distance is measured in units of $\Delta R \equiv \sqrt{(\Delta\eta)^2 + (\Delta\phi)^2}$.

pidity coverage ($|\eta| \lesssim 2$), the TRT provides typically 35 hits per track.

The ATLAS calorimeter system has both electromagnetic and hadronic components and covers the pseudorapidity range $|\eta| < 4.9$, with finer granularity over the region matching the inner detector. The central EM calorimeters are of an accordion-geometry design made from lead/liquid-argon (LAr) detectors, providing a full ϕ coverage. These detectors are divided into two half-barrels ($-1.475 < \eta < 0$ and $0 < \eta < 1.475$) and two endcap components ($1.375 < |\eta| < 3.2$), with a transition region between the barrel and the endcap ($1.37 < |\eta| < 1.52$) which contains a relatively large amount of inactive material. Over the region devoted to precision measurements ($|\eta| < 2.47$, excluding the transition regions), the EM calorimeter is segmented into longitudinal (depth) compartments called the *first* (also known as *strips*), *second*, and *third* layers. The first layer consists of strips finely segmented in η, offering excellent discrimination between photons and $\pi^0 \to \gamma\gamma$ decays. At electron or photon energies relevant to this paper, most of the energy is collected in the second layer, which has a lateral granularity of 0.025×0.025 in (η, ϕ) space, while the third layer provides measurements of energy deposited in the tails of the shower. The central EM calorimeter is complemented by two presampler detectors in the region $|\eta| < 1.52$ (barrel) and $1.5 < |\eta| < 1.8$ (endcaps), made of a thin LAr layer, providing a sampling for particles that start showering in front of the EM calorimeters. Hadronic calorimetry is provided by the steel/scintillating-tile calorimeter, segmented into three barrel structures within $|\eta| < 1.7$, and two copper/LAr hadronic endcap calorimeters. They surround the EM calorimeters and provide additional discrimination through further energy measurements of possible EM shower tails as well as rejection of events with activity of hadronic origin.

3 Datasets and simulated-event samples

All data collected by the ATLAS detector undergo careful scrutiny to ensure the quality of the recorded information; data used for the efficiency measurements are filtered by requiring that all detector subsystems needed in the analysis (calorimeters and tracking detectors) are operating nominally. After all data-quality requirements (94% efficient), 37.1 fb^{-1} of pp collision data from the 2015–2016 dataset are available for analysis. Some results in this paper are based on the 2016 dataset only, and contain approximately 10% less data.

Samples of simulated $Z \to ee$ and $J/\psi \to ee$ decays as well as single-electron samples are used to benchmark the expected electron efficiencies and to define the electron-identification criteria. The $Z \to ee$ Monte Carlo (MC) samples were generated with the POWHEG-Box v2 MC program [8–12] interfaced to the PYTHIA v.8.186 [13] parton shower model. The CT10 parton distribution function (PDF) set [14] was used in the event generation with the matrix element, and the AZNLO [15] set of generator-parameter values (tune) with the CTEQ6L1 [16] PDF set were used for the modelling of non-perturbative effects. The $J/\psi \to ee$ samples were generated with PYTHIA v.8.186; the A14 set of tuned parameters [17] was used together with the CTEQ6L1 PDF set for event generation and the parton shower. The simulated single-electron samples were produced with a flat distribution in η as well as in p_{T} in the region 3.5 GeV to 100 GeV, followed by a linear ramp down to 300 GeV, and then a flat distribution again to 3 TeV. For studies of electrons in simulated event samples, the reconstructed-electron track is required to have hits in the inner detector which originate from the true electron during simulation.

Backgrounds that may mimic the signature of prompt electrons were simulated with two-to-two processes in the PYTHIA v.8.186 event generator using the A14 set of tuned parameters and the NNPDF2.3LO PDF set [18]. These processes include multijet production, $qg \to q\gamma$, $q\bar{q} \to g\gamma$, W- and Z-boson production (as well as other electroweak processes), and top-quark production. A filter was applied to the simulation to enrich the final sample in electron backgrounds. This filter retains events in which particles produced in the hard scatter (excluding muons and neutrinos) have a summed energy that exceeds 17 GeV in an area of $\Delta\eta \times \Delta\phi = 0.1 \times 0.1$, which mimics the highly localised energy deposits that are characteristic of electrons. When using this background sample, prompt electrons from W- and Z-boson decays are excluded using generator-level simulation information.

Multiple overlaid pp collisions were simulated with the soft QCD processes of PYTHIA v.8.186 using the MSTW2008LO PDF [19]. The Monte Carlo events were reweighted so that the $\langle\mu\rangle$ distribution matches the one observed in the data. All samples were processed with the GEANT4-based simulation [20,21] of the ATLAS detector.

4 Electron-efficiency measurements

Electrons isolated from other particles are important ingredients in Standard Model measurements and in searches for physics beyond the Standard Model. However, the experimentally determined electron spectra must be corrected for the selection efficiencies, such as those related to the trigger, as well as particle isolation, identification, and reconstruction, before absolute measurements can be made. These efficiencies may be estimated directly from data using tag-and-probe methods. These methods select, from known resonances such as $Z \to ee$ or $J/\psi \to ee$, unbiased samples of electrons (*probes*) by using strict selection requirements on

the second object (*tags*) produced from the particle's decay. The events are selected on the basis of the electron–positron invariant mass. The efficiency of a given requirement can then be determined by applying it to the probe sample after accounting for residual background contamination.

The total efficiency ϵ_{total} may be factorised as a product of different efficiency terms:

$$\begin{aligned}\epsilon_{\text{total}} &= \epsilon_{\text{EMclus}} \times \epsilon_{\text{reco}} \times \epsilon_{\text{id}} \times \epsilon_{\text{iso}} \times \epsilon_{\text{trig}} \\ &= \left(\frac{N_{\text{cluster}}}{N_{\text{all}}}\right) \times \left(\frac{N_{\text{reco}}}{N_{\text{cluster}}}\right) \\ &\quad \times \left(\frac{N_{\text{id}}}{N_{\text{reco}}}\right) \times \left(\frac{N_{\text{iso}}}{N_{\text{id}}}\right) \times \left(\frac{N_{\text{trig}}}{N_{\text{iso}}}\right). \end{aligned} \tag{1}$$

The efficiency to reconstruct in the electromagnetic calorimeter EM-cluster candidates (localised energy deposits) associated with all produced electrons, ϵ_{EMclus}, is given by the number of reconstructed EM calorimeter clusters N_{cluster} divided by the number of produced electrons N_{all}. This efficiency is evaluated entirely from simulation, where the reconstructed cluster is associated to a genuine electron produced at generator level. The reconstruction efficiency, ϵ_{reco}, is given by the number of reconstructed electron candidates N_{reco} divided by the number of EM-cluster candidates N_{cluster}. This reconstruction efficiency, as well as the efficiency to reconstruct electromagnetic clusters, is described in Sect. 5. The identification efficiency, ϵ_{id}, is given by the number of identified and reconstructed electron candidates N_{id} divided by N_{reco}, and is described in Sect. 6. The isolation efficiency is calculated as the number of identified electron candidates satisfying the isolation, identification, and reconstruction requirements N_{iso} divided by N_{id}, and is explained in Sect. 7. Finally, the trigger efficiency is calculated as the number of triggered (and isolated, identified, reconstructed) electron candidates N_{trig} divided by N_{iso} (see for example Ref. [22]; trigger efficiency is not discussed further in this paper).

Isolated electrons selected for physics analyses are subject to large backgrounds from misidentified hadrons, electrons from photon conversions, and non-isolated electrons originating from heavy-flavour decays. The biggest challenge in the efficiency measurements presented in this paper is the estimation of probes that originate from background rather than signal processes. This background is largest for the sample of cluster probes, but the fraction of such events is reduced with each efficiency step, from left to right, as given in Eq. (1).

The accuracy with which the detector simulation models the observed electron efficiency plays an important role when using simulation to predict physics processes, for example the signal or background of a measurement. In order to achieve reliable results, the simulated events need to be corrected to reproduce as closely as possible the efficiencies measured in data. This is achieved by applying a multiplicative correction factor to the event weight in simulation. This correction factor is defined as the ratio of the efficiency measured in data to that determined from Monte Carlo events. These correction weights are normally close to unity; deviations from unity usually arise from mismodelling in the simulation of tracking properties or shower shapes in the calorimeters.

Systematic uncertainties in the correction factors are evaluated by varying the requirements on the selection of both the tag and the probe electron candidates as well as varying the details of the background-subtraction method. The central value of the measurement is extracted by averaging the measurement results over all variations. The statistical uncertainty in a single variation of the measurement is calculated following the approach in Ref. [23], i.e. assuming a binomial distribution. If the evaluation of the number of events (before or after the selection under investigation) is the result of a background subtraction, the corresponding statistical uncertainties are also included in the overall statistical uncertainty, rather than in the systematic uncertainty. The systematic uncertainty in the averaged result is obtained from the root-mean-square (RMS) of the individual results, and in the case of non-Gaussian behaviour, it is inflated to cover 68% of the variations.

The tag-and-probe measurements are based on samples of $Z \to ee$ and $J/\psi \to ee$ events. Whereas the $Z \to ee$ sample is used to extract all terms in Eq. (1), the $J/\psi \to ee$ sample is only used to extract the identification efficiency ϵ_{id} since the significant background as well as the difficulties in designing a trigger for this process prevent its use in determining the reconstruction efficiency. The combination of the two samples allows identification efficiency measurements over a significant transverse energy E_{T} range of 4.5 GeV to 20 GeV for the $J/\psi \to ee$ sample, and above 15 GeV (4.5 GeV for the isolation efficiency measurement) for the $Z \to ee$ sample, while still providing overlapping measurements between the samples in the E_{T} range 15–20 GeV where the correction factors of the two results are combined using a χ^2 minimisation [2,24]. Combining the correction factors instead of the individual measured and simulated efficiencies reduces the dependence on kinematic differences of the physics processes as they cancel out in the ratio.

Due to the number of events available in the sample, the $Z \to ee$ tag-and-probe measurements provide limited information about electron efficiencies beyond approximately electron $E_{\text{T}} = 150$ GeV. The following procedure is used to assign correction factors for candidate electrons with high E_{T}:

- *reconstruction:* the same η-dependent correction factors are used for all $E_{\text{T}} > 80$ GeV,
- *identification:* correction factors determined up to $E_{\text{T}} = 250$ GeV are applicable beyond,

- *isolation:* correction factors of unity are used for $E_{\mathrm{T}} > 150$ GeV.

The following subsections give a brief overview of the methods used to extract efficiencies in the data. Efficiency extraction using simulated events is performed in a very similar fashion, except that no background subtraction is performed. More detailed descriptions may be found in Ref. [3].

4.1 Measurements using $Z \to ee$ events

$Z \to ee$ events with two electron candidates in the central region of the detector, $|\eta| < 2.47$, were collected using two triggers designed to identify at least one electron in the event. One trigger has a minimum E_{T} threshold of 24 GeV (which was changed to 26 GeV during 2016 data-taking), and requires Tight trigger identification (see Sect. 6) and track isolation (see Sect. 7), while the other trigger has a minimum E_{T} threshold of 60 GeV and Medium trigger identification. The tag electron is required to have $E_{\mathrm{T}} > 27$ GeV and to lie outside of the calorimeter transition region, $1.37 < |\eta| < 1.52$. It must be associated with the object that fired the trigger, and must also pass Tight-identification (see Sect. 6) and isolation requirements. If both electrons pass the tag requirements, the event will provide two probes. The invariant-mass distribution constructed from the tag electron and the cluster probe is used to discriminate prompt electrons from background. The signal efficiency is extracted in a window of ± 15 GeV around the Z-boson mass peak at 91.2 GeV. Approximately 35 million electron-candidate probes from $Z \to ee$ data events are available for analysis.

The probe electrons in the denominator of the reconstruction-efficiency measurement (see Eq. (1)) are electromagnetic clusters both with and without associated tracks, while those in the numerator consist of clusters with matched tracks, i.e. reconstructed electrons (see Sect. 5). These tracks are required to have at least seven hits in the silicon detectors (i.e. both pixel and SCT) and at least one hit in the pixel detector. The background for electron candidates without a matched track is estimated by fitting a polynomial to the sideband regions of the invariant-mass distribution of the candidate electron pairs, after subtracting the remaining signal contamination using simulation. The background for electron candidates with a matched track is estimated by constructing a background template by inverting identification or isolation criteria for the probe electron candidate and normalising it to the invariant-mass sideband regions, after subtraction of the signal events in both the template and the sidebands.

The probe electrons used in the denominator of the identification efficiency measurement are the same as those used in the numerator of the reconstruction efficiency measurement, with an additional opposite-charge requirement on the tag–probe pair; this method assumes that the charge of the candidate is correctly identified. The numerator of the identification measurement consists of probes satisfying the identification criteria under evaluation. Two methods are used in the identification measurements to estimate the non-prompt background [2,3]; they are treated as variations of the same measurement: the *Zmass* method uses the invariant mass of the tag–probe pair while the *Ziso* method uses the isolation distribution of probes in the signal mass window around the Z-boson peak. In both cases, and as discussed for the reconstruction-efficiency measurement, background templates are formed and normalised to the sideband regions, after subtraction of the signal events. The contamination from charge-misidentified candidates is negligible in this sample. In the *Zmass* method, the numerator of the identification efficiency uses same-charge events to obtain a normalisation factor for the template in opposite-charge events, in order to reduce the contamination from signal events.

The isolation-efficiency measurements are performed using the *Zmass* method, as described above. The denominator in the efficiency ratio is the number of identified electron candidates, while the numerator consists of candidates that also satisfy the isolation criteria under evaluation.

In all cases, systematic uncertainties in the data-MC correction factors are evaluated from the background-subtraction method as well as variations of the quality of the probed electrons via changes in the window around the Z-boson mass peak. They are also evaluated by varying the identification and isolation requirements on the tag, the sideband regions used in the fits, and the template definitions.

4.2 Measurements using $J/\psi \to ee$ events

$J/\psi \to ee$ events with at least two electron candidates with $E_{\mathrm{T}} > 4.5$ GeV and $|\eta| < 2.47$ were collected with dedicated dielectron triggers with electron E_{T} thresholds ranging from 4 to 14 GeV. Each of these triggers requires Tight trigger identification and E_{T} above a certain threshold for one trigger object, while only demanding the electromagnetic cluster E_{T} to be higher than some other (lower) threshold for the second object. The $J/\psi \to ee$ selection consists of one electron candidate passing a Tight-identification selection (see Sect. 6) and one reconstructed-electron candidate (see Sect. 5). The tag electron is required to be outside the calorimeter transition region $1.37 < |\eta| < 1.52$ and to be associated with the Tight trigger object. The probe electron must be matched to the second trigger object. Due to the nature of the sample (a mixture of prompt and non-prompt decays) as well as significant background, isolation requirements are applied on both the tag and the probe electrons, although for the latter the requirement is very loose so as to not bias the identification-efficiency measurement. Fur-

thermore, the tag and the probe electron candidates must be separated from each other in η–ϕ space by $\Delta R > 0.15$. If both electrons pass the tag requirements, the event will provide two probes. Approximately 80 thousand electron-candidate probes from $J/\psi \to ee$ data events are available for analysis.

The invariant-mass distribution of the two electron candidates in the range 1.8–4.6 GeV is fit with functions to extract three contributions: J/ψ events, $\psi(2S)$ events, and the background from hadronic jets, heavy flavour, and electrons from conversions. The J/ψ and $\psi(2S)$ contributions are each modelled with a Crystal Ball function convolved with a Gaussian function, and the background is estimated using same-charge events and fit with a second-order Chebyshev polynomial.

$J/\psi \to ee$ events come from a mixture of prompt and non-prompt J/ψ production, with relative fractions depending both on the triggers used to collect the data and on the E_{T} of the probe electrons. Prompt J/ψ mesons are produced directly in pp collisions and in radiative decays of directly produced heavier charmonium states. Non-prompt J/ψ production occurs when the J/ψ is produced in the decay of a b-hadron. Only the prompt production yields isolated electrons, which are expected to have efficiencies similar to those of electrons from physics processes of interest such as $H \to ZZ^* \to 4\ell$. Given the difficulties associated with the fact that electrons from non-prompt decays are often surrounded by hadronic activity, two methods have been developed to measure the efficiency for isolated electrons at low E_{T}, both exploiting the pseudo-proper time variable[3] t_0. In the *cut* method, a requirement is imposed on the pseudo-proper time, so that the prompt component is enhanced, thereby limiting the non-prompt contribution. The residual non-prompt fraction is estimated using simulated samples and ATLAS measurements of $J/\psi \to \mu\mu$ [26]. In the *fit* method, a fit to the pseudo-proper time distribution is used to extract the prompt fraction, after subtracting the background using the pseudo-proper time distribution in sideband regions around the J/ψ peak.

The systematic uncertainties in the data-to-simulation correction factors of both methods are estimated by varying the isolation criteria for the tag and the probe electron candidates, the fit models for the signal and background, the signal invariant-mass range, the pseudo-proper time requirement in the *cut* method, and the fit range in the *fit* method.

[3] The pseudo-proper time is defined as $t_0 = L_{xy} \cdot m_{\mathrm{PDG}}^{J/\psi} / p_{\mathrm{T}}^{J/\psi}$, where L_{xy} is the displacement of the J/ψ vertex from the primary vertex projected onto the flight direction of the J/ψ in the transverse plane, $m_{\mathrm{PDG}}^{J/\psi}$ is the nominal J/ψ mass [25] and $p_{\mathrm{T}}^{J/\psi}$ is the J/ψ-reconstructed transverse momentum.

5 Electron reconstruction

An electron can lose a significant amount of its energy due to bremsstrahlung when interacting with the material it traverses. The radiated photon may convert into an electron–positron pair which itself can interact with the detector material. These positrons, electrons, and photons are usually emitted in a very collimated fashion and are normally reconstructed as part of the same electromagnetic cluster. These interactions can occur inside the inner-detector volume or even in the beam pipe, generating multiple tracks in the inner detector, or can instead occur downstream of the inner detector, only impacting the shower in the calorimeter. As a result, it is possible to produce and match multiple tracks to the same electromagnetic cluster, all originating from the same primary electron.

The reconstruction of electron candidates within the kinematic region encompassed by the high-granularity electromagnetic calorimeter and the inner detector is based on three fundamental components characterising the signature of electrons: localised clusters of energy deposits found within the electromagnetic calorimeter, charged-particle tracks identified in the inner detector, and close matching in $\eta \times \phi$ space of the tracks to the clusters to form the final electron candidates. Therefore, electron reconstruction in the precision region of the ATLAS detector ($|\eta| < 2.47$) proceeds along those steps, described below in this order. Figure 1 provides a schematic illustration of the elements that enter into the reconstruction and identification (see Sect. 6) of an electron.

5.1 Seed-cluster reconstruction

The $\eta \times \phi$ space of the EM calorimeter is divided into a grid of 200×256 elements (towers) of size $\Delta\eta \times \Delta\phi = 0.025 \times 0.025$, corresponding to the granularity of the second layer of the EM calorimeter. For each element, the energy (approximately calibrated at the EM scale), collected in the first, second, and third calorimeter layers as well as in the presampler (only for $|\eta| < 1.8$, the region where the presampler is located) is summed to form the energy of the tower. Electromagnetic-energy cluster candidates are then seeded from localised energy deposits using a sliding-window algorithm [27] of size 3×5 towers in $\eta \times \phi$, whose summed transverse energy exceeds 2.5 GeV. The centre of the 3×5 seed cluster moves in steps of 0.025 in either the η or ϕ direction, searching for localised energy deposits; the seed-cluster reconstruction process is repeated until this has been performed for every element in the calorimeter. If two seed-cluster candidates are found in close proximity (if their towers overlap within an area of $\Delta\eta \times \Delta\phi = 5 \times 9$ units of 0.025×0.025), the candidate with the higher transverse energy is retained, if its E_{T} is at least 10% higher than the

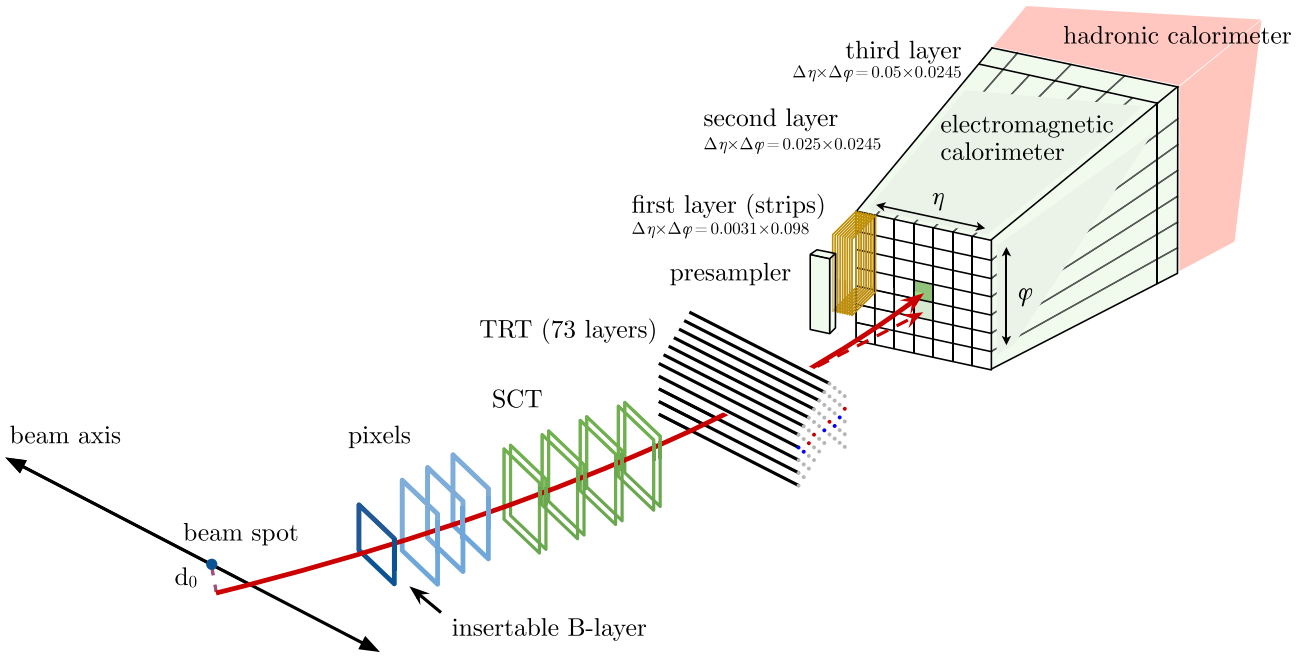

Fig. 1 A schematic illustration of the path of an electron through the detector. The red trajectory shows the hypothetical path of an electron, which first traverses the tracking system (pixel detectors, then silicon-strip detectors and lastly the TRT) and then enters the electromagnetic calorimeter. The dashed red trajectory indicates the path of a photon produced by the interaction of the electron with the material in the tracking system

other candidate. If their E_{T} values are within 10% of each other, the candidate containing the highest-E_{T} central tower is kept. The duplicate cluster is thereby removed. The reconstruction efficiency of this seed-cluster algorithm (effectively $\epsilon_{\mathrm{EMclus}}$ in Eq. (1)) depends on $|\eta|$ and E_{T}. As a function of E_{T}, it ranges from 65% at $E_{\mathrm{T}} = 4.5$ GeV, to 96% at $E_{\mathrm{T}} = 7$ GeV, to more than 99% above $E_{\mathrm{T}} = 15$ GeV, as can be seen in Fig. 2. This efficiency is determined entirely from simulation. Efficiency losses due to seed-cluster reconstruction for $E_{\mathrm{T}} > 15$ GeV are negligible compared with the uncertainties attributed to the next two steps of the reconstruction (track reconstruction and track–cluster matching).

5.2 Track reconstruction

The basic building block for track reconstruction is a 'hit' in one of the inner-detector tracking layers. Charged-particle reconstruction in the pixel and SCT detectors begins by assembling clusters from these hits [28]. From these clusters, three-dimensional measurements referred to as space-points are created. In the pixel detector, each cluster equates to one space-point, while in the SCT, clusters from both stereo views of a strip layer must be combined to obtain a three-dimensional measurement. Track seeds are formed from sets of three space-points in the silicon-detector layers. The track reconstruction then proceeds in three steps: pattern recognition, ambiguity resolution, and TRT extension (for more details of the TRT extension, see Ref. [29]). The pattern-recognition algorithm uses the pion hypothesis for the model of energy loss from interactions of the particle with the detector material. However, if a track seed with $p_{\mathrm{T}} > 1$ GeV cannot be successfully extended to a full track of at least seven silicon hits per candidate track and the EM cluster satisfies requirements on the shower width and depth, a second attempt with modified pattern recognition, one which allows up to 30% energy loss for bremsstrahlung at each intersection of the track with the detector material, is made. Track candidates with $p_{\mathrm{T}} > 400$ MeV are fit, according to the hypothesis used in the pattern recognition, using the ATLAS Global χ^2 Track Fitter [30]. Any ambiguity resulting from track candidates sharing hits is resolved at the same stage. In order to avoid inefficiencies for electron tracks with significant bremsstrahlung, if the fit fails under the pion hypothesis and its polar and azimuthal separation to the EM cluster is below a value, a second fit is attempted under an electron hypothesis (an extra degree of freedom, in the form of an additional Gaussian term, is added to the χ^2 to compensate for the additional bremsstrahlung losses coming from electrons; such an energy-loss term is neglected in the pion-hypothesis fit). Figure 2 (top) shows that the reconstruction efficiency of the track-fitting step ranges from 80% at $E_{\mathrm{T}} = 1$ GeV to more than 98% above $E_{\mathrm{T}} = 10$ GeV.

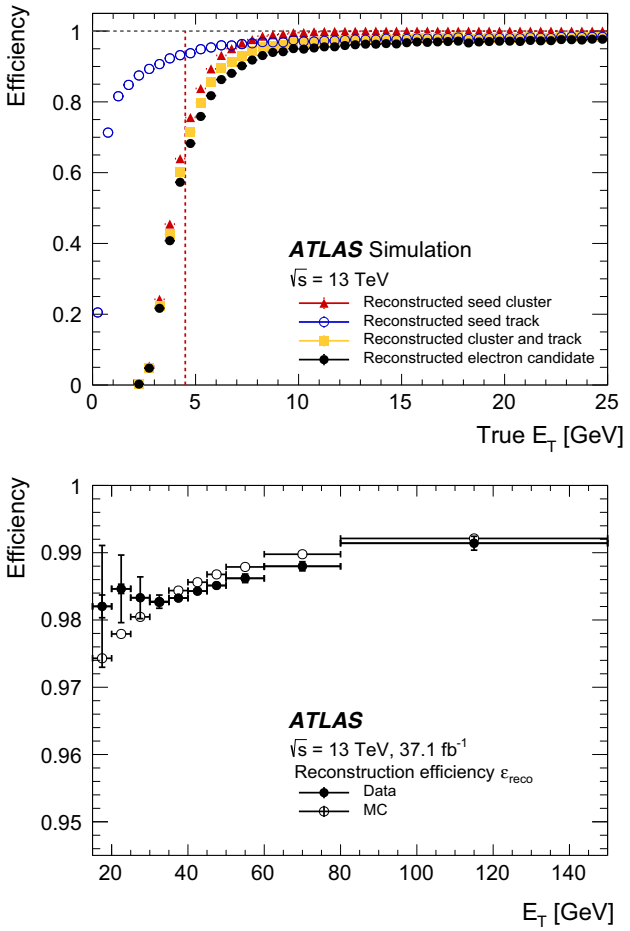

Fig. 2 Top: the total reconstruction efficiency for simulated electrons in a single-electron sample is shown as a function of the true (generator) transverse energy E_{T} for each step of the electron-candidate formation: $\Delta\eta \times \Delta\phi = 3 \times 5$ (in units of 0.025×0.025) seed-cluster reconstruction (red triangles), seed-track reconstruction using the Global χ^2 Track Fitter (blue open circles), both of these steps together but instead using GSF tracking (yellow squares), and the final reconstructed electron candidate, which includes the track-to-cluster matching (black closed circles). As the cluster reconstruction requires uncalibrated cluster seeds with $E_{\mathrm{T}} > 2.5$ GeV, the total reconstruction efficiency is less than 60% below 4.5 GeV (dashed line). Bottom: the reconstruction efficiency relative to reconstructed clusters, ϵ_{reco}, as a function of electron transverse energy E_{T} for $Z \to ee$ events, comparing data (closed circles) with simulation (open circles). The inner uncertainties are statistical while the total uncertainties include both the statistical and systematic components

A subsequent fitting procedure, using an optimised Gaussian-sum filter (GSF) [31] designed to better account for energy loss of charged particles in material, is applied to the clusters of raw measurements. This procedure is used for tracks which have at least four silicon hits and that are loosely matched to EM clusters. The separation of the cluster-barycentre position and the position of the track extrapolated from the perigee to the second layer of the calorimeter must satisfy $|\eta_{\mathrm{cluster}} - \eta_{\mathrm{track}}| < 0.05$ and one of two alternative requirements on the azimuthal separation between the cluster position and the track: $-0.20 < \Delta\phi < 0.05$ or $-0.10 < \Delta\phi_{\mathrm{res}} < 0.05$, where q is the sign of the electric charge of the particle, and $\Delta\phi$ and $\Delta\phi_{\mathrm{res}}$ are calculated as $-q \times (\phi_{\mathrm{cluster}} - \phi_{\mathrm{track}})$ with the momentum of the track rescaled to the energy of the cluster for $\Delta\phi_{\mathrm{res}}$. The asymmetric condition for the matching in ϕ mitigates the effects of energy loss due to bremsstrahlung where tracks with negative (positive) electric charge bend due to the magnetic field in the positive (negative) ϕ direction.

The GSF method [32] is based on a generalisation of the Kalman filter [33] and takes into account the non-linear effects related to bremsstrahlung. Within the GSF, experimental noise is modelled by a sum of Gaussian functions. The GSF therefore consists of a number of Kalman filters running in parallel, the result of which is that each track parameter is approximated by a weighted sum of Gaussian functions. Six Gaussian functions are used to describe the material-induced energy losses and up to twelve to describe the track parameters. In the final step, the mode of the energy distribution is used to represent the energy loss.

Radiative losses of energy lead to a decrease in momentum, resulting in increased curvature of the electron's trajectory in the magnetic field. When accounting for such losses via the GSF method, all track parameters relevant to the bending-plane are expected to improve. Such a parameter is the transverse impact parameter significance: d_0 divided by its estimated uncertainty $\sigma(d_0)$. Since the curvature, in the ATLAS coordinate frame, is positive for negative particles and negative for positive particles, the signed impact parameter significance (i.e. multiplied by the sign of the reconstructed electric charge q of the electron) is used. Figure 3 shows $q \times d_0/\sigma(d_0)$ for the track associated with the electron, i.e. the primary electron track. A clear improvement in $q \times d_0/\sigma(d_0)$ for genuine electron tracks fitted with the GSF over tracks with the ATLAS Global χ^2 Track Fitter is observed; the distribution is narrower and better centred at zero. Figure 3 also shows, for the ratio of the electron-candidate charge to its momentum q/p, the relative difference between the true generator value and the reconstructed value; the GSF method shows a sharper and better-centred distribution near zero with smaller tails. The reconstruction efficiency for finding both a seed cluster and a GSF track is shown in Fig. 2 (top).

5.3 Electron-candidate reconstruction

The matching of the GSF-track candidate to the candidate calorimeter seed cluster and the determination of the final cluster size complete the electron-reconstruction procedure. This matching procedure is similar to the loose matching discussed above prior to the GSF step, but with stricter requirements; the track-matching in ϕ is tightened

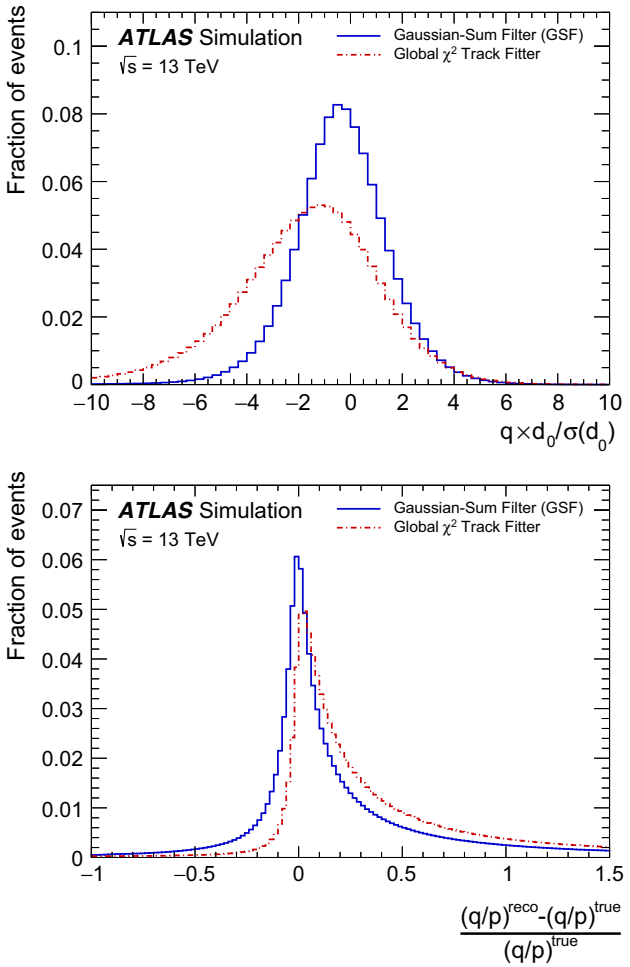

Fig. 3 Distributions of the reconstructed electric charge of the candidate electron multiplied by the transverse impact parameter significance, $q \times d_0/\sigma(d_0)$ (top) and the relative difference between the reconstructed value of the candidate-electron charge divided by its momentum, q/p, and the true generator value (bottom). The distributions are shown for tracks fitted with the Global χ^2 Track Fitter (dashed red lines) and for tracks fitted with the GSF (solid blue line). The distributions were obtained from a simulated single-electron sample

to $-0.10 < \Delta\phi < 0.05$, keeping the original alternative requirement $-0.10 < \Delta\phi_{\text{res}} < 0.05$ the same. If several tracks fulfil the matching criteria, the track considered to be the primary electron track is selected using an algorithm that takes into account the distance in η and ϕ between the extrapolated tracks and the cluster barycentres measured in the second layer of the calorimeter, the number of hits in the silicon detectors, and the number of hits in the innermost silicon layer; a candidate with an associated track with at least four hits in the silicon layers and no association with a vertex from a photon conversion [34] is considered as an electron candidate. However, if the primary candidate track can be matched to a secondary vertex and has no pixel hits, then this object is classified as a photon candidate (likely a conversion). A further classification is performed using the candidate electron's E/p and p_{T}, the presence of a pixel hit, and the secondary-vertex information, to determine unambiguously whether the object is only to be considered as an electron candidate or if it should be ambiguously classified as potentially either a photon candidate or an electron candidate. However, this classification scheme is mainly for the benefit of keeping a high photon-reconstruction efficiency. Since all electron identification operating points described in Sect. 6 require a track with a hit in the innermost silicon layer (or in the next-to-innermost layer if the innermost layer is non-operational), most candidates fall into the 'unambiguous' category after applying an identification criterion.

Finally, reconstructed clusters are formed around the seed clusters using an extended window of size 3×7 in the barrel region ($|\eta| < 1.37$) or 5×5 in the endcap ($1.52 < |\eta| < 2.47$) by simply expanding the cluster size in ϕ or η, respectively, on either side of the original seed cluster. A method using both elements of the extended-window size is used in the transition region of $1.37 < |\eta| < 1.52$. The energy of the clusters must ultimately be calibrated to correspond to the original electron energy. This detailed calibration is performed using multivariate techniques [35,36] based on data and simulated samples, and only after the step of selecting electron candidates rather than during the reconstruction step, which relies on approximate EM-scale energy clusters. The energy of the final electron candidate is computed from the calibrated energy of the extended-window cluster while the ϕ and η directions are taken from the corresponding track parameters, measured relative to the beam spot, of the track best matched to the original seed cluster.

Above $E_{\text{T}} = 15$ GeV, the efficiency to reconstruct an electron having a track of good quality (at least one pixel hit and at least seven silicon hits) varies from approximately 97–99%. The simulation has lower efficiency than data in the low E_{T} region ($E_{\text{T}} < 30$ GeV) while the opposite is true for the higher E_{T} region ($E_{\text{T}} > 30$ GeV), as demonstrated in Figs. 2 and 4, which show the reconstruction efficiency as a function of E_{T} and as a function of η in bins of E_{T}, respectively, from $Z \to ee$ events. All measurements are binned in two dimensions. The uncertainty in the efficiency in data is typically 1% in the $E_{\text{T}} = 15{-}20$ GeV bin and reaches the per-mille level at higher E_{T} and the uncertainty in simulation is almost an order of magnitude smaller than for data. The systematic uncertainty dominates at low E_{T} for data, with the estimation of background from clusters with no associated track giving the largest contribution. Below $E_{\text{T}} = 15$ GeV, the reconstruction efficiency is determined solely from the simulation; a 2% (5%) uncertainty is assigned in the barrel (endcap) region.

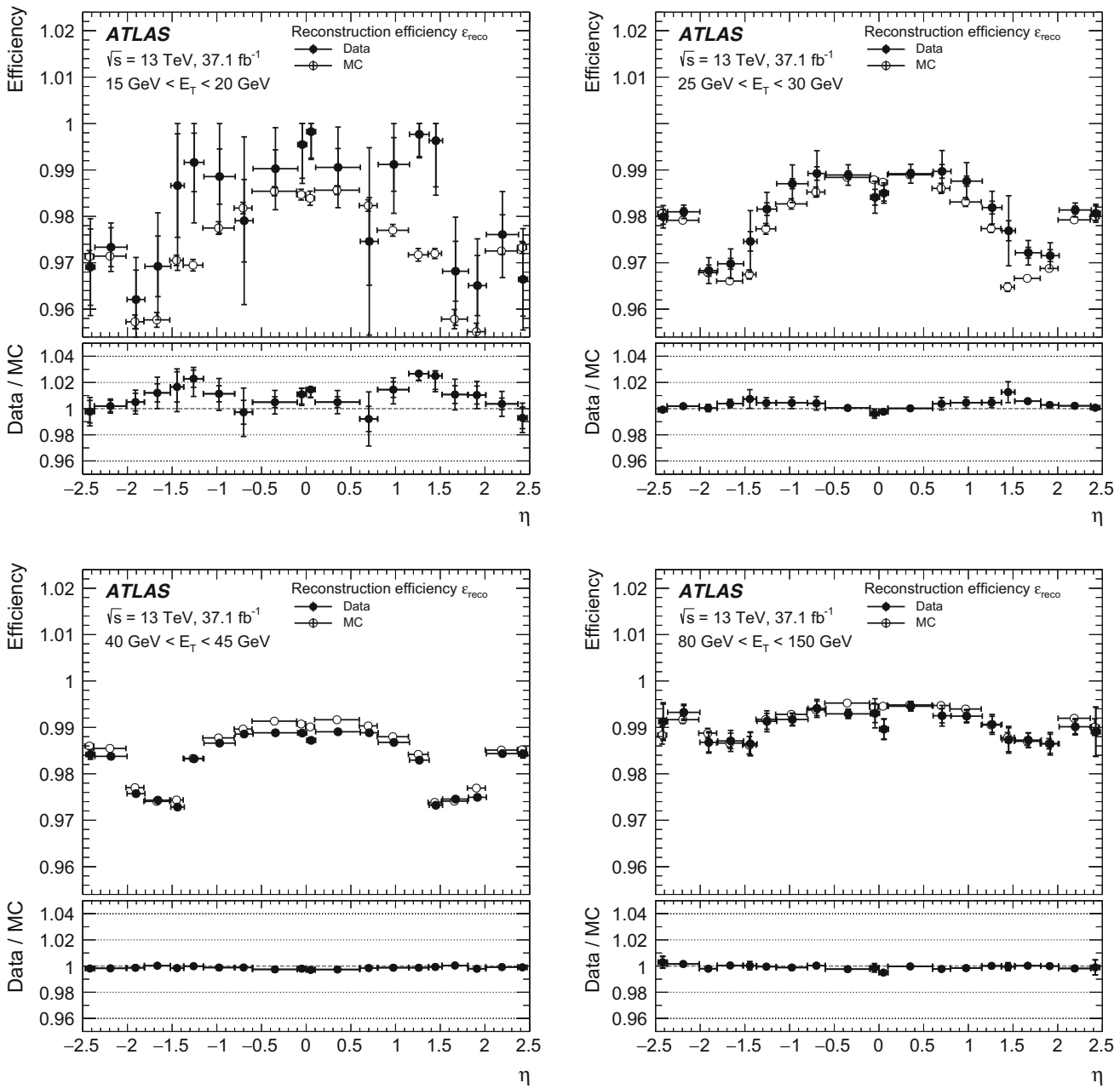

Fig. 4 Reconstruction efficiencies relative to reconstructed clusters, ϵ_{reco}, evaluated in the 2015–2016 dataset (closed points) and in simulation (open points), and their ratio, using the $Z \to ee$ process, as a function of η in four illustrative E_{T} bins: 15–20 GeV (top left), 25–30 GeV (top right), 40–45 GeV (bottom left), and 80–150 GeV (bottom right). The inner uncertainties are statistical while the total uncertainties include both the statistical and systematic components

6 Electron identification

Prompt electrons entering the central region of the detector ($|\eta| < 2.47$) are selected using a likelihood-based (LH) identification. The inputs to the LH include measurements from the tracking system, the calorimeter system, and quantities that combine both tracking and calorimeter information. The various inputs are described in Table 1 and the components of the quantities described in this table are illustrated schematically in Fig. 1. The LH identification is very similar in method to the electron LH identification used in Run 1 (2010–2012) [3], but there are some important differences. To prepare for the start of data-taking with a higher center-of-mass energy and different detector conditions it was necessary to construct probability density functions (pdfs) based on simulated events rather than data events, and correct the

resulting distributions for any mismodelling. Furthermore, the efficiency was smoothed as a function of E_{T} and the likelihood was adjusted to allow its use for electrons with $E_{\mathrm{T}} > 300$ GeV.

6.1 The likelihood identification

The electron LH is based on the products for signal, L_S, and for background, L_B, of n pdfs, P:

$$L_{S(B)}(\mathbf{x}) = \prod_{i=1}^{n} P_{S(B),i}(x_i), \tag{2}$$

where $\mathbf{x}$ is the vector of the various quantities specified in Table 1. $P_{S,i}(x_i)$ is the value of the signal pdf for quantity i at value x_i and $P_{B,i}(x_i)$ is the corresponding value of the background pdf. The signal is prompt electrons, while the background is the combination of jets that mimic the signature of prompt electrons, electrons from photon conversions in the detector material, and non-prompt electrons from the decay of hadrons containing heavy flavours. Correlations in the quantities selected for the LH are neglected.

For each electron candidate, a discriminant d_L is formed:

$$d_L = \frac{L_S}{L_S + L_B}; \tag{3}$$

the electron LH identification is based on this discriminant. The discriminant d_L has a sharp peak at unity (zero) for signal (background); this sharp peak makes it inconvenient to select operating points as it would require extremely fine binning. An inverse sigmoid function is used to transform the distribution of the discriminant of Eq. (3):

$$d_L' = -\tau^{-1} \ln(d_L^{-1} - 1),$$

where the parameter τ is fixed to 15 [37]. As a consequence, the range of values of the transformed discriminant no longer varies between zero and unity. For each operating point, a value of the transformed discriminant is chosen: electron candidates with values of d_L' larger than this value are considered signal. An example of the distribution of a transformed discriminant is shown in Fig. 5 for prompt electrons from Z-boson decays and for background. This distribution illustrates the effective separation between signal and background encapsulated in this single quantity.

There are two advantages to using a LH-based electron identification over a selection-criteria-based (so-called "cut-based") identification. First, a prompt electron may fail the cut-based identification because it does not satisfy the selection criterion for a single quantity. In the LH-based selection, this electron can still satisfy the identification criteria, because the LH combines the information of all of the discriminating quantities. Second, discriminating quantities that have distributions too similar to be used in a cut-based identification without suffering large losses in efficiency may be added to the LH-based identification without penalty. Two examples of quantities that are used in the LH-based identification, but not in cut-based identifications, are R_ϕ and f_1, which are defined in Table 1. Figure 6 compares the distributions of these two quantities for prompt electrons and background.

6.2 The pdfs for the LH-identification

The pdfs for the electron LH are derived from the simulation samples described in Sect. 3. As described below, distinct pdfs are determined for each identification quantity in separate bins of electron-candidate E_{T} and η. The pdfs are created from finely binned histograms of the individual identification quantities. To avoid non-physical fluctuations in the pdfs arising from the limited size of the simulation samples, the histograms are smoothed using an adaptive kernel density estimation (KDE) implemented in the TMVA toolkit [37].

Imperfect detector modelling causes differences between the simulation quantities used to form the LH-identification and the corresponding quantities in data. Some simulation quantities are corrected to account for these differences so that the simulation models the data more accurately and hence the determination of the LH-identification operating points is made using a simulation that reproduces the data as closely as possible. These corrections are determined using simulation and data obtained with the $Z \to ee$ tag-and-probe method.

The differences between the data and the simulation typically appear as either a constant offset between the quantities (i.e., a shift of the distributions) or a difference in the width, quantified here as the full-width at half-maximum (FWHM) of the distribution of the quantity. In some cases, both shift and width corrections are applied. The quantities f_1, f_3, R_η, $w_{\eta 2}$ and R_ϕ have η-dependent offsets, and the quantities f_1, f_3, R_{had}, $\Delta\eta_1$ and $\Delta\phi_{\mathrm{res}}$ have differences in FWHM.

In the case that the difference is a shift, the value in the simulation is shifted by a fixed (η-dependent) amount to make the distribution in the simulation agree better with the distribution in the data. In the case of a difference in FWHM, the value in the simulation is scaled by a multiplicative factor. The optimal values of the shifts and width-scaling factors are determined by minimising a χ^2 that compares the distributions in the data and the simulation. An example of applying an offset is shown in the top panel of Fig. 7, while an example of applying a width-scaling factor is shown in the bottom panel of Fig. 7.

The pdfs for the E_{T} range of 4.5 GeV to 15 GeV are determined using $J/\psi \to ee$ Monte Carlo simulation and the

Table 1 Type and description of the quantities used in the electron identification. The columns labelled "Rejects" indicate whether a quantity has significant discrimination power between prompt electrons and light-flavour (LF) jets, photon conversions (γ), or non-prompt electrons from the semileptonic decay of hadrons containing heavy-flavour (HF) quarks (b- or c-quarks). In the column labelled "Usage," an "LH" indicates that the pdf of this quantity is used in forming L_S and L_B (defined in Eq. (2)) and a "C" indicates that this quantity is used directly as a selection criterion. In the description of the quantities formed using the second layer of the calorimeter, 3×3, 3×5, 3×7, and 7×7 refer to areas of $\Delta\eta \times \Delta\phi$ space in units of 0.025×0.025

Type	Description	Name	Rejects			Usage
			LF	γ	HF	
Hadronic leakage	Ratio of E_{T} in the first layer of the hadronic calorimeter to E_{T} of the EM cluster (used over the range $\lvert\eta\rvert < 0.8$ or $\lvert\eta\rvert > 1.37$)	R_{had1}	x	x		LH
	Ratio of E_{T} in the hadronic calorimeter to E_{T} of the EM cluster (used over the range $0.8 < \lvert\eta\rvert < 1.37$)	R_{had}	x	x		LH
Third layer of EM calorimeter	Ratio of the energy in the third layer to the total energy in the EM calorimeter. This variable is only used for $E_{\mathrm{T}} < 80$ GeV, due to inefficiencies at high E_{T}, and is also removed from the LH for $\lvert\eta\rvert > 2.37$, where it is poorly modelled by the simulation.	f_3	x			LH
Second layer of EM calorimeter	Lateral shower width, $\sqrt{(\Sigma E_i \eta_i^2)/(\Sigma E_i) - ((\Sigma E_i \eta_i)/(\Sigma E_i))^2}$, where E_i is the energy and η_i is the pseudorapidity of cell i and the sum is calculated within a window of 3×5 cells	$w_{\eta 2}$	x	x		LH
	Ratio of the energy in 3×3 cells over the energy in 3×7 cells centred at the electron cluster position	R_ϕ	x	x		LH
	Ratio of the energy in 3×7 cells over the energy in 7×7 cells centred at the electron cluster position	R_η	x	x	x	LH
First layer of EM calorimeter	Shower width, $\sqrt{(\Sigma E_i (i - i_{\mathrm{max}})^2)/(\Sigma E_i)}$, where i runs over all strips in a window of $\Delta\eta \times \Delta\phi \approx 0.0625 \times 0.2$, corresponding typically to 20 strips in η, and i_{max} is the index of the highest-energy strip, used for $E_{\mathrm{T}} > 150$ GeV only	w_{stot}	x	x	x	C
	Ratio of the energy difference between the maximum energy deposit and the energy deposit in a secondary maximum in the cluster to the sum of these energies	E_{ratio}	x	x		LH
	Ratio of the energy in the first layer to the total energy in the EM calorimeter	f_1	x			LH

Table 1 continued

Type	Description	Name	Rejects			Usage
			LF	γ	HF	
Track conditions	Number of hits in the innermost pixel layer	n_{Blayer}		x		C
	Number of hits in the pixel detector	n_{Pixel}		x		C
	Total number of hits in the pixel and SCT detectors	n_{Si}		x		C
	Transverse impact parameter relative to the beam-line	d_0		x	x	LH
	Significance of transverse impact parameter defined as the ratio of d_0 to its uncertainty	$\lvert d_0/\sigma(d_0)\rvert$		x	x	LH
	Momentum lost by the track between the perigee and the last measurement point divided by the momentum at perigee	$\Delta p/p$	x			LH
TRT	Likelihood probability based on transition radiation in the TRT	eProbabilityHT	x			LH
Track–cluster matching	$\Delta\eta$ between the cluster position in the first layer and the extrapolated track	$\Delta\eta_1$	x	x		LH
	$\Delta\phi$ between the cluster position in the second layer of the EM calorimeter and the momentum-rescaled track, extrapolated from the perigee, times the charge q	$\Delta\phi_{\text{res}}$	x	x		LH
	Ratio of the cluster energy to the track momentum, used for $E_{\text{T}} >$ 150 GeV only	E/p	x	x		C

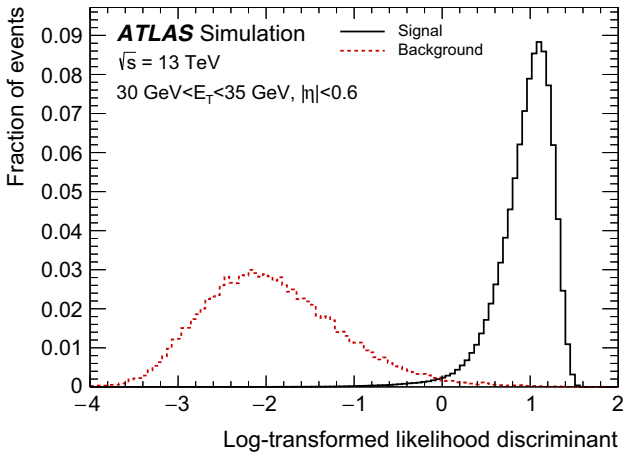

Fig. 5 The transformed LH-based identification discriminant d_L' for reconstructed electron candidates with good quality tracks with 30 GeV $< E_{\text{T}} <$ 35 GeV and $|\eta| < 0.6$. The black histogram is for prompt electrons in a $Z \to ee$ simulation sample, and the red (dashed-line) histogram is for backgrounds in a generic two-to-two process simulation sample (both simulation samples are described in Sect. 3). The histograms are normalised to unit area

pdfs for $E_{\text{T}} > 15$ GeV are determined using $Z \to ee$ Monte Carlo simulation.

6.3 LH-identification operating points and their corresponding efficiencies

To cover the various required prompt-electron signal efficiencies and corresponding background rejection factors needed by the physics analyses carried out within the ATLAS Collaboration, four fixed values of the LH discriminant are used to define four operating points. These operating points are referred to as VeryLoose, Loose, Medium, and Tight in the text below, and correspond to increasing thresholds for the LH discriminant. The numerical values of the discriminant are determined using the simulation. As shown in more detail later in this section, the efficiencies for identifying a prompt electron with $E_{\text{T}} = 40$ GeV are 93%, 88%, and 80% for the Loose, Medium, and Tight operating points, respectively.

The identification is optimised in bins of cluster η (specified in Table 2) and bins of E_{T} (specified in Table 3). The selected bins in cluster η are based on calorimeter geometry, detector acceptances and the variation of the material in the

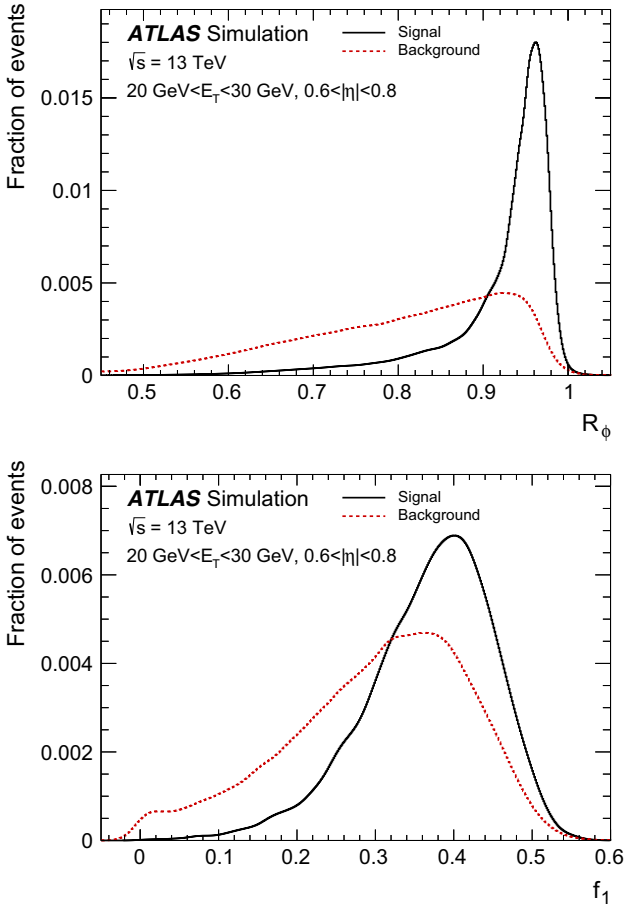

Fig. 6 Examples of distributions of two quantities R_ϕ (top) and f_1 (bottom), both defined in Table 1 and shown for 20 GeV $< E_{\mathrm{T}} <$ 30 GeV and $0.6 < |\eta| < 0.8$, that would be inefficient if used in a cut-based identification, but which, nonetheless, have significant discriminating power against background and, therefore, can be used to improve a LH-based identification. In each figure, the red-dashed distribution is determined from a background simulation sample and the black-line distribution is determined from a $Z \rightarrow ee$ simulation sample. These distributions are for reconstructed electron candidates before applying any identification. They are smoothed using an adaptive KDE and have been corrected for offsets or differences in widths between the distributions in data and simulation as described in Sect. 6.2

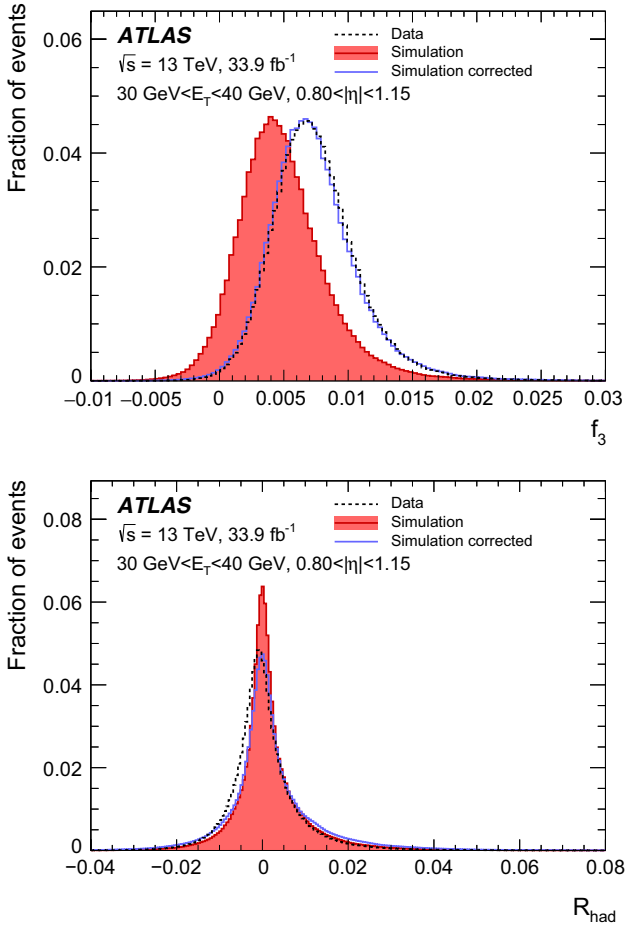

Fig. 7 The f_3 (top) and R_{had} (bottom) pdf distributions in data and simulation for prompt electrons that satisfy 30 GeV $< E_{\mathrm{T}} <$ 40 GeV and $0.80 < |\eta| < 1.15$. The distributions for both simulation and data are obtained using the $Z \rightarrow ee$ tag-and-probe method. KDE smoothing has been applied to all distributions. The simulation is shown before (shaded histogram) and after (open histogram) applying a constant shift (f_3, top) and a width-scaling factor (R_{had}, bottom). Although some $|\eta|$ bins of f_3 additionally have a width-scaling factor, this particular $|\eta|$ bin only has a constant shift applied

inner detector. The pdfs of the various electron-identification quantities vary with particle energy, which motivates the bins in E_{T}. The rate and composition of the background also varies with η and E_{T}.

To have a relatively smooth variation of electron-identification efficiency with electron E_{T}, the discriminant requirements are varied in finer bins (specified in Table 3) than the pdfs. To avoid large discontinuities in electron-identification efficiency at the bin boundaries in electron E_{T}, the pdf values and discriminant requirements are linearly interpolated between the centres of two adjacent bins in E_{T}.

All of the operating points have fixed requirements on tracking criteria: the Loose, Medium, and Tight operating points require at least two hits in the pixel detector and seven hits total in the pixel and silicon-strip detectors combined. For the Medium and Tight operating points, one of these pixel hits must be in the innermost pixel layer (or in the next-to-innermost layer if the innermost layer is non-operational). This requirement helps to reduce the background from photon conversions. A variation of the Loose operating point—LooseAndBLayer—uses the same threshold for the LH discriminant as the Loose operating point and also adds the requirement of a hit in the innermost pixel layer. The VeryLoose operating point does not include an explicit requirement on the innermost pixel layer and requires only one hit in the pixel detector; the goal of this operating point is to provide relaxed identification requirements for background studies.

Table 2 Boundaries in absolute cluster pseudorapidity used to define the nine bins for the LH pdfs and LH discriminant requirements

Bin boundaries in $\|\eta\|$									
0.0	0.6	0.8	1.15	1.37	1.52	1.81	2.01	2.37	2.47

The pdfs of some of the LH quantities—particularly R_{had} and R_η—are affected by additional activity in the calorimeter due to pile-up, making them more background-like. The number of additional inelastic pp collisions in each event is quantified using the number of reconstructed primary vertices n_{vtx}. In each η bin and E_{T} bin, the LH discriminant d_L' is adjusted to include a linear variation with n_{vtx}. Imposing a constraint of constant prompt-electron efficiency with n_{vtx} leads to an unacceptable increase in backgrounds. Instead, the background efficiency is constrained to remain approximately constant as a function of n_{vtx}, and this constraint results in a small (≤ 5 %) decrease in signal efficiency with n_{vtx}.

The minimum E_{T} of the electron identification was reduced from 7 GeV in Run 1 to 4.5 GeV in Run 2. The use of $J/\psi \to ee$ to determine LH pdfs at low E_{T} is also new in Run 2. The push towards lower E_{T} was motivated in part by searches for supersymmetric particles in compressed scenarios. In these scenarios, small differences between the masses of supersymmetric particles can lead to leptons with low transverse momentum.

Special treatment is required for electrons with $E_{\text{T}} > 80$ GeV. The f_3 quantity (defined in Table 1) degrades the capability to distinguish signal from background because high-E_{T} electrons deposit a larger fraction of their energy in the third layer of the EM calorimeter (making them more hadron-like) than low-E_{T} electrons. For this reason and since it is not modelled well in the simulation, the pdf for f_3 is removed from the LH for $E_{\text{T}} > 80$ GeV. Furthermore, changes with increasing prompt-electron E_{T} in the R_{had} and f_1 quantities cause a large decrease in identification efficiency for $E_{\text{T}} > 300$ GeV. Studies during development of the identification algorithm showed that this loss in efficiency was very large for the Tight operating point (the identification efficiency fell from 95% at $E_{\text{T}} = 300$ GeV to 73% for $E_{\text{T}} = 2000$ GeV). To mitigate this loss, for electron candidates with $E_{\text{T}} > 150$ GeV, the LH discriminant threshold for the Tight operating point is set to be the same as for the Medium operating point, and two additional selection criteria are added to the Tight selection: E/p and w_{stot}. The requirement on w_{stot} depends on the electron candidate η, while the requirement on E/p is $E/p < 10$. The high value of the latter requirement takes into account the decreased momentum resolution in track fits of a few 100 GeV and above. With these modifications, good signal efficiency and background rejection are maintained for very high E_{T} electrons in searches for physics beyond the Standard Model, such as $W' \to e\nu$.

In Run 1, electron candidates satisfying tighter operating points did not necessarily satisfy the more efficient looser operating points. This situation was a result of using different quantities in the electron LH for the different operating points. In Run 2, electron candidates satisfying tighter operating points also satisfy less restrictive operating points, i.e. an electron candidate that satisfies the Tight criteria will also pass the Medium, Loose, and VeryLoose criteria.

Another important difference in the electron identification between Run 1 and Run 2 is that the LH identification is used in the online event selection (the high-level trigger, HLT) in Run 2, instead of a cut-based identification in Run 1. This change helps to reduce losses in efficiency incurred by applying the offline identification criteria in addition to the online criteria. The LH identification in the trigger is designed to be as close as possible to the LH used in offline data analysis; however, there are some important differences. The $\Delta p/p$ quantity is removed from the LH because it relies on the GSF algorithm (see Sect. 5.2), which is too CPU-intensive for use in the HLT. The average number of interactions per bunch crossing, $\langle\mu\rangle$, is used to quantify the amount of pile-up, again because the determination of the number of primary vertices, n_{vtx}, is too CPU-intensive for the HLT. Both the d_0 and $d_0/\sigma(d_0)$ quantities are removed from the LH used in the trigger in order to preserve efficiency for electrons from exotic processes which might have non-zero track impact parameters. Finally, the LH identification in the trigger uses quantities reconstructed in the trigger, which generally have poorer resolution than the same quantities reconstructed offline. The online operating points corresponding to VeryLoose, Loose, Medium, and Tight are designed to have efficiencies relative to reconstruction like those of the corresponding offline operating points. Due to these differences, the inefficiency of the online selection for electrons fulfilling the same operating point as the offline selection is typically a few percent (absolute), up to 7% for the Tight operating point.

The efficiencies of the LH-based electron identification for the Loose, Medium, and Tight operating points for data and the corresponding data-to-simulation ratios are summarised in Figs. 8 and 9. They are extracted from $J/\psi \to ee$ and $Z \to ee$ events, as discussed in Sect. 4. The variations of the efficiencies with E_{T}, η, and the number of reconstructed primary vertices are shown. Requirements on the transverse (d_0) and longitudinal (z_0) impact parameters measured as the distance of closest approach of the track to the measured primary vertex (taking into account the beam-spot and the tilt of the beam-line) are applied when evaluating the numerator of the identification efficiency. For the Tight operating point, the identification efficiency varies from 55% at $E_{\text{T}} = 4.5$ GeV to 90% at $E_{\text{T}} = 100$ GeV, while it ranges from 85% at

Table 3 Boundaries in electron transverse energy used to define the seven bins for the LH pdfs and the twelve bins for LH discriminant requirements

Bin boundaries in E_T [GeV]													
pdfs	4.5	7	10	15	20		30		40				∞
Discriminant	4.5	7	10	15	20	25	30	35	40	45	80	150	∞

$E_T = 20$ GeV to 96% at $E_T = 100$ GeV for the Loose operating point. The uncertainties in these measured efficiencies for the Loose (Tight) operating point range from 3% (4%) at $E_T = 4.5$ GeV to 0.1% (0.3%) for $E_T = 40$ GeV. As mentioned earlier in this section, simulation was used to determine the discriminant values that define the various operating points, with the intended outcome that the efficiencies would fall smoothly with decreasing electron E_T, while keeping the rapidly increasing background at acceptable levels. The simple offsets and width variations applied to the simulation to account for mismodelling of the EM-calorimeter shower shapes (see Sect. 6.2) work well at higher electron E_T, but are unable to fully correct the simulation at lower electron E_T. This leads to an unintended larger efficiency in data for signal electrons at lower E_T, as can be seen in Fig. 8. The figure also shows the corresponding rise in the data-to-simulation ratios.

The lower efficiencies of the Medium and Tight operating points compared to Loose result in an increased rejection of background; the rejection factors for misidentified electrons from multijet production (evaluated with the two-to-two process simulation sample described in Sect. 3) increase typically by factors of approximately 2.5 for Medium and 5 for Tight compared to Loose, in the E_T range of 4–50 GeV. Computations and measurements of the rejection, especially absolute rejections, are typically associated with large uncertainties due to ambiguities in the definition of the denominator, and the diversity of the sources of background. The factors mentioned above are similar to those published in Table 3 of the ATLAS Run-1 publication [3] when these considerations are taken into account.

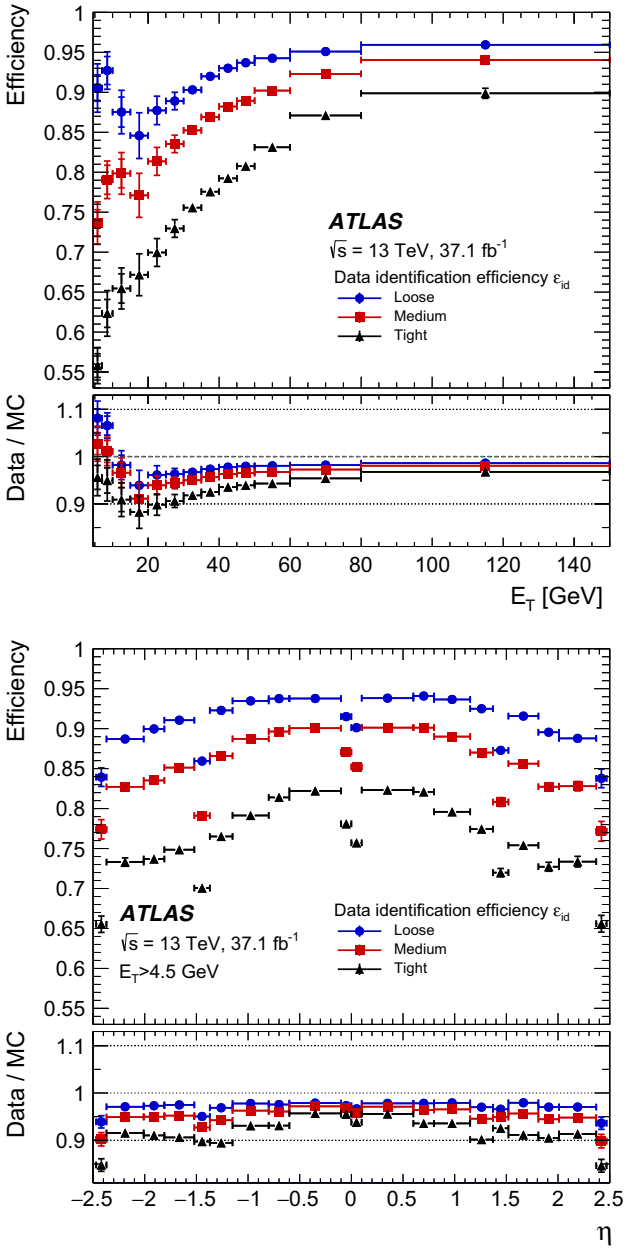

Fig. 8 Measured LH electron-identification efficiencies in $Z \to ee$ events for the Loose (blue circle), Medium (red square), and Tight (black triangle) operating points as a function of E_T (top) and η (bottom). The vertical uncertainty bars (barely visible because they are small) represent the statistical (inner bars) and total (outer bars) uncertainties. The data efficiencies are obtained by applying data-to-simulation efficiency ratios that are measured in $J/\psi \to ee$ and $Z \to ee$ events to the $Z \to ee$ simulation. For both plots, the bottom panel shows the data-to-simulation ratios

7 Electron isolation

A considerable challenge at the LHC experiments is to differentiate the prompt production of electrons, muons, and photons in signal processes (from the hard-scattering vertex, or from the decay of heavy resonances such as Higgs, W, and Z bosons) from background processes such as semileptonic decays of heavy quarks, hadrons misidentified as leptons and photons, and photons converting into electron–positron pairs in the detector material upstream of the electromagnetic calorimeter. A characteristic signature of such a signal is represented by little activity (both in the calorimeter and in the inner detector) in an area of $\Delta\eta \times \Delta\phi$ surrounding

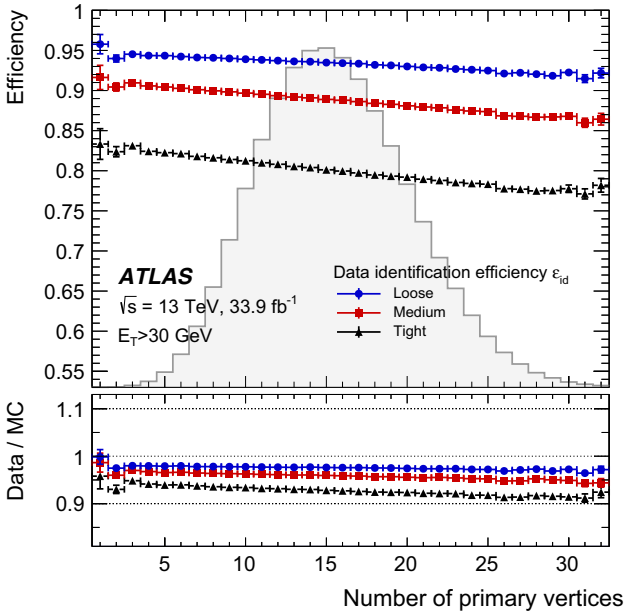

Fig. 9 The LH electron-identification efficiencies for electron candidates with $E_{\mathrm{T}} > 30\,\mathrm{GeV}$ for the Loose (blue circle), Medium (red square), and Tight (black triangle) operating points as a function of the number of primary vertices in the 2016 data using the $Z \to ee$ process. The shaded histogram shows the distribution of the number of primary vertices for the 2016 data. The inner uncertainties are statistical while the total uncertainties include both the statistical and systematic components. The bottom panel shows the data-to-simulation ratios

the candidate object. However, the production of boosted particles decaying, for example, into collimated electron–positron pairs or the production of prompt electrons, muons, and photons within a busy experimental environment such as in $t\bar{t}$ production can obscure the picture. Variables are constructed that quantify the amount of activity in the vicinity of the candidate object, something usually performed by summing the transverse energies of clusters in the calorimeter or the transverse momenta of tracks in a cone of radius $\Delta R = \sqrt{(\Delta\eta)^2 + (\Delta\phi)^2}$ around the direction of the electron candidate, excluding the candidate itself.

Several components enter into building such isolation variables: identifying the candidate object itself, its direction, and its contribution to the activity within the cone, and summing, in a pile-up and underlying-event robust way, the other activity found within the cone. The two classes of isolation variables considered in this paper are based on calorimeter and tracking measurements, and are respectively discussed in Sects. 7.1 and 7.2.

7.1 Calorimeter-based isolation

The reconstruction of electron candidates is described in Sect. 5. To build an isolation variable, a cone of size ΔR is then delineated around the candidate electron's cluster position.

The computation of calorimeter-based isolation in the early running period of ATLAS simply summed the transverse energies of the calorimeter cells (from both the electromagnetic and hadronic calorimeters) within a cone aligned with the electron direction, excluding the candidate's contribution. This type of calorimeter-based variable exhibited a lack of pile-up resilience and demonstrated poor data–simulation agreement. A significant improvement was achieved by using the transverse energies of topological clusters [38] instead of cells, thus effectively applying a noise-suppression algorithm to the collection of cells.

Topological clusters are seeded by cells with a deposited electromagnetic-scale energy of more than four times the expected noise-level threshold of that cell; this includes both electronic noise and the effects of pileup. The clusters are then expanded, in the three spatial directions across all electromagnetic and hadronic calorimeter layers, by iteratively adding neighbouring cells that contain a deposited energy more than twice the noise level. After the expansion around the cluster stops due to a lack of cells satisfying the energy threshold requirements, a final shell of cells surrounding the agglomeration is added to the cluster. The topological clusters used in the isolation computation are not further calibrated: they remain at the electromagnetic scale, regardless of the origin of the particle.

The energies of all positive-energy topological clusters, whose barycentres fall within the cone of radius ΔR, as illustrated in Fig. 10, are summed into the raw isolation energy variable $E_{\mathrm{T,raw}}^{\mathrm{isol}}$. This raw isolation energy still includes the energy deposited by the candidate electron, called the core energy $E_{\mathrm{T,core}}$. The core energy is subtracted by removing the cells included in a $\Delta\eta \times \Delta\phi = 0.125 \times 0.175$ rectangle around the candidate's direction, as illustrated in Fig. 10. The advantage of this method is its simplicity and stable subtraction scheme for both the signal and background candidates. A disadvantage of this method is that the candidate object may deposit energy outside of this fixed rectangular area which may be incorrectly assigned as additional activity, requiring an additional leakage correction to the subtracted core energy. The core leakage correction is evaluated using samples of simulated single electrons (without additional pile-up activity). The energy leaking into the cone is then fit to a Crystal Ball function; its most probable value μ_{CB} is parameterised as a function of E_{T} and is used as an estimator of the average leakage, $E_{\mathrm{T,leakage}}(E_{\mathrm{T}})$. The corrections are derived in ten bins of the associated cluster η position.

Figure 11 shows the isolation energy corrected with a rectangular core, without and with the calculated leakage correction, as a function of the electron E_{T} for a sample of simulated single electrons which includes the effects of pile-up; a

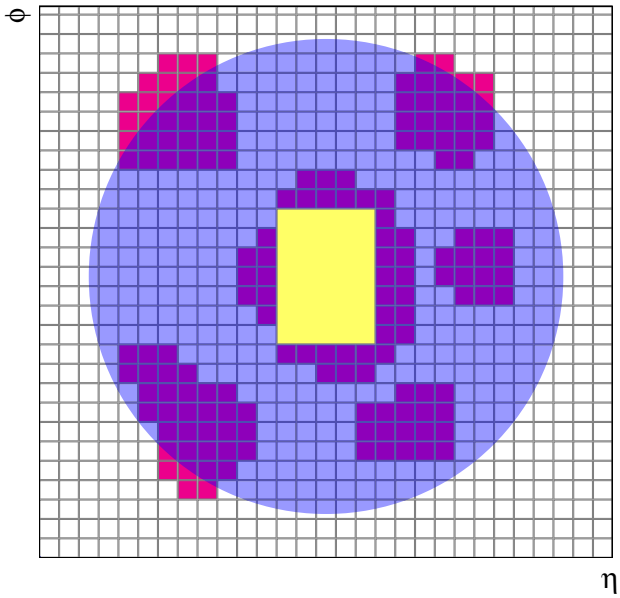

Fig. 10 Schema of the calorimeter isolation method: the grid represents the second-layer calorimeter cells in the η and ϕ directions. The candidate electron is located in the centre of the purple circle representing the isolation cone. All topological clusters, represented in red, for which the barycentres fall within the isolation cone are included in the computation of the isolation variable. The 5×7 cells (which cover an area of $\Delta\eta \times \Delta\phi = 0.125 \times 0.175$) represented by the yellow rectangle correspond to the subtracted cells in the core subtraction method

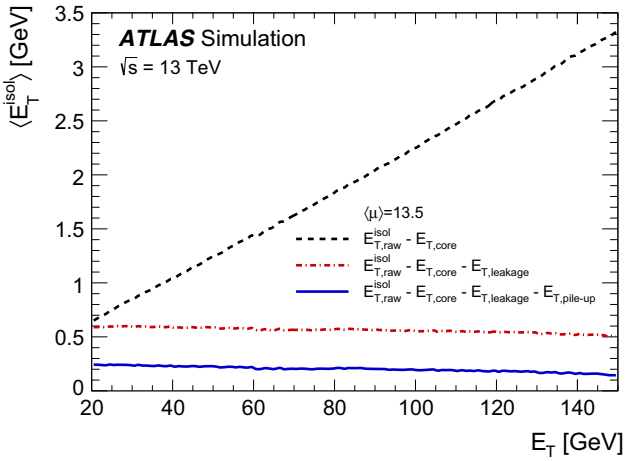

Fig. 11 Isolation transverse energy built with a cone of radius $\Delta R = 0.2$, corrected with a rectangular core without (black dashed line) and with (red dot-dashed line) the leakage correction $E_{\mathrm{T,leakage}}$ as a function of the electron E_{T}, for a simulated sample with electron candidates in the central region of the detector ($|\eta| < 2.47$) that satisfy a Tight electron identification criterion. This figure also shows the size of the pile-up correction $E_{\mathrm{T,pile\text{-}up}}$ (the difference between the red dot-dashed line and solid blue line). The curves were obtained from a simulated single-electron sample that includes the effects of $\langle\mu\rangle = 13.5$ pile-up

leakage correction is essential when using a rectangular core region.

The pile-up and underlying-event contribution to the isolation cone is estimated from the ambient energy density [39]. For each event, the entire calorimeter acceptance up to $|\eta| = 5$ is used to gather positive-energy topological clusters using the k_t jet-clustering algorithm [40,41] with radius parameter $R = 0.5$, with no jet p_{T} threshold. The area A of each jet is estimated and the transverse energy density ρ of each jet is computed as $\rho = p_{\mathrm{T}}/A$. The median energy density ρ_{median} of the distribution of jet densities in the event is used as an estimator of the transverse energy density of the event. For a simulated $Z \to ee$ sample at $\sqrt{s} = 13$ TeV with average pile-up $\langle\mu\rangle = 22$, ρ_{median} is approximately 4 GeV per unit of $\eta - \phi$ space in the central η region of the calorimeter, decreasing to 2 GeV at $|\eta| = 2.5$. The pile-up/underlying-event correction is then evaluated as:

$$E_{\mathrm{T,pile\text{-}up}}(\eta) = \rho_{\mathrm{median}}(\eta) \times \left(\pi \Delta R^2 - A_{\mathrm{core}}\right),$$

where ΔR is the radius of the isolation cone and A_{core} is the area of the signal core that was subtracted. The η dependence of ρ is estimated in two bins: $|\eta| < 1.5$ and $1.5 < |\eta| < 3.0$. Figure 11 shows the size of this pile-up correction for a simulated single-electron sample with $\langle\mu\rangle = 13.5$ pile-up.

The fully corrected calorimeter-based isolation variable $E_{\mathrm{T,cone}}^{\mathrm{isol}}$ calculated within the cone of radius ΔR is then obtained after subtracting the components described above, namely

$$E_{\mathrm{T,cone}}^{\mathrm{isol}} = E_{\mathrm{T,raw}}^{\mathrm{isol}} - E_{\mathrm{T,core}} - E_{\mathrm{T,leakage}} - E_{\mathrm{T,pile\text{-}up}}.$$

Figure 11 shows the resulting distribution as a function of the transverse energy of the electron for a simulated single-electron sample. The distribution is slightly positive since only positive-energy clusters are summed, allowing for only positive fluctuations from noise.

7.2 Track-based isolation

The computation of track-based isolation variables uses tracks with $p_{\mathrm{T}} > 1$ GeV, reconstructed within a fiducial region of the inner detector, $|\eta| < 2.5$, and that satisfy basic track-quality requirements. This track selection, optimised using candidate muons from simulated $t\bar{t}$ samples, includes a minimum number of hits identified in the silicon detectors and a maximum number of inoperable detector regions crossed by the track. In order to minimise the impact of pile-up, a requirement is placed on the longitudinal impact parameter, z_0, corrected for the reconstructed position of the primary vertex and multiplied by the sine of the track polar angle: $|z_0 \sin\theta| < 3$ mm. This requirement on $|z_0 \sin\theta|$ aims to select tracks that originate from the vertex that is chosen to be the relevant vertex of the process. In most cases, the rele-

vant vertex corresponds to the "hardest" vertex of the event, i.e. the vertex for which the sum of the squares of the transverse momenta of the associated tracks is the largest; this is the vertex used by default in the track-isolation computation. Track-based isolation variables are constructed by summing the transverse momenta of the tracks found within a cone of radius ΔR aligned with the electron track, excluding the candidate's own contribution.

The track-p_{T} contribution of the candidate electron to the track-isolation variable must be subtracted from the cone. Electrons can undergo bremsstrahlung radiation with the radiated photons converting into secondary electrons; such additional particles should be counted as part of the initial particle's energy. For this reason, tracks are extrapolated to the second layer of the EM calorimeter. All extrapolated tracks that fall within a $\Delta\eta \times \Delta\phi = 0.05 \times 0.1$ window around the cluster position are considered to be part of the candidate and are removed from the track-isolation-variable computation. The resulting track-isolation variable is called $p_{\mathrm{T}}^{\mathrm{isol}}$.

Unlike calorimeter isolation, where a cone with a radius much less than $\Delta R = 0.2$ is difficult to build due to the finite granularity of the calorimeter, the much smaller tracker granularity allows the use of narrower cone sizes. For example, in boosted decay signatures or very busy environments, other objects can be close to the signal lepton direction. For such cases, a variable-cone-size track isolation, $p_{\mathrm{T,var}}^{\mathrm{isol}}$, can be used, one that progressively decreases in size as a function of the p_{T} of the candidate:

$$\Delta R = \min\left(\frac{10\ \mathrm{GeV}}{p_{\mathrm{T}}[\mathrm{GeV}]}, R_{\mathrm{max}}\right),$$

where R_{max} is the maximum cone size (typically 0.2–0.4). The value of 10 GeV in the argument is derived with a simulated $t\bar{t}$ sample, and designed to maximise the rejection of background.

7.3 Optimisation of isolation criteria and resulting efficiency measurements

The implementation of isolation criteria is specific to the physics analysis needs, be it to identify isolated prompt electrons or electrons produced in a busy environment, or to reject light hadrons misidentified as electrons. Precision measurements with copious signal at lower p_{T} may favour tighter isolation requirements, and be willing to sacrifice some signal in order to ensure high background rejection, whereas searches at high p_{T} may instead favour looser requirements in order to maintain high signal efficiency. Therefore, several isolation operating points were established that use calorimeter-based isolation in a cone of radius $\Delta R = 0.2$ (Sect. 7.1) or track-based isolation using a variable-size cone with $R_{\mathrm{max}} = 0.2$ or 0.4 (Sect. 7.2), or both types of isolation simultaneously. The requirements for each efficiency-targeted operating point are established in bins of electron E_{T} and η with edges:

- E_{T} [GeV]: 7, 10, 15, 20, 25, 27.5, 30, 32.5, 35–45 (1 GeV bins), 47.5, 50, 60, 80, ∞,
- $|\eta|$: 0, 0.1, 0.6, 0.8, 1.15, 1.37, 1.52, 1.81, 2.01, 2.37, 2.47.

The operating points are defined in three categories:

- targeting a fixed value of the isolation efficiency ϵ_{iso}, uniform in the E_{T}, η of the electron ('Loose' isolation),
- targeting a fixed value of the isolation efficiency ϵ_{iso}, dependent on the E_{T} of the electron but uniform in η ('Gradient' isolation),
- imposing fixed requirements on the value of the isolation variable ('Fix').

Figure 12 shows the isolation efficiencies measured in data and the corresponding data-to-simulation ratios as a function of the electron E_{T} and η for the operating points given in Table 4 and for candidate electrons satisfying Tight identification requirements. The efficiencies that determine the values of the requirements given in Table 4 are evaluated in simulation from a $J/\psi \to ee$ sample for $E_{\mathrm{T}} < 15$ GeV and from a $Z \to ee$ sample for $E_{\mathrm{T}} > 15$ GeV. Since the value of the efficiency is process dependent, this can result in a jump in efficiency at the transition point of $E_{\mathrm{T}} = 15$ GeV, as can be seen in the top-left plot of Fig. 12, which was produced with a $Z \to ee$ sample over the full E_{T} range. The overall differences between data and simulation are less than approximately 2–4%; the operating point 'Fix (Tight)' has the most significant difference in shape in η.

8 Electron-charge identification

8.1 Reconstruction of electric charge

The electric charge of an electron is determined from the curvature of the associated track reconstructed in the inner detector. The misidentification of electron charge can result from the matching of an incorrect track to the electron candidate or from a mismeasurement of the curvature of the primary electron track.

The probability of bremsstrahlung emission and subsequent photon conversion to an electron–positron pair (see Sect. 5) depends significantly on the amount of detector material traversed. As shown in Fig. 13 (top, left) for a simulated $Z \to ee$ sample, most electrons for which the wrong charge was assigned are found in the pseudorapidity region

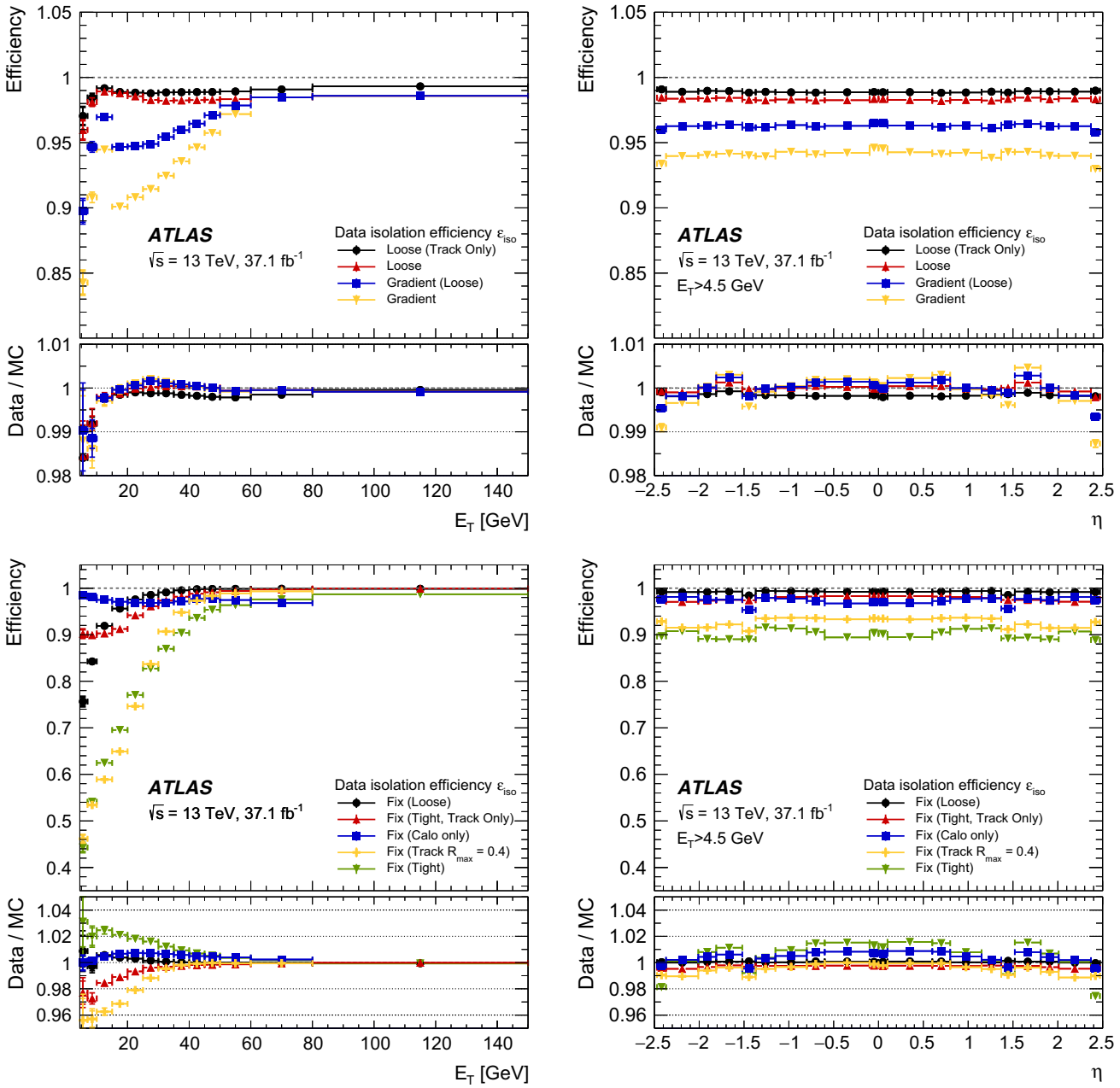

Fig. 12 Isolation efficiencies for data (in the upper panels) and the ratio to simulation (lower panels) for the operating points given in Table 4 as a function of candidate-electron E_{T} (left) and η (right) in $Z \to ee$ events. Top plots: efficiencies for optimised operating points targeting specific efficiencies. Bottom plots: efficiencies for operating points where fixed requirements are applied to the isolation variables. Cone sizes of $\Delta R = 0.2$ for calorimeter isolation and $R_{\mathrm{max}} = 0.2$ for track isolation are used (except for "Fix (Track $R_{\mathrm{max}} = 0.4$)" where a twice larger radius cone is used). The inner uncertainties are statistical while the total uncertainties include both the statistical and systematic components

$1.5 < |\eta| < 2.2$, corresponding to a region in the detector with a relatively large amount of inactive material.

Pair production resulting from bremsstrahlung is the main reason why a wrong track can be matched to the electron candidate; three tracks in close proximity are present, two of which have the correct charge assignment, causing an ambiguity in the selection of the primary electron track. In this context, "correct track" means the primary electron track while "correct charge" means the track has the same reconstructed charge as the primary electron. The number of reconstructed tracks passing the requirements described in Sect. 5.3 is shown in Fig. 13 (top, right); events with electrons

Table 4 Definition of the electron-isolation operating points and isolation efficiency ϵ_{iso}. For the 'Gradient' operating points, the units of p_{T} are GeV. All operating points use a cone size of $\Delta R = 0.2$ for calorimeter isolation and $R_{\text{max}} = 0.2$ for track isolation except for the final entry 'Fix (Track)' which uses $R_{\text{max}} = 0.4$. The values are obtained from a simulated $Z \to ee$ sample where electrons satisfy Tight identification requirements

Operating point	$E_{\text{T,cone}}^{\text{isol}}$ ($\Delta R = 0.2$)	$p_{\text{T,var}}^{\text{isol}}$ ($R_{\text{max}} = 0.2$)	Total ϵ_{iso}
Loose (Track Only)	–	$\epsilon_{\text{iso}} = 99\%$	99%
Loose	$\epsilon_{\text{iso}} = 99\%$	$\epsilon_{\text{iso}} = 99\%$	98%
Gradient	$\epsilon_{\text{iso}} = 0.1143 \times p_{\text{T}} + 92.14\%$	$\epsilon_{\text{iso}} = 0.1143 \times p_{\text{T}} + 92.14\%$	90(99)% at 25(60) GeV
Gradient (Loose)	$\epsilon_{\text{iso}} = 0.057 \times p_{\text{T}} + 95.57\%$	$\epsilon_{\text{iso}} = 0.057 \times p_{\text{T}} + 95.57\%$	95(99)% at 25(60) GeV
Fix (Loose)	$E_{\text{T,cone}}^{\text{isol}}/p_{\text{T}} < 0.20$	$p_{\text{T,var}}^{\text{isol}}/p_{\text{T}} < 0.15$	–
Fix (Tight)	$E_{\text{T,cone}}^{\text{isol}}/p_{\text{T}} < 0.06$	$p_{\text{T,var}}^{\text{isol}}/p_{\text{T}} < 0.06$	–
Fix (Tight, Track Only)	–	$p_{\text{T,var}}^{\text{isol}}/p_{\text{T}} < 0.06$	–
Fix (Calo Only)	$E_{\text{T,cone}}^{\text{isol}} < 3.5$ GeV	–	–
Fix (Track $R_{\text{max}} = 0.4$)	$E_{\text{T,cone}}^{\text{isol}}/p_{\text{T}} < 0.11$	$p_{\text{T,var}}^{\text{isol}}/p_{\text{T}} < 0.06$	–

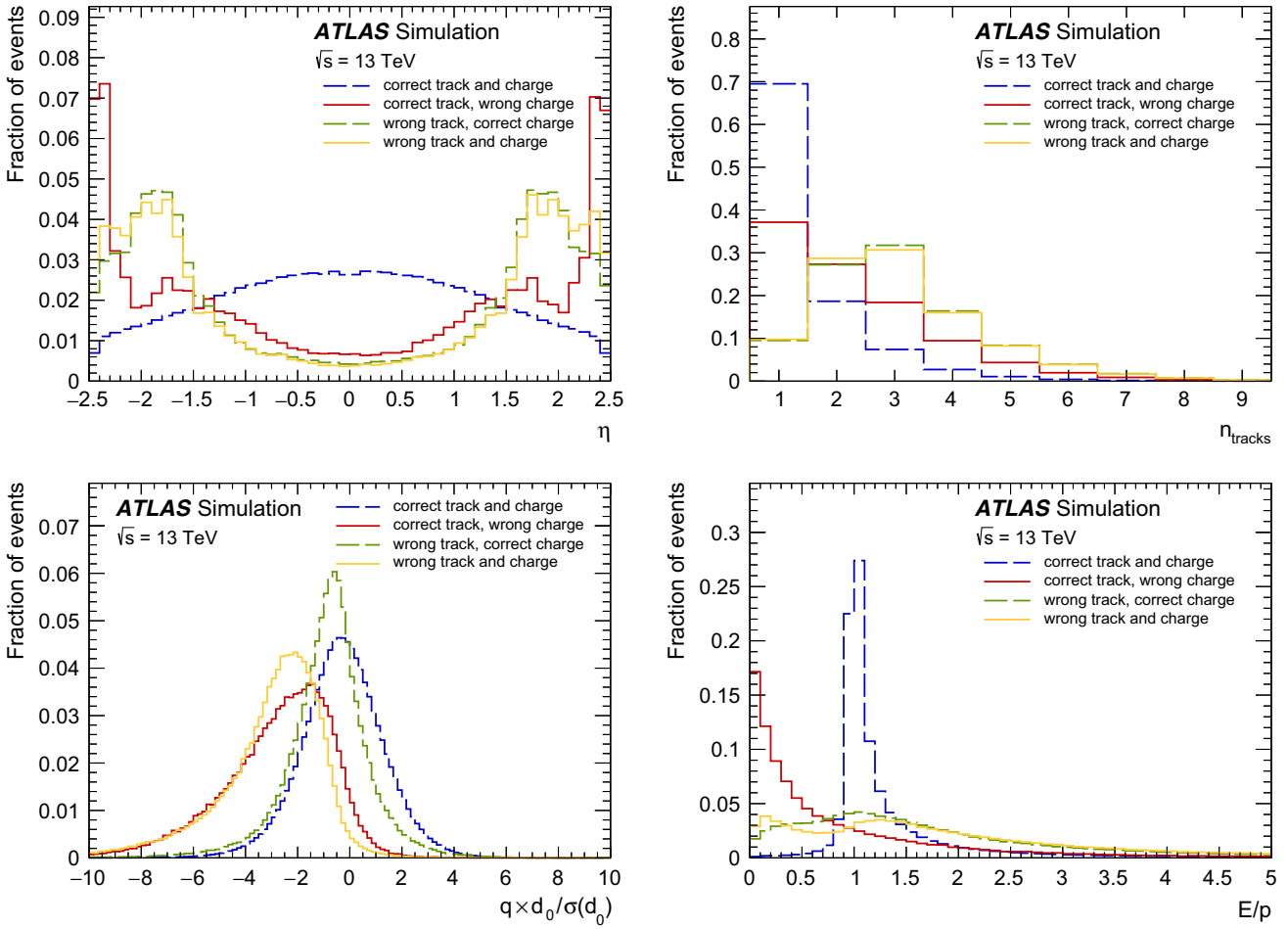

Fig. 13 Kinematic and tracking properties of electrons from a simulated $Z \to ee$ sample. Top, left: track pseudorapidity. Top, right: multiplicity of associated tracks. Bottom, left: electric charge multiplied by the transverse impact parameter significance. Bottom, right: energy-to-momentum ratio, in each case for electrons with the correctly and incorrectly reconstructed charge with respect to the particle that caused the track and the correctly and incorrectly assigned track with respect to the primary electron. The distributions are normalised to the same area

that have a wrongly assigned track tend to have higher track multiplicities. Electrons produced in conversions of photons originating from the primary electron have a most probable value of three tracks regardless of whether the charge was correctly reconstructed or not, illustrating the probabilistic nature of the process.

The presence of additional electrons and positrons in close proximity can cause the track to be reconstructed from hits of primary and secondary electrons and positrons. Significant energy loss can also distort the shape of the track. At very high energies or large pseudorapidities, the tracks can also become straighter and hence it is difficult to determine their curvature. All of these effects impact the ability to correctly fit the track, as can be seen from the comparison of the correct charge and wrong charge distributions for the correctly assigned track. These effects are more pronounced as a function of increased passive material, located at large values of η, as shown by comparing the equivalent two distributions in Fig. 13 (top, left).

Figure 13 (bottom, left) and (bottom, right) show the distributions of the electric charge multiplied by the transverse impact parameter significance $q \times d_0/\sigma(d_0)$ and the E/p, respectively, for electron candidates with correctly and incorrectly reconstructed charge and assigned track. As expected, electrons with incorrectly reconstructed charge tend to have a larger magnitude of $d_0/\sigma(d_0)$. Their $q \times d_0/\sigma(d_0)$ tends to be more negative due to the incorrect measurement of the electric charge. The distributions have a significant fraction of events with $E/p \neq 1$, due to either the wrong track being matched to the candidate electron or the wrong track curvature being measured, resulting in an erroneous measurement of the electron's momentum.

8.2 Suppression of charge misidentification

The charge-misidentification rate for reconstructed electron candidates can be reduced with an additional selection criterion based on the output discriminant of a boosted decision tree (BDT) trained using the TMVA toolkit. The training of the BDT is performed on a simulated single-electron sample. A set of eight variables related to the quality of the chosen primary electron track, the lateral development of the electromagnetic shower (which is expected to be narrower for electrons that don't undergo bremsstrahlung), and combined tracking and calorimeter quantities is used to separate electrons with the correctly reconstructed electric charge from those reconstructed with the wrong charge. The list of these quantities, ranked by their contribution to the discriminating power of the selection (highest to lowest, as evaluated with a simulated $Z \to ee$ sample), is: E/p, $\Delta\phi_{\text{res}}$, $q \times d_0$, the pseudorapidity η of the electron, R_ϕ, $(q/p)/\sigma(q/p)$, $\Delta\phi_1$, and the transverse energy E_{T} of the electron. Table 1 provides the definitions of these variables except for the charge-to-momentum ratio q/p divided by its uncertainty $\sigma(q/p)$ and the distance in ϕ between the cluster position in the first layer of the calorimeter and the extrapolated track, $\Delta\phi_1$.

The BDT parameters are optimised to achieve the best possible rejection of electrons reconstructed with the wrong charge given an efficiency loss of 3% for electrons with correctly reconstructed charge. The resulting efficiencies from applying the additional BDT requirement for electrons already identified with a Medium requirement (see Sect. 6) are shown in Fig. 14 for candidate electrons from $Z \to ee$ events. The inclusion of the kinematic properties E_{T} and η in the BDT introduces a dependence of the efficiency on these quantities (in particular for η), even for electron candidates reconstructed with the correct charge. The differences observed between data and simulation arise not only from mismodelling of some of the electromagnetic shower shapes in the simulation but also from the modelling of complicated objects such as the beam-spot. For this reason, data-to-simulation scale factors are calculated; they are also shown in Fig. 14. At very high $|\eta|$, the efficiency in data is approximately 76%. The corresponding efficiency in simulation is about 8% higher, due to mismodelling. Analyses using same-charge dilepton pairs such as searches for supersymmetry in same-charge signatures [42] or the search for Higgs boson production in association with a top-quark pair [43] benefit from a suppression of electrons from charge misidentification with the BDT requirement.

8.3 Measurement of the probability of charge misidentification

A measurement of the probability of charge misidentification is performed using a sample of $Z \to ee$ events where both electrons are required to satisfy the same identification and isolation criteria. The probability ϵ for an electron to be reconstructed with the wrong charge in a given (η, E_{T}) bin is obtained from the numbers of events where both electrons have the same (SC) and opposite electric charges (OC). The average *expected* number of same-charge events for a pair of electrons falling into their respective (η, E_{T}) bins i and j, N_{ij}^{SC}, follows from the total number of *observed* events $n_{ij}^{\text{OC+SC}}$ in these same two (η, E_{T}) bins regardless of charge, corrected for the charge-misidentification probability in each bin $\epsilon_{i,j}$:

$$N_{ij}^{\text{SC}} = n_{ij}^{\text{OC+SC}}[(1-\epsilon_i)\epsilon_j + (1-\epsilon_j)\epsilon_i].$$

The probabilities ϵ_i and ϵ_j are obtained by maximising the Poisson likelihood to observe the number of same-charge events n_{ij}^{SC} in these bins. The non-prompt-background contributions to n_{ij}^{OC} and n_{ij}^{SC} are estimated by taking equal-size sideband invariant-mass regions about the Z-boson peak and

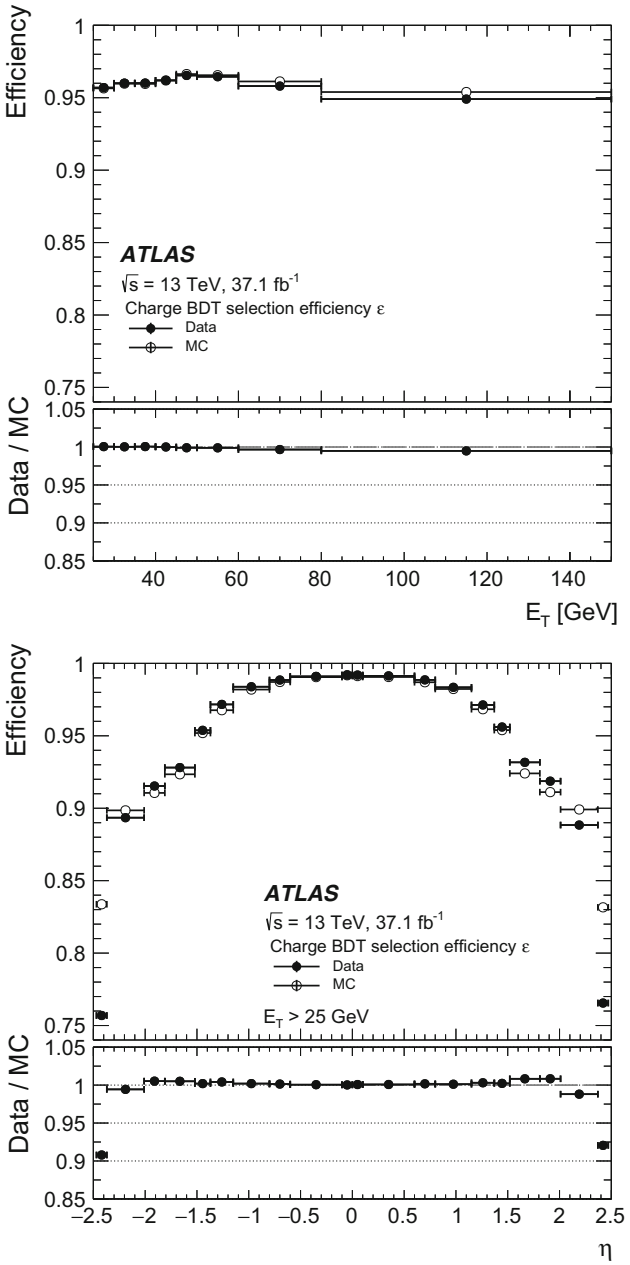

Fig. 14 Efficiency of applying the additional BDT selection criterion to choose Medium-identified electrons reconstructed with the correct charge, as evaluated in $Z \to ee$ events. The criterion is based on a BDT discriminant optimised to select electrons with a correct charge assignment with an efficiency of 97%. Top: vs. E_{T}; bottom: vs. η. Open points: data; closed points: simulation; and lower panels: data-to-simulation ratios. The uncertainties are smaller than the markers and hence not visible

linearly interpolating to estimate the number of events under the mass peak.

Systematic uncertainties associated with the Z-boson mass window are evaluated by increasing and decreasing its range. Systematic uncertainties from other sources are evaluated by not performing the background subtraction, by taking differences between probabilities in events where both electrons fired the trigger and probabilities in events where only one electron fired the trigger, and by comparing the charge-misidentification rates extracted using the likelihood method with the rates extracted from a comparison with the true charge as determined in simulation.

Figure 15 shows the charge-misidentification rates in data and simulation for Medium electrons in $Z \to ee$ events as a function of E_{T} and $|\eta|$, demonstrating the impact of applying the BDT requirement to suppress charge misidentification, as explained in Sect. 8.2. As expected, the charge-misidentification rates are larger at high E_{T} and $|\eta|$. Two identification operating points are also contrasted showing the impact of using a Tight identification requirement without the BDT requirement compared with using Medium identification but also including this BDT requirement.

The knowledge of electron charge-misidentification rates is crucial for the estimation of background from charge misidentification in measurements, e.g. in the observation of the electroweak $W^{\pm}W^{\pm}jj$ production [44] or the search for doubly charged Higgs boson production [45]. To account for disagreements between data and simulation, data-to-simulation ratios, extracted from the efficiencies described above, are provided as correction factors for analyses to account for this mismodelling in the simulation.

9 Usage of electron selections in physics measurements

Efficiencies for electron reconstruction, identification, isolation, and charge identification are shown for several operating points in Sects. 5, 6, 7, and 8, respectively. The product of these efficiencies (and their corresponding data-to-simulation correction factors) is relevant in physics measurements. In this section, electron efficiencies for data from a $Z \to ee$ sample are presented for the combination $\epsilon_{\mathrm{reco}} \times \epsilon_{\mathrm{id}} \times \epsilon_{\mathrm{iso}}$ (see Eq. (1)) for some typical operating points used in ATLAS physics analyses. The results are shown in Fig. 16 for the following operating points (listed as Identification + Isolation):

- Loose + Fix (Loose): used in cross-section measurements of $H \to 4\ell$ [46] and Standard Model ZZ production [47],
- Medium + Gradient (Loose): used in searches for direct top-squark-pair production in final states with two leptons [48] and to identify the Z-boson candidate in measurements of Standard Model WZ production [49],
- Tight + Gradient: used in measurements of single-top-quark production in association with a Z or W boson [50,51] and Standard Model WW production [52],

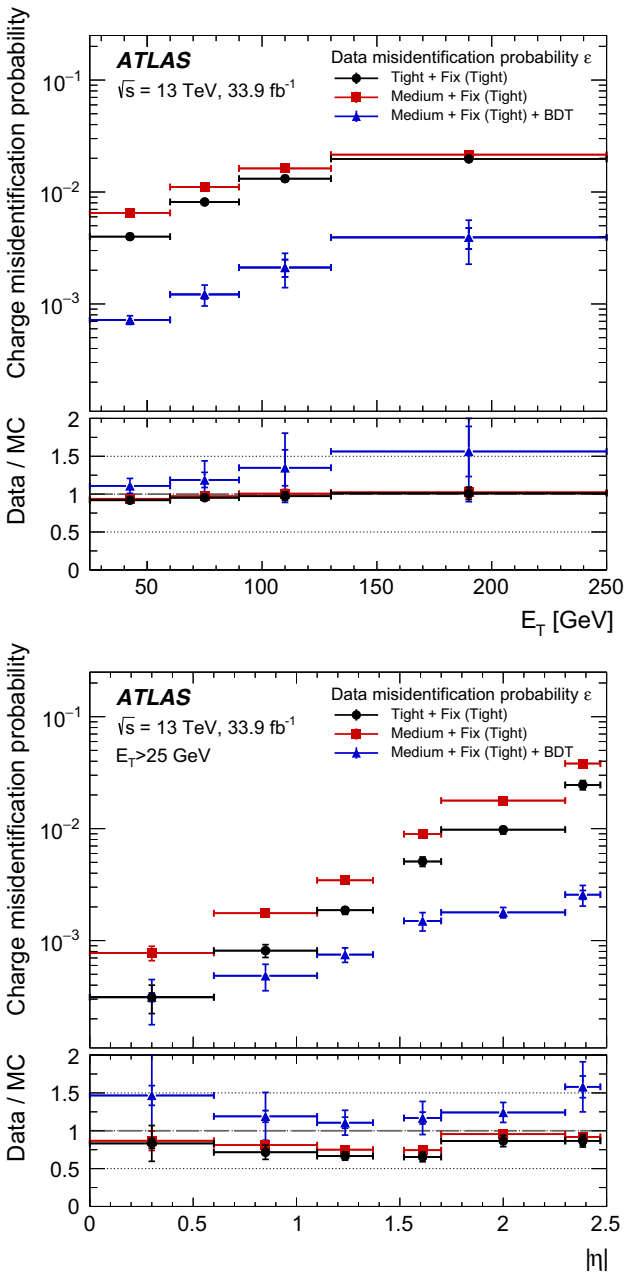

Fig. 15 Charge-misidentification rates in 2016 data and simulated $Z \to ee$ events as a function of E_{T} (top) and $|\eta|$ (bottom) showing the impact of applying the BDT requirement to suppress charge misidentification (red squares vs. blue triangles). Medium identification with BDT vs. Tight identification without BDT is also explored (black circles vs. blue triangles). The Fix (Tight) isolation requirement is applied in all cases (see Table 4). The inner uncertainties are statistical while the total uncertainties include both the statistical and systematic components

- Tight + Fix (Track $R_{\mathrm{max}} = 0.4$) used in cross-section measurements of gluon–gluon fusion and vector-boson-fusion Higgs-boson production in the $H \to WW^* \to e\nu\mu\nu$ decay channel [53].

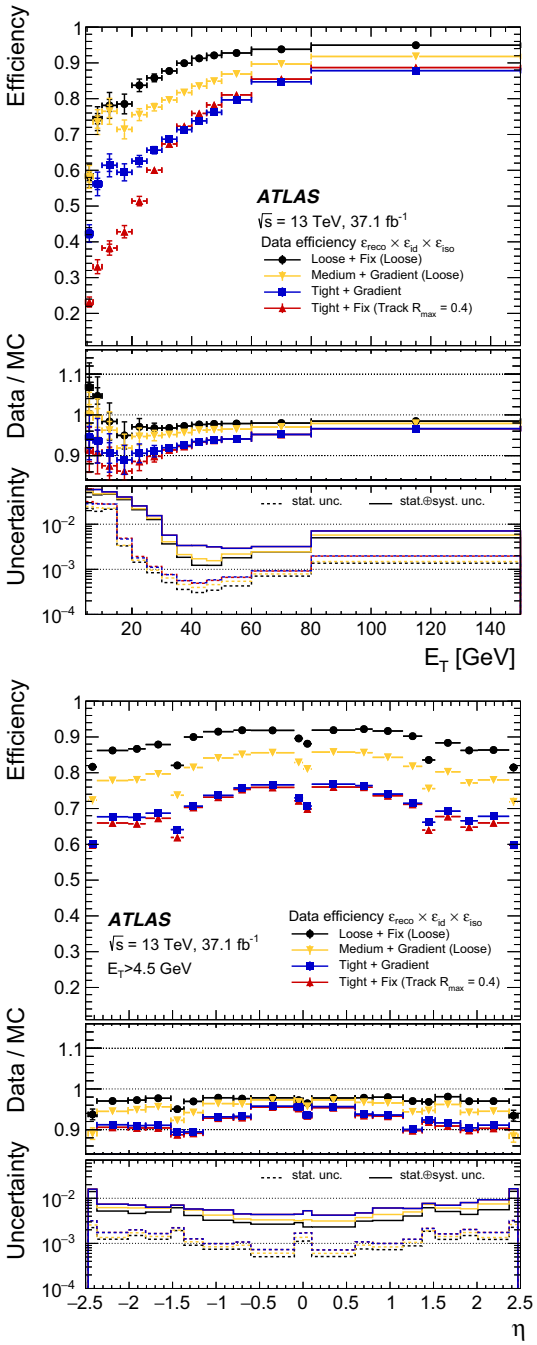

Fig. 16 The product of reconstruction, identification, and isolation efficiencies $\epsilon_{\mathrm{reco}} \times \epsilon_{\mathrm{id}} \times \epsilon_{\mathrm{iso}}$ for data from a $Z \to ee$ sample as a function of electron E_{T} (top) and η for $E_{\mathrm{T}} > 4.5$ GeV (bottom), for the following operating points: "Loose + Fix (Loose)" (black circles), "Medium + Gradient (Loose)" (yellow upside-down triangles), "Tight + Gradient" (blue squares) and "Tight + Fix" (Track $R_{\mathrm{max}} = 0.4$) (red triangles). The inner uncertainties are statistical while the total uncertainties include both the statistical and systematic components. The lower panels show data-to-simulation ratios as well as the relative statistical and total uncertainties (statistical and systematic added in quadrature) applicable to both the data efficiencies and correction factors

10 Conclusions

The focus of this paper is to document the methods used by the ATLAS experiment at the LHC in Run 2 to reconstruct, identify, and isolate prompt-electron candidates with high efficiency, as well as to suppress electron-charge misidentification. Efficiency measurements as evaluated with 37.1 fb^{-1} of 13 TeV pp collision data recorded in 2015–2016 are then compared with those determined from simulation.

The method used to reconstruct electron candidates is explained for candidates in the central region of the detector ($|\eta| < 2.47$). Illustrative measurements of the reconstruction efficiency are presented for candidates with transverse energy $E_{\mathrm{T}} > 4.5$ GeV. For $E_{\mathrm{T}} > 15$ GeV, the reconstruction efficiencies range from 96 to 99%, with the data uncertainties typically 1% for $E_{\mathrm{T}} = 15-20$ GeV and reaching the per-mille level at higher E_{T}.

The likelihood method used to identify electrons given the existence of a reconstructed electron candidate is also explained for candidates in the central region of the detector ($|\eta| < 2.47$). The minimum E_{T} of the identified electron is reduced from 7 GeV in Run 1 to 4.5 GeV in Run 2. Benchmark efficiency measurements for three identification operating points are provided: for the Tight operating point, the identification efficiency varies from 55% at $E_{\mathrm{T}} = 4.5$ GeV to 90% at $E_{\mathrm{T}} = 100$ GeV, while it ranges from 85% at $E_{\mathrm{T}} = 20$ GeV to 96% at $E_{\mathrm{T}} = 100$ GeV for the Loose operating point. The uncertainties in these measured efficiencies for the Loose (Tight) operating point range from 3% (4%) at $E_{\mathrm{T}} = 4.5$ GeV to 0.1% (0.3%) for $E_{\mathrm{T}} = 40$ GeV.

The ability to identify electron candidates isolated from any other local activity in the detector is documented. Two varieties of isolation variables, calorimeter- and tracking-based, are considered. Since the implementation of isolation criteria is specific to the physics analysis needs, several operating points are illustrated; their typical isolation efficiencies are measured in data and determined from simulation, ranging from approximately 90% for the tightest operating points to nearly 99% for the loosest, for electrons with $E_{\mathrm{T}} = 40$ GeV.

Possible sources of electron-charge misidentification are explored and an algorithm to suppress such effects is outlined. The efficiency for correct charge reconstruction is illustrated for candidates passing the Medium identification requirements. The efficiency is approximately 96% in both data and simulation and is mostly independent of E_{T}, while it varies from 90 to 99% over most of the electron η region except at very high $|\eta|$ where the efficiency in data is approximately 76%. The corresponding efficiency in simulation is about 8% higher, due to mismodelling.

Finally, since total efficiencies are used in ATLAS physics analyses, the product of the electron efficiencies $\epsilon_{\mathrm{reco}} \times \epsilon_{\mathrm{id}} \times \epsilon_{\mathrm{iso}}$ measured in data and presented in this paper for some typical operating points demonstrate the impact of these efficiencies on ATLAS measurements and searches for new physics.

Acknowledgements We thank CERN for the very successful operation of the LHC, as well as the support staff from our institutions without whom ATLAS could not be operated efficiently. We acknowledge the support of ANPCyT, Argentina; YerPhI, Armenia; ARC, Australia; BMWFW and FWF, Austria; ANAS, Azerbaijan; SSTC, Belarus; CNPq and FAPESP, Brazil; NSERC, NRC and CFI, Canada; CERN; CONICYT, Chile; CAS, MOST and NSFC, China; COLCIENCIAS, Colombia; MSMT CR, MPO CR and VSC CR, Czech Republic; DNRF and DNSRC, Denmark; IN2P3-CNRS, CEA-DRF/IRFU, France; SRNSFG, Georgia; BMBF, HGF, and MPG, Germany; GSRT, Greece; RGC, Hong Kong SAR, China; ISF and Benoziyo Center, Israel; INFN, Italy; MEXT and JSPS, Japan; CNRST, Morocco; NWO, The Netherlands; RCN, Norway; MNiSW and NCN, Poland; FCT, Portugal; MNE/IFA, Romania; MES of Russia and NRC KI, Russian Federation; JINR; MESTD, Serbia; MSSR, Slovakia; ARRS and MIZŠ, Slovenia; DST/NRF, South Africa; MINECO, Spain; SRC and Wallenberg Foundation, Sweden; SERI, SNSF and Cantons of Bern and Geneva, Switzerland; MOST, Taiwan; TAEK, Turkey; STFC, UK; DOE and NSF, USA. In addition, individual groups and members have received support from BCKDF, CANARIE, CRC and Compute Canada, Canada; COST, ERC, ERDF, Horizon 2020, and Marie Skłodowska-Curie Actions, European Union; Investissements d' Avenir Labex and Idex, ANR, France; DFG and AvH Foundation, Germany; Herakleitos, Thales and Aristeia programmes co-financed by EU-ESF and the Greek NSRF, Greece; BSF-NSF and GIF, Israel; CERCA Programme Generalitat de Catalunya, Spain; The Royal Society and Leverhulme Trust, UK. The crucial computing support from all WLCG partners is acknowledged gratefully, in particular from CERN, the ATLAS Tier-1 facilities at TRIUMF (Canada), NDGF (Denmark, Norway, Sweden), CC-IN2P3 (France), KIT/GridKA (Germany), INFN-CNAF (Italy), NL-T1 (The Netherlands), PIC (Spain), ASGC (Taiwan), RAL (UK) and BNL (USA), the Tier-2 facilities worldwide and large non-WLCG resource providers. Major contributors of computing resources are listed in Ref. [54].

Data Availability Statement This manuscript has no associated data or the data will not be deposited. [Authors' comment: All ATLAS scientific output is published in journals, and preliminary results are made available in Conference Notes. All are openly available, without restriction on use by external parties beyond copyright law and the standard conditions agreed by CERN. Data associated with journal publications are also made available: tables and data from plots (e.g. cross section values, likelihood profiles, selection efficiencies, cross section limits, ...) are stored in appropriate repositories such as HEPDATA (http://hepdata.cedar.ac.uk/). ATLAS also strives to make additional material related to the paper available that allows a reinterpretation of the data in the context of new theoretical models. For example, an extended encapsulation of the analysis is often provided for measurements in the framework of RIVET (http://rivet.hepforge.org/)." This information is taken from the ATLAS Data Access Policy, which is a public document that can be downloaded from http://opendata.cern.ch/record/413 [opendata.cern.ch].]

References

1. ATLAS Collaboration, Electron performance measurements with the ATLAS detector using the 2010 LHC proton–proton collision data, Eur. Phys. J. C **72**, 1909 (2012) arXiv:1110.3174 [hep-ex]
2. ATLAS Collaboration, Electron reconstruction and identification efficiency measurements with the ATLAS detector using the 2011 LHC proton–proton collision data, Eur. Phys. J. C **74**, 2941 (2014) arXiv:1404.2240 [hep-ex]
3. ATLAS Collaboration, Electron efficiency measurements with the ATLAS detector using 2012 LHC proton–proton collision data, Eur. Phys. J. C **77**, 195 (2017) arXiv:1612.01456 [hep-ex]
4. ATLAS Collaboration, Luminosity determination in pp collisions at $\sqrt{s} = 8$ TeV using the ATLAS detector at the LHC, Eur. Phys. J. C **76**, 653 (2016) arXiv:1608.03953 [hep-ex]
5. ATLAS Collaboration, The ATLAS Experiment at the CERN Large Hadron Collider, JINST **3**, S08003 (2008)
6. B. Abbott et al., Production and integration of the ATLAS Insertable B-Layer. JINST **13**, T05008 (2018). arXiv:1803.00844 [physics.ins-det]
7. ATLAS Collaboration, ATLAS Insertable B-Layer Technical Design Report, ATLAS-TDR-19, (2010), https://cds.cern.ch/record/1291633, ATLAS Insertable B-Layer Technical Design Report Addendum, ATLAS-TDR-19-ADD-1, (2012) https://cds.cern.ch/record/1451888
8. P. Nason, A new method for combining NLO QCD with shower Monte Carlo algorithms. JHEP **11**, 040 (2004). arXiv:hep-ph/0409146
9. S. Frixione, P. Nason, C. Oleari, Matching NLO QCD computations with parton shower simulations: the POWHEG method. JHEP **11**, 070 (2007). arXiv:0709.2092 [hep-ph]
10. S. Alioli, P. Nason, C. Oleari, E. Re, A general framework for implementing NLO calculations in shower Monte Carlo programs: the POWHEG BOX. JHEP **06**, 043 (2010). arXiv:1002.2581 [hep-ph]
11. S. Alioli, P. Nason, C. Oleari, E. Re, NLO vector-boson production matched with shower in POWHEG. JHEP **07**, 060 (2008). arXiv:0805.4802 [hep-ph]
12. S. Frixione, P. Nason, G. Ridolfi, A positive-weight next-to-leading-order Monte Carlo for heavy flavour hadroproduction. JHEP **09**, 126 (2007). arXiv:0707.3088 [hep-ph]
13. T. Sjöstrand, S. Mrenna, P.Z. Skands, A brief introduction to PYTHIA 8.1. Comput. Phys. Commun. **178**, 852 (2008). arXiv:0710.3820 [hep-ph]
14. H.-L. Lai et al., New parton distributions for collider physics. Phys. Rev. D **82**, 074024 (2010). arXiv:1007.2241 [hep-ph]
15. ATLAS Collaboration, Measurement of the Z/γ^* boson transverse momentum distribution in pp collisions at $\sqrt{s} = 7$ TeV with the ATLAS detector, JHEP **09**, 145 (2014). arXiv:1406.3660 [hep-ex]
16. J. Pumplin et al., New generation of parton distributions with uncertainties from global QCD analysis. JHEP **07**, 012 (2002). arXiv:hep-ph/0201195 [hep-ph]
17. ATLAS Collaboration, ATLAS Pythia 8 tunes to 7 TeV data, ATL-PHYS-PUB-2014-021 (2014). https://cdsweb.cern.ch/record/1966419
18. R.D. Ball et al., Parton distributions with LHC data. Nucl. Phys. B **867**, 244 (2013). arXiv:1207.1303 [hep-ph]
19. A.D. Martin, W.J. Stirling, R.S. Thorne, G. Watt, Parton distributions for the LHC. Eur. Phys. J. C **63**, 189 (2009). arXiv:0901.0002 [hep-ph]
20. S. Agostinelli et al., GEANT4–a simulation toolkit. Nucl. Instrum. Meth. A **506**, 250 (2003)
21. ATLAS Collaboration, The ATLAS Simulation Infrastructure, Eur. Phys. J. C **70**, 823 (2010). arXiv:1005.4568 [physics.ins-det]
22. ATLAS Collaboration, Performance of the ATLAS trigger system in 2015, Eur. Phys. J. C **77**, 317 (2017). arXiv:1611.09661 [hep-ex]
23. C. Blocker, Uncertainties on Efficiencies, CDF/MEMO/STATISTICS/PUBLIC/7168. http://www-cdf.fnal.gov/physics/statistics/notes/cdf7168_eff_uncertainties.ps
24. H1 Collaboration, Measurement of the inclusive ep scattering cross section at low Q^2 and x at HERA. Eur. Phys. J. C **63**, 625 (2009). arXiv:0904.0929 [hep-ex]
25. C. Patrignani et al., Review of particle physics. Chin. Phys. C **40**, 100001 (2016)
26. ATLAS Collaboration, Measurement of the diffierential cross-sections of inclusive, prompt and non-prompt J/ψ production in proton–proton collisions at $\sqrt{s} = 7$ TeV, Nucl. Phys. B **850**, 387 (2011). arXiv:1104.3038 [hep-ex]
27. W. Lampl et al., Calorimeter clustering algorithms: description and performance. ATL-LARG-PUB-2008-002 (2008). https://cds.cern.ch/record/1099735
28. ATLAS Collaboration, Performance of the ATLAS track reconstruction algorithms in dense environments in LHC Run 2, Eur. Phys. J. C **77**, 673 (2017). arXiv: 1704.07983 [hep-ex]
29. T. Cornelissen et al., The new ATLAS track reconstruction (NEWT). J. Phys. Conf. Ser. **119**, 032014 (2008)
30. T. Cornelissen et al., The global χ^2 track fitter in ATLAS. J. Phys. Conf. Ser. **119**, 032013 (2008)
31. ATLAS Collaboration, Improved electron reconstruction in ATLAS using the Gaussian Sum Filter-based model for bremsstrahlung, ATLAS-CONF-2012-047 (2012). https://cds.cern.ch/record/1449796
32. R. Frühwirth, A Gaussian-mixture approximation of the Bethe-Heitler model of electron energy loss by bremsstrahlung. Comp. Phys. Comm. **154**, 131 (2003). ISSN: 0010-4655
33. R. Frühwirth, Application of Kalman filtering to track and vertex fitting. Nucl. Instrum. Meth. A **262**, 444 (1987)
34. ATLAS Collaboration, Measurement of the photon identification efficiencies with the ATLAS detector using LHC Run 2 data collected in 2015 and 2016. Eur. Phys. J. C **79**, 205 (2019). https://doi.org/10.1140/epjc/s10052-019-6650-6
35. ATLAS Collaboration, Electron and photon energy calibration with the ATLAS detector using LHC Run 1 data. Eur. Phys. J. C **74**, 3071 (2014). arXiv:1407.5063 [hep-ex]
36. ATLAS Collaboration, Electron and photon energy calibration with the ATLAS detector using 2015–2016 LHC proton–proton collision data. JINST **14**, P03017 (2019). https://doi.org/10.1088/1748-0221/14/03/P03017
37. A. Hoecker et al., TMVA: Toolkit for Multivariate Data Analysis, PoS ACAT **040** (2007). arXiv:physics/0703039, http://tmva.sourceforge.net/
38. ATLAS Collaboration, Topological cell clustering in the ATLAS calorimeters and its performance in LHC Run 1. Eur. Phys. J. C **77**, 490 (2017). arXiv:1603.02934 [hep-ex]
39. M. Cacciari, G.P. Salam, Pileup subtraction using jet areas. Phys. Lett. B **659**, 119 (2008). arXiv:0707.1378 [hep-ph]
40. S.D. Ellis, D.E. Soper, Successive combination jet algorithm for hadron collisions. Phys. Rev. D **48**, 3160 (1993). arXiv:hep-ph/9305266 [hep-ph]
41. S. Catani, Y.L. Dokshitzer, M.H. Seymour, B.R. Webber, Longitudinally invariant K_t clustering algorithms for hadron hadron collisions. Nucl. Phys. B **406**, 187 (1993)
42. ATLAS Collaboration, Search for supersymmetry in final states with two same-sign or three leptons and jets using 36 fb^{-1} of $\sqrt{s} =$ 13 TeV pp collision data with the ATLAS detector. JHEP **09**, 084 (2017). arXiv:1706.03731 [hep-ex]
43. ATLAS Collaboration, Evidence for the associated production of the Higgs boson and a top quark pair with the ATLAS detector. Phys. Rev. D. **97**, 072003 (2018). arXiv: 1712.08891 [hep-ex]

44. ATLAS Collaboration, Observation of electroweak production of a same-sign W boson pair in association with two jets in pp collisions at $\sqrt{s} = 13$ TeV with the ATLAS detector. Eur. Phys. J. C **79** 535 (2019). https://doi.org/10.1140/epjc/s10052-019-7027-6
45. ATLAS Collaboration, Search for doubly charged Higgs boson production in multi-lepton final states with the ATLAS detector using proton–proton collisions at $\sqrt{s} = 13$ TeV. Eur. Phys. J. C **78**, 199 (2018). arXiv:1710.09748 [hep-ex]
46. ATLAS Collaboration, Measurement of inclusive and differential cross sections in the $H \to ZZ^* \to 4\ell$ decay channel in pp collisions at $\sqrt{s} = 13$ TeV with the ATLAS detector. JHEP **10**, 132(2017). arXiv:1708.02810 [hep-ex]
47. ATLAS Collaboration, $ZZ \to \ell^+\ell^-\ell'^+\ell'^-$ cross-section measurements and search for anomalous triple gauge couplings in 13 TeV pp collisions with the ATLAS detector. Phys. Rev. D **97**, 032005 (2018). arXiv:1709.07703 [hep-ex]
48. ATLAS Collaboration, Search for direct top squark pair production in final states with two leptons in $\sqrt{s} = 13$ TeV pp collisions with the ATLAS detector. Eur. Phys. J. C **77**, 898 (2017). arXiv:1708.03247 [hep-ex]
49. ATLAS Collaboration, Measurement of $W^{\pm}Z$ production cross sections and gauge boson polarisation in pp collisions at $\sqrt{s} = 13$ TeV with the ATLAS detector. Eur. Phys. J. C **79**, 535 (2019). https://doi.org/10.1140/epjc/s10052-019-7027-6
50. ATLAS Collaboration, Measurement of diffierential cross-sections of a single top quark produced in association with a W boson at $\sqrt{s} = 13$ TeV with ATLAS. Eur. Phys. J. C **78**, 186 (2018). arXiv:1712.01602 [hep-ex]
51. ATLAS Collaboration, Measurement of the production cross-section of a single top quark in association with a Z boson in proton–proton collisions at 13 TeV with the ATLAS detector. Phys. Lett. B **780**, 557 (2018). arXiv:1905.04242 [hep-ex]
52. ATLAS Collaboration, Measurement of fiducial and differential W^+W^- production cross-sections at $\sqrt{s}$ =13 TeV with the ATLAS detector (2019). arXiv:1905.04242 [hep-ex]
53. ATLAS Collaboration, Measurements of gluon-gluon fusion and vector-boson fusion Higgs bosonproduction cross-sections in the $H \to WW^* \to e\nu\mu\nu$ decay channel in pp collisions at $\sqrt{s} = 13$ TeV with the ATLAS detector (2018). arXiv:1808.09054 [hep-ex]
54. ATLAS Collaboration, ATLAS computing acknowledgements, ATL-GEN-PUB-2016-002. https://cds.cern.ch/record/2202407

ATLAS Collaboration

M. Aaboud[34d], G. Aad[99], B. Abbott[125], D. C. Abbott[100], O. Abdinov[13,*], B. Abeloos[129], D. K. Abhayasinghe[91], S. H. Abidi[164], O. S. AbouZeid[39], N. L. Abraham[153], H. Abramowicz[158], H. Abreu[157], Y. Abulaiti[6], B. S. Acharya[64a,64b,p], S. Adachi[160], L. Adam[97], L. Adamczyk[81a], L. Adamek[164], J. Adelman[119], M. Adersberger[112], A. Adiguzel[12c,ai], T. Adye[141], A. A. Affolder[143], Y. Afik[157], C. Agheorghiesei[27c], J. A. Aguilar-Saavedra[137a,137f,ah], F. Ahmadov[77,af], G. Aielli[71a,71b], S. Akatsuka[83], T. P. A. Åkesson[94], E. Akilli[52], A. V. Akimov[108], G. L. Alberghi[23a,23b], J. Albert[173], P. Albicocco[49], M. J. Alconada Verzini[86], S. Alderweireldt[117], M. Aleksa[35], I. N. Aleksandrov[77], C. Alexa[27b], D. Alexandre[19], T. Alexopoulos[10], M. Alhroob[125], B. Ali[139], G. Alimonti[66a], J. Alison[36], S. P. Alkire[145], C. Allaire[129], B. M. M. Allbrooke[153], B. W. Allen[128], P. P. Allport[21], A. Aloisio[67a,67b], A. Alonso[39], F. Alonso[86], C. Alpigiani[145], A. A. Alshehri[55], M. I. Alstaty[99], B. Alvarez Gonzalez[35], D. Álvarez Piqueras[171], M. G. Alviggi[67a,67b], B. T. Amadio[18], Y. Amaral Coutinho[78b], A. Ambler[101], L. Ambroz[132], C. Amelung[26], D. Amidei[103], S. P. Amor Dos Santos[137a,137c], S. Amoroso[44], C. S. Amrouche[52], F. An[76], C. Anastopoulos[146], L. S. Ancu[52], N. Andari[142], T. Andeen[11], C. F. Anders[59b], J. K. Anders[20], K. J. Anderson[36], A. Andreazza[66a,66b], V. Andrei[59a], C. R. Anelli[173], S. Angelidakis[37], I. Angelozzi[118], A. Angerami[38], A. V. Anisenkov[120a,120b], A. Annovi[69a], C. Antel[59a], M. T. Anthony[146], M. Antonelli[49], D. J. A. Antrim[168], F. Anulli[70a], M. Aoki[79], J. A. Aparisi Pozo[171], L. Aperio Bella[35], G. Arabidze[104], J. P. Araque[137a], V. Araujo Ferraz[78b], R. Araujo Pereira[78b], A. T. H. Arce[47], R. E. Ardell[91], F. A. Arduh[86], J-F. Arguin[107], S. Argyropoulos[75], J.-H. Arling[44], A. J. Armbruster[35], L. J. Armitage[90], A. Armstrong[168], O. Arnaez[164], H. Arnold[118], M. Arratia[31], O. Arslan[24], A. Artamonov[109,*], G. Artoni[132], S. Artz[97], S. Asai[160], N. Asbah[57], E. M. Asimakopoulou[169], L. Asquith[153], K. Assamagan[29], R. Astalos[28a], R. J. Atkin[32a], M. Atkinson[170], N. B. Atlay[148], K. Augsten[139], G. Avolio[35], R. Avramidou[58a], M. K. Ayoub[15a], A. M. Azoulay[165b], G. Azuelos[107,av], A. E. Baas[59a], M. J. Baca[21], H. Bachacou[142], K. Bachas[65a,65b], M. Backes[132], P. Bagnaia[70a,70b], M. Bahmani[82], H. Bahrasemani[149], A. J. Bailey[171], V. R. Bailey[170], J. T. Baines[141], M. Bajic[39], C. Bakalis[10], O. K. Baker[180], P. J. Bakker[118], D. Bakshi Gupta[8], S. Balaji[154], E. M. Baldin[120a,120b], P. Balek[177], F. Balli[142], W. K. Balunas[134], J. Balz[97], E. Banas[82], A. Bandyopadhyay[24], S. Banerjee[178,l], A. A. E. Bannoura[179], L. Barak[158], W. M. Barbe[37], E. L. Barberio[102], D. Barberis[53a,53b], M. Barbero[99], T. Barillari[113], M-S. Barisits[35], J. Barkeloo[128], T. Barklow[150], R. Barnea[157], S. L. Barnes[58c], B. M. Barnett[141], R. M. Barnett[18], Z. Barnovska-Blenessy[58a], A. Baroncelli[72a], G. Barone[29], A. J. Barr[132], L. Barranco Navarro[171], F. Barreiro[96], J. Barreiro Guimarães da Costa[15a], R. Bartoldus[150], A. E. Barton[87], P. Bartos[28a], A. Basalaev[135], A. Bassalat[129], R. L. Bates[55], S. J. Batista[164], S. Batlamous[34e], J. R. Batley[31], M. Battaglia[143], M. Bauce[70a,70b], F. Bauer[142], K. T. Bauer[168], H. S. Bawa[150], J. B. Beacham[123], T. Beau[133], P. H. Beauchemin[167], P. Bechtle[24], H. C. Beck[51], H. P. Beck[20,s], K. Becker[50], M. Becker[97], C. Becot[44], A. Beddall[12d], A. J. Beddall[12a], V. A. Bednyakov[77], M. Bedognetti[118], C. P. Bee[152], T. A. Beermann[74], M. Begalli[78b], M. Begel[29], A. Behera[152], J. K. Behr[44], F. Beisiegel[24], A. S. Bell[92], G. Bella[158], L. Bellagamba[23b], A. Bellerive[33], M. Bellomo[157], P. Bellos[9], K. Belotskiy[110], N. L. Belyaev[110], O. Benary[158,*], D. Benchekroun[34a], M. Bender[112], N. Benekos[10], Y. Benhammou[158], E. Benhar Noccioli[180], J. Benitez[75],

D. P. Benjamin[6], M. Benoit[52], J. R. Bensinger[26], S. Bentvelsen[118], L. Beresford[132], M. Beretta[49], D. Berge[44], E. Bergeaas Kuutmann[169], N. Berger[5], B. Bergmann[139], L. J. Bergsten[26], J. Beringer[18], S. Berlendis[7], N. R. Bernard[100], G. Bernardi[133], C. Bernius[150], F. U. Bernlochner[24], T. Berry[91], P. Berta[97], C. Bertella[15a], G. Bertoli[43a,43b], I. A. Bertram[87], G. J. Besjes[39], O. Bessidskaia Bylund[179], M. Bessner[44], N. Besson[142], A. Bethani[98], S. Bethke[113], A. Betti[24], A. J. Bevan[90], J. Beyer[113], R. Bi[136], R. M. Bianchi[136], O. Biebel[112], D. Biedermann[19], R. Bielski[35], K. Bierwagen[97], N. V. Biesuz[69a,69b], M. Biglietti[72a], T. R. V. Billoud[107], M. Bindi[51], A. Bingul[12d], C. Bini[70a,70b], S. Biondi[23a,23b], M. Birman[177], T. Bisanz[51], J. P. Biswal[158], C. Bittrich[46], D. M. Bjergaard[47], J. E. Black[150], K. M. Black[25], T. Blazek[28a], I. Bloch[44], C. Blocker[26], A. Blue[55], U. Blumenschein[90], Dr. Blunier[144a], G. J. Bobbink[118], V. S. Bobrovnikov[120a,120b], S. S. Bocchetta[94], A. Bocci[47], D. Boerner[179], D. Bogavac[112], A. G. Bogdanchikov[120a,120b], C. Bohm[43a], V. Boisvert[91], P. Bokan[169], T. Bold[81a], A. S. Boldyrev[111], A. E. Bolz[59b], M. Bomben[133], M. Bona[90], J. S. Bonilla[128], M. Boonekamp[142], H. M. Borecka-Bielska[88], A. Borisov[121], G. Borissov[87], J. Bortfeldt[35], D. Bortoletto[132], V. Bortolotto[71a,71b], D. Boscherini[23b], M. Bosman[14], J. D. Bossio Sola[30], K. Bouaouda[34a], J. Boudreau[136], E. V. Bouhova-Thacker[87], D. Boumediene[37], C. Bourdarios[129], S. K. Boutle[55], A. Boveia[123], J. Boyd[35], D. Boye[32b], I. R. Boyko[77], A. J. Bozson[91], J. Bracinik[21], N. Brahimi[99], A. Brandt[8], G. Brandt[179], O. Brandt[59a], F. Braren[44], U. Bratzler[161], B. Brau[100], J. E. Brau[128], W. D. Breaden Madden[55], K. Brendlinger[44], L. Brenner[44], R. Brenner[169], S. Bressler[177], B. Brickwedde[97], D. L. Briglin[21], D. Britton[55], D. Britzger[113], I. Brock[24], R. Brock[104], G. Brooijmans[38], T. Brooks[91], W. K. Brooks[144b], E. Brost[119], J. H. Broughton[21], P. A. Bruckman de Renstrom[82], D. Bruncko[28b], A. Bruni[23b], G. Bruni[23b], L. S. Bruni[118], S. Bruno[71a,71b], B. H. Brunt[31], M. Bruschi[23b], N. Bruscino[136], P. Bryant[36], L. Bryngemark[94], T. Buanes[17], Q. Buat[35], P. Buchholz[148], A. G. Buckley[55], I. A. Budagov[77], M. K. Bugge[131], F. Bührer[50], O. Bulekov[110], D. Bullock[8], T. J. Burch[119], S. Burdin[88], C. D. Burgard[118], A. M. Burger[5], B. Burghgrave[119], K. Burka[82], S. Burke[141], I. Burmeister[45], J. T. P. Burr[132], V. Büscher[97], E. Buschmann[51], P. Bussey[55], J. M. Butler[25], C. M. Buttar[55], J. M. Butterworth[92], P. Butti[35], W. Buttinger[35], A. Buzatu[155], A. R. Buzykaev[120a,120b], G. Cabras[23a,23b], S. Cabrera Urbán[171], D. Caforio[139], H. Cai[170], V. M. M. Cairo[2], O. Cakir[4a], N. Calace[35], P. Calafiura[18], A. Calandri[99], G. Calderini[133], P. Calfayan[63], G. Callea[55], L. P. Caloba[78b], S. Calvente Lopez[96], D. Calvet[37], S. Calvet[37], T. P. Calvet[152], M. Calvetti[69a,69b], R. Camacho Toro[133], S. Camarda[35], D. Camarero Munoz[96], P. Camarri[71a,71b], D. Cameron[131], R. Caminal Armadans[100], C. Camincher[35], S. Campana[35], M. Campanelli[92], A. Camplani[39], A. Campoverde[148], V. Canale[67a,67b], M. Cano Bret[58c], J. Cantero[126], T. Cao[158], Y. Cao[170], M. D. M. Capeans Garrido[35], I. Caprini[27b], M. Caprini[27b], M. Capua[40b,40a], R. M. Carbone[38], R. Cardarelli[71a], F. C. Cardillo[146], I. Carli[140], T. Carli[35], G. Carlino[67a], B. T. Carlson[136], L. Carminati[66a,66b], R. M. D. Carney[43a,43b], S. Caron[117], E. Carquin[144b], S. Carrá[66a,66b], J. W. S. Carter[164], D. Casadei[32b], M. P. Casado[14,g], A. F. Casha[164], D. W. Casper[168], R. Castelijn[118], F. L. Castillo[171], V. Castillo Gimenez[171], N. F. Castro[137a,137e], A. Catinaccio[35], J. R. Catmore[131], A. Cattai[35], J. Caudron[24], V. Cavaliere[29], E. Cavallaro[14], D. Cavalli[66a], M. Cavalli-Sforza[14], V. Cavasinni[69a,69b], E. Celebi[12b], F. Ceradini[72a,72b], L. Cerda Alberich[171], A. S. Cerqueira[78a], A. Cerri[153], L. Cerrito[71a,71b], F. Cerutti[18], A. Cervelli[23a,23b], S. A. Cetin[12b], A. Chafaq[34a], D. Chakraborty[119], S. K. Chan[57], W. S. Chan[118], J. D. Chapman[31], B. Chargeishvili[156b], D. G. Charlton[21], C. C. Chau[33], C. A. Chavez Barajas[153], S. Che[123], A. Chegwidden[104], S. Chekanov[6], S. V. Chekulaev[165a], G. A. Chelkov[77,au], M. A. Chelstowska[35], B. Chen[76], C. Chen[58a], C. H. Chen[76], H. Chen[29], J. Chen[58a], J. Chen[38], S. Chen[134], S. J. Chen[15c], X. Chen[15b,at], Y. Chen[80], Y-H. Chen[44], H. C. Cheng[61a], H. J. Cheng[15d], A. Cheplakov[77], E. Cheremushkina[121], R. Cherkaoui El Moursli[34e], E. Cheu[7], K. Cheung[62], T. J. A. Chevalérias[142], L. Chevalier[142], V. Chiarella[49], G. Chiarelli[69a], G. Chiodini[65a], A. S. Chisholm[35,21], A. Chitan[27b], I. Chiu[160], Y. H. Chiu[173], M. V. Chizhov[77], K. Choi[63], A. R. Chomont[129], S. Chouridou[159], Y. S. Chow[118], V. Christodoulou[92], M. C. Chu[61a], J. Chudoba[138], A. J. Chuinard[101], J. J. Chwastowski[82], L. Chytka[127], D. Cinca[45], V. Cindro[89], I. A. Cioară[24], A. Ciocio[18], F. Cirotto[67a,67b], Z. H. Citron[177], M. Citterio[66a], A. Clark[52], M. R. Clark[38], P. J. Clark[48], C. Clement[43a,43b], Y. Coadou[99], M. Cobal[64a,64c], A. Coccaro[53a,53b], J. Cochran[76], H. Cohen[158], A. E. C. Coimbra[177], L. Colasurdo[117], B. Cole[38], A. P. Colijn[118], J. Collot[56], P. Conde Muiño[137a,i], E. Coniavitis[50], S. H. Connell[32b], I. A. Connelly[98], S. Constantinescu[27b], F. Conventi[67a,aw], A. M. Cooper-Sarkar[132], F. Cormier[172], K. J. R. Cormier[164], L. D. Corpe[92], M. Corradi[70a,70b], E. E. Corrigan[94], F. Corriveau[101,ad], A. Cortes-Gonzalez[35], M. J. Costa[171], F. Costanza[5], D. Costanzo[146], G. Cottin[31], G. Cowan[91], B. E. Cox[98], J. Crane[98], K. Cranmer[122], S. J. Crawley[55], R. A. Creager[134], G. Cree[33], S. Crépé-Renaudin[56], F. Crescioli[133], M. Cristinziani[24], V. Croft[122], G. Crosetti[40b,40a], A. Cueto[96], T. Cuhadar Donszelmann[146], A. R. Cukierman[150], S. Czekierda[82], P. Czodrowski[35], M. J. Da Cunha Sargedas De Sousa[58b], C. Da Via[98], W. Dabrowski[81a], T. Dado[28a,y], S. Dahbi[34e], T. Dai[103], F. Dallaire[107], C. Dallapiccola[100], M. Dam[39], G. D'amen[23a,23b], J. Damp[97], J. R. Dandoy[134], M. F. Daneri[30], N. P. Dang[178,l], N. D. Dann[98], M. Danninger[172], V. Dao[35], G. Darbo[53b], S. Darmora[8], O. Dartsi[5], A. Dattagupta[128], T. Daubney[44], S. D'Auria[66a,66b], W. Davey[24], C. David[44], T. Davidek[140], D. R. Davis[47], E. Dawe[102], I. Dawson[146], K. De[8], R. De Asmundis[67a], A. De Benedetti[125], M. De Beurs[118], S. De Castro[23a,23b], S. De Cecco[70a,70b], N. De Groot[117],

P. de Jong[118], H. De la Torre[104], F. De Lorenzi[76], A. De Maria[69a,69b], D. De Pedis[70a], A. De Salvo[70a], U. De Sanctis[71a,71b], M. De Santis[71a,71b], A. De Santo[153], K. De Vasconcelos Corga[99], J. B. De Vivie De Regie[129], C. Debenedetti[143], D. V. Dedovich[77], N. Dehghanian[3], M. Del Gaudio[40b,40a], J. Del Peso[96], Y. Delabat Diaz[44], D. Delgove[129], F. Deliot[142], C. M. Delitzsch[7], M. Della Pietra[67a,67b], D. Della Volpe[52], A. Dell'Acqua[35], L. Dell'Asta[25], M. Delmastro[5], C. Delporte[129], P. A. Delsart[56], D. A. DeMarco[164], S. Demers[180], M. Demichev[77], S. P. Denisov[121], D. Denysiuk[118], L. D'Eramo[133], D. Derendarz[82], J. E. Derkaoui[34d], F. Derue[133], P. Dervan[88], K. Desch[24], C. Deterre[44], K. Dette[164], M. R. Devesa[30], P. O. Deviveiros[35], A. Dewhurst[141], S. Dhaliwal[26], F. A. Di Bello[52], A. Di Ciaccio[71a,71b], L. Di Ciaccio[5], W. K. Di Clemente[134], C. Di Donato[67a,67b], A. Di Girolamo[35], G. Di Gregorio[69a,69b], B. Di Micco[72a,72b], R. Di Nardo[100], K. F. Di Petrillo[57], R. Di Sipio[164], D. Di Valentino[33], C. Diaconu[99], M. Diamond[164], F. A. Dias[39], T. Dias Do Vale[137a], M. A. Diaz[144a], J. Dickinson[18], E. B. Diehl[103], J. Dietrich[19], S. Díez Cornell[44], A. Dimitrievska[18], J. Dingfelder[24], F. Dittus[35], F. Djama[99], T. Djobava[156b], J. I. Djuvsland[59a], M. A. B. Do Vale[78c], M. Dobre[27b], D. Dodsworth[26], C. Doglioni[94], J. Dolejsi[140], Z. Dolezal[140], M. Donadelli[78d], J. Donini[37], A. D'onofrio[90], M. D'Onofrio[88], J. Dopke[141], A. Doria[67a], M. T. Dova[86], A. T. Doyle[55], E. Drechsler[149], E. Dreyer[149], T. Dreyer[51], Y. Du[58b], F. Dubinin[108], M. Dubovsky[28a], A. Dubreuil[52], E. Duchovni[177], G. Duckeck[112], A. Ducourthial[133], O. A. Ducu[107,x], D. Duda[113], A. Dudarev[35], A. C. Dudder[97], E. M. Duffield[18], L. Duflot[129], M. Dührssen[35], C. Dülsen[179], M. Dumancic[177], A. E. Dumitriu[27b,e], A. K. Duncan[55], M. Dunford[59a], A. Duperrin[99], H. Duran Yildiz[4a], M. Düren[54], A. Durglishvili[156b], D. Duschinger[46], B. Dutta[44], D. Duvnjak[1], M. Dyndal[44], S. Dysch[98], B. S. Dziedzic[82], K. M. Ecker[113], R. C. Edgar[103], T. Eifert[35], G. Eigen[17], K. Einsweiler[18], T. Ekelof[169], M. El Kacimi[34c], R. El Kosseifi[99], V. Ellajosyula[99], M. Ellert[169], F. Ellinghaus[179], A. A. Elliot[90], N. Ellis[35], J. Elmsheuser[29], M. Elsing[35], D. Emeliyanov[141], A. Emerman[38], Y. Enari[160], J. S. Ennis[175], M. B. Epland[47], J. Erdmann[45], A. Ereditato[20], S. Errede[170], M. Escalier[129], C. Escobar[171], O. Estrada Pastor[171], A. I. Etienvre[142], E. Etzion[158], H. Evans[63], A. Ezhilov[135], M. Ezzi[34e], F. Fabbri[55], L. Fabbri[23a,23b], V. Fabiani[117], G. Facini[92], R. M. Faisca Rodrigues Pereira[137a], R. M. Fakhrutdinov[121], S. Falciano[70a], P. J. Falke[5], S. Falke[5], J. Faltova[140], Y. Fang[15a], M. Fanti[66a,66b], A. Farbin[8], A. Farilla[72a], E. M. Farina[68a,68b], T. Farooque[104], S. Farrell[18], S. M. Farrington[175], P. Farthouat[35], F. Fassi[34e], P. Fassnacht[35], D. Fassouliotis[9], M. Faucci Giannelli[48], A. Favareto[53a,53b], W. J. Fawcett[31], L. Fayard[129], O. L. Fedin[135,q], W. Fedorko[172], M. Feickert[41], S. Feigl[131], L. Feligioni[99], C. Feng[58b], E. J. Feng[35], M. Feng[47], M. J. Fenton[55], A. B. Fenyuk[121], L. Feremenga[8], J. Ferrando[44], A. Ferrari[169], P. Ferrari[118], R. Ferrari[68a], D. E. Ferreira de Lima[59b], A. Ferrer[171], D. Ferrere[52], C. Ferretti[103], F. Fiedler[97], A. Filipčič[89], F. Filthaut[117], K. D. Finelli[25], M. C. N. Fiolhais[137a,137c,a], L. Fiorini[171], C. Fischer[14], W. C. Fisher[104], N. Flaschel[44], I. Fleck[148], P. Fleischmann[103], R. R. M. Fletcher[134], T. Flick[179], B. M. Flierl[112], L. M. Flores[134], L. R. Flores Castillo[61a], F. M. Follega[73a,73b], N. Fomin[17], G. T. Forcolin[73a,73b], A. Formica[142], F. A. Förster[14], A. C. Forti[98], A. G. Foster[21], D. Fournier[129], H. Fox[87], S. Fracchia[146], P. Francavilla[69a,69b], M. Franchini[23a,23b], S. Franchino[59a], D. Francis[35], L. Franconi[143], M. Franklin[57], M. Frate[168], M. Fraternali[68a,68b], A. N. Fray[90], D. Freeborn[92], B. Freund[107], W. S. Freund[78b], E. M. Freundlich[45], D. C. Frizzell[125], D. Froidevaux[35], J. A. Frost[132], C. Fukunaga[161], E. Fullana Torregrosa[171], T. Fusayasu[114], J. Fuster[171], O. Gabizon[157], A. Gabrielli[23a,23b], A. Gabrielli[18], G. P. Gach[81a], S. Gadatsch[52], P. Gadow[113], G. Gagliardi[53a,53b], L. G. Gagnon[107], C. Galea[27b], B. Galhardo[137a,137c], E. J. Gallas[132], B. J. Gallop[141], P. Gallus[139], G. Galster[39], R. Gamboa Goni[90], K. K. Gan[123], S. Ganguly[177], J. Gao[58a], Y. Gao[88], Y. S. Gao[150,n], C. García[171], J. E. García Navarro[171], J. A. García Pascual[15a], M. Garcia-Sciveres[18], R. W. Gardner[36], N. Garelli[150], S. Gargiulo[50], V. Garonne[131], K. Gasnikova[44], A. Gaudiello[53a,53b], G. Gaudio[68a], I. L. Gavrilenko[108], A. Gavrilyuk[109], C. Gay[172], G. Gaycken[24], E. N. Gazis[10], C. N. P. Gee[141], J. Geisen[51], M. Geisen[97], M. P. Geisler[59a], C. Gemme[53b], M. H. Genest[56], C. Geng[103], S. Gentile[70a,70b], S. George[91], D. Gerbaudo[14], G. Gessner[45], S. Ghasemi[148], M. Ghasemi Bostanabad[173], M. Ghneimat[24], B. Giacobbe[23b], S. Giagu[70a,70b], N. Giangiacomi[23a,23b], P. Giannetti[69a], A. Giannini[67a,67b], S. M. Gibson[91], M. Gignac[143], D. Gillberg[33], G. Gilles[179], D. M. Gingrich[3,av], M. P. Giordani[64a,64c], F. M. Giorgi[23b], P. F. Giraud[142], P. Giromini[57], G. Giugliarelli[64a,64c], D. Giugni[66a], F. Giuli[132], M. Giulini[59b], S. Gkaitatzis[159], I. Gkialas[9,k], E. L. Gkougkousis[14], P. Gkountoumis[10], L. K. Gladilin[111], C. Glasman[96], J. Glatzer[14], P. C. F. Glaysher[44], A. Glazov[44], M. Goblirsch-Kolb[26], J. Godlewski[82], S. Goldfarb[102], T. Golling[52], D. Golubkov[121], A. Gomes[137a,137b], R. Goncalves Gama[51], R. Gonçalo[137a], G. Gonella[50], L. Gonella[21], A. Gongadze[77], F. Gonnella[21], J. L. Gonski[57], S. González de la Hoz[171], S. Gonzalez-Sevilla[52], L. Goossens[35], P. A. Gorbounov[109], H. A. Gordon[29], B. Gorini[35], E. Gorini[65a,65b], A. Gorišek[89], A. T. Goshaw[47], C. Gössling[45], M. I. Gostkin[77], C. A. Gottardo[24], C. R. Goudet[129], D. Goujdami[34c], A. G. Goussiou[145], N. Govender[32b,c], C. Goy[5], E. Gozani[157], I. Grabowska-Bold[81a], P. O. J. Gradin[169], E. C. Graham[88], J. Gramling[168], E. Gramstad[131], S. Grancagnolo[19], V. Gratchev[135], P. M. Gravila[27f], F. G. Gravili[65a,65b], C. Gray[55], H. M. Gray[18], Z. D. Greenwood[93,al], C. Grefe[24], K. Gregersen[94], I. M. Gregor[44], P. Grenier[150], K. Grevtsov[44], N. A. Grieser[125], J. Griffiths[8], A. A. Grillo[143], K. Grimm[150,b], S. Grinstein[14,z], Ph. Gris[37], J.-F. Grivaz[129], S. Groh[97], E. Gross[177], J. Grosse-Knetter[51], G. C. Grossi[93], Z. J. Grout[92], C. Grud[103],

A. Grummer[116], L. Guan[103], W. Guan[178], J. Guenther[35], A. Guerguichon[129], F. Guescini[165a], D. Guest[168], R. Gugel[50], B. Gui[123], T. Guillemin[5], S. Guindon[35], U. Gul[55], J. Guo[58c], W. Guo[103], Y. Guo[58a,t], Z. Guo[99], R. Gupta[44], S. Gurbuz[12c], G. Gustavino[125], P. Gutierrez[125], C. Gutschow[92], C. Guyot[142], M. P. Guzik[81a], C. Gwenlan[132], C. B. Gwilliam[88], A. Haas[122], C. Haber[18], H. K. Hadavand[8], N. Haddad[34e], A. Hadef[58a], S. Hageböck[24], M. Hagihara[166], H. Hakobyan[181,*], M. Haleem[174], J. Haley[126], G. Halladjian[104], G. D. Hallewell[99], K. Hamacher[179], P. Hamal[127], K. Hamano[173], A. Hamilton[32a], G. N. Hamity[146], K. Han[58a,ak], L. Han[58a], S. Han[15d], K. Hanagaki[79,v], M. Hance[143], D. M. Handl[112], B. Haney[134], R. Hankache[133], P. Hanke[59a], E. Hansen[94], J. B. Hansen[39], J. D. Hansen[39], M. C. Hansen[24], P. H. Hansen[39], K. Hara[166], A. S. Hard[178], T. Harenberg[179], S. Harkusha[105], P. F. Harrison[175], N. M. Hartmann[112], Y. Hasegawa[147], A. Hasib[48], S. Hassani[142], S. Haug[20], R. Hauser[104], L. Hauswald[46], L. B. Havener[38], M. Havranek[139], C. M. Hawkes[21], R. J. Hawkings[35], D. Hayden[104], C. Hayes[152], C. P. Hays[132], J. M. Hays[90], H. S. Hayward[88], S. J. Haywood[141], F. He[58a], M. P. Heath[48], V. Hedberg[94], L. Heelan[8], S. Heer[24], K. K. Heidegger[50], J. Heilman[33], S. Heim[44], T. Heim[18], B. Heinemann[44,aq], J. J. Heinrich[112], L. Heinrich[122], C. Heinz[54], J. Hejbal[138], L. Helary[35], A. Held[172], S. Hellesund[131], C. M. Helling[143], S. Hellman[43a,43b], C. Helsens[35], R. C. W. Henderson[87], Y. Heng[178], S. Henkelmann[172], A. M. Henriques Correia[35], G. H. Herbert[19], H. Herde[26], V. Herget[174], Y. Hernández Jiménez[32c], H. Herr[97], M. G. Herrmann[112], T. Herrmann[46], G. Herten[50], R. Hertenberger[112], L. Hervas[35], T. C. Herwig[134], G. G. Hesketh[92], N. P. Hessey[165a], A. Higashida[160], S. Higashino[79], E. Higón-Rodriguez[171], K. Hildebrand[36], E. Hill[173], J. C. Hill[31], K. K. Hill[29], K. H. Hiller[44], S. J. Hillier[21], M. Hils[46], I. Hinchliffe[18], F. Hinterkeuser[24], M. Hirose[130], D. Hirschbuehl[179], B. Hiti[89], O. Hladik[138], D. R. Hlaluku[32c], X. Hoad[48], J. Hobbs[152], N. Hod[165a], M. C. Hodgkinson[146], A. Hoecker[35], M. R. Hoeferkamp[116], F. Hoenig[112], D. Hohn[50], D. Hohov[129], T. R. Holmes[36], M. Holzbock[112], M. Homann[45], B. H. Hommels[31], S. Honda[166], T. Honda[79], T. M. Hong[136], A. Hönle[113], B. H. Hooberman[170], W. H. Hopkins[128], Y. Horii[115], P. Horn[46], A. J. Horton[149], L. A. Horyn[36], J-Y. Hostachy[56], A. Hostiuc[145], S. Hou[155], A. Hoummada[34a], J. Howarth[98], J. Hoya[86], M. Hrabovsky[127], I. Hristova[19], J. Hrivnac[129], A. Hrynevich[106], T. Hryn'ova[5], P. J. Hsu[62], S.-C. Hsu[145], Q. Hu[29], S. Hu[58c], Y. Huang[15a], Z. Hubacek[139], F. Hubaut[99], M. Huebner[24], F. Huegging[24], T. B. Huffman[132], M. Huhtinen[35], R. F. H. Hunter[33], P. Huo[152], A. M. Hupe[33], N. Huseynov[77,af], J. Huston[104], J. Huth[57], R. Hyneman[103], G. Iacobucci[52], G. Iakovidis[29], I. Ibragimov[148], L. Iconomidou-Fayard[129], Z. Idrissi[34e], P. Iengo[35], R. Ignazzi[39], O. Igonkina[118,ab], R. Iguchi[160], T. Iizawa[52], Y. Ikegami[79], M. Ikeno[79], D. Iliadis[159], N. Ilic[117], F. Iltzsche[46], G. Introzzi[68a,68b], M. Iodice[72a], K. Iordanidou[38], V. Ippolito[70a,70b], M. F. Isacson[169], N. Ishijima[130], M. Ishino[160], M. Ishitsuka[162], W. Islam[126], C. Issever[132], S. Istin[157], F. Ito[166], J. M. Iturbe Ponce[61a], R. Iuppa[73a,73b], A. Ivina[177], H. Iwasaki[79], J. M. Izen[42], V. Izzo[67a], P. Jacka[138], P. Jackson[1], R. M. Jacobs[24], V. Jain[2], G. Jäkel[179], K. B. Jakobi[97], K. Jakobs[50], S. Jakobsen[74], T. Jakoubek[138], D. O. Jamin[126], R. Jansky[52], J. Janssen[24], M. Janus[51], P. A. Janus[81a], G. Jarlskog[94], N. Javadov[77,af], T. Javůrek[35], M. Javurkova[50], F. Jeanneau[142], L. Jeanty[18], J. Jejelava[156a,ag], A. Jelinskas[175], P. Jenni[50,d], J. Jeong[44], N. Jeong[44], S. Jézéquel[5], H. Ji[178], J. Jia[152], H. Jiang[76], Y. Jiang[58a], Z. Jiang[150,r], S. Jiggins[50], F. A. Jimenez Morales[37], J. Jimenez Pena[171], S. Jin[15c], A. Jinaru[27b], O. Jinnouchi[162], H. Jivan[32c], P. Johansson[146], K. A. Johns[7], C. A. Johnson[63], K. Jon-And[43a,43b], R. W. L. Jones[87], S. D. Jones[153], S. Jones[7], T. J. Jones[88], J. Jongmanns[59a], P. M. Jorge[137a,137b], J. Jovicevic[165a], X. Ju[18], J. J. Junggeburth[113], A. Juste Rozas[14,z], A. Kaczmarska[82], M. Kado[129], H. Kagan[123], M. Kagan[150], T. Kaji[176], E. Kajomovitz[157], C. W. Kalderon[94], A. Kaluza[97], S. Kama[41], A. Kamenshchikov[121], L. Kanjir[89], Y. Kano[160], V. A. Kantserov[110], J. Kanzaki[79], L. S. Kaplan[178], D. Kar[32c], M. J. Kareem[165b], E. Karentzos[10], S. N. Karpov[77], Z. M. Karpova[77], V. Kartvelishvili[87], A. N. Karyukhin[121], L. Kashif[178], R. D. Kass[123], A. Kastanas[43a,43b], Y. Kataoka[160], C. Kato[58d,58c], J. Katzy[44], K. Kawade[80], K. Kawagoe[85], T. Kawaguchi[115], T. Kawamoto[160], G. Kawamura[51], E. F. Kay[88], V. F. Kazanin[120a,120b], R. Keeler[173], R. Kehoe[41], J. S. Keller[33], E. Kellermann[94], J. J. Kempster[21], J. Kendrick[21], O. Kepka[138], S. Kersten[179], B. P. Kerševan[89], S. Ketabchi Haghighat[164], R. A. Keyes[101], M. Khader[170], F. Khalil-Zada[13], A. Khanov[126], A. G. Kharlamov[120a,120b], T. Kharlamova[120a,120b], E. E. Khoda[172], A. Khodinov[163], T. J. Khoo[52], E. Khramov[77], J. Khubua[156b], S. Kido[80], M. Kiehn[52], C. R. Kilby[91], Y. K. Kim[36], N. Kimura[64a,64c], O. M. Kind[19], B. T. King[88], D. Kirchmeier[46], J. Kirk[141], A. E. Kiryunin[113], T. Kishimoto[160], D. Kisielewska[81a], V. Kitali[44], O. Kivernyk[5], E. Kladiva[28b,*], T. Klapdor-Kleingrothaus[50], M. H. Klein[103], M. Klein[88], U. Klein[88], K. Kleinknecht[97], P. Klimek[119], A. Klimentov[29], T. Klingl[24], T. Klioutchnikova[35], F. F. Klitzner[112], P. Kluit[118], S. Kluth[113], E. Kneringer[74], E. B. F. G. Knoops[99], A. Knue[50], A. Kobayashi[160], D. Kobayashi[85], T. Kobayashi[160], M. Kobel[46], M. Kocian[150], P. Kodys[140], P. T. Koenig[24], T. Koffas[33], E. Koffeman[118], N. M. Köhler[113], T. Koi[150], M. Kolb[59b], I. Koletsou[5], T. Kondo[79], N. Kondrashova[58c], K. Köneke[50], A. C. König[117], T. Kono[79], R. Konoplich[122,an], V. Konstantinides[92], N. Konstantinidis[92], B. Konya[94], R. Kopeliansky[63], S. Koperny[81a], K. Korcyl[82], K. Kordas[159], G. Koren[158], A. Korn[92], I. Korolkov[14], E. V. Korolkova[146], N. Korotkova[111], O. Kortner[113], S. Kortner[113], T. Kosek[140], V. V. Kostyukhin[24], A. Kotwal[47], A. Koulouris[10], A. Kourkoumeli-Charalampidi[68a,68b], C. Kourkoumelis[9], E. Kourlitis[146], V. Kouskoura[29], A. B. Kowalewska[82], R. Kowalewski[173], T. Z. Kowalski[81a], C. Kozakai[160], W. Kozanecki[142], A. S. Kozhin[121],

V. A. Kramarenko[111], G. Kramberger[89], D. Krasnopevtsev[58a], M. W. Krasny[133], A. Krasznahorkay[35], D. Krauss[113], J. A. Kremer[81a], J. Kretzschmar[88], P. Krieger[164], K. Krizka[18], K. Kroeninger[45], H. Kroha[113], J. Kroll[138], J. Kroll[134], J. Krstic[16], U. Kruchonak[77], H. Krüger[24], N. Krumnack[76], M. C. Kruse[47], T. Kubota[102], S. Kuday[4b], J. T. Kuechler[179], S. Kuehn[35], A. Kugel[59a], T. Kuhl[44], V. Kukhtin[77], R. Kukla[99], Y. Kulchitsky[105,aj], S. Kuleshov[144b], Y. P. Kulinich[170], M. Kuna[56], T. Kunigo[83], A. Kupco[138], T. Kupfer[45], O. Kuprash[158], H. Kurashige[80], L. L. Kurchaninov[165a], Y. A. Kurochkin[105], A. Kurova[110], M. G. Kurth[15d], E. S. Kuwertz[35], M. Kuze[162], J. Kvita[127], T. Kwan[101], A. La Rosa[113], J. L. La Rosa Navarro[78d], L. La Rotonda[40b,40a], F. La Ruffa[40b,40a], C. Lacasta[171], F. Lacava[70a,70b], J. Lacey[44], D. P. J. Lack[98], H. Lacker[19], D. Lacour[133], E. Ladygin[77], R. Lafaye[5], B. Laforge[133], T. Lagouri[32c], S. Lai[51], S. Lammers[63], W. Lampl[7], E. Lançon[29], U. Landgraf[50], M. P. J. Landon[90], M. C. Lanfermann[52], V. S. Lang[44], J. C. Lange[51], R. J. Langenberg[35], A. J. Lankford[168], F. Lanni[29], K. Lantzsch[24], A. Lanza[68a], A. Lapertosa[53a,53b], S. Laplace[133], J. F. Laporte[142], T. Lari[66a], F. Lasagni Manghi[23a,23b], M. Lassnig[35], T. S. Lau[61a], A. Laudrain[129], M. Lavorgna[67a,67b], M. Lazzaroni[66a,66b], B. Le[102], O. Le Dortz[133], E. Le Guirriec[99], E. P. Le Quilleuc[142], M. LeBlanc[7], T. LeCompte[6], F. Ledroit-Guillon[56], C. A. Lee[29], G. R. Lee[144a], L. Lee[57], S. C. Lee[155], B. Lefebvre[101], M. Lefebvre[173], F. Legger[112], C. Leggett[18], K. Lehmann[149], N. Lehmann[179], G. Lehmann Miotto[35], W. A. Leight[44], A. Leisos[159,w], M. A. L. Leite[78d], R. Leitner[140], D. Lellouch[177], K. J. C. Leney[92], T. Lenz[24], B. Lenzi[35], R. Leone[7], S. Leone[69a], C. Leonidopoulos[48], G. Lerner[153], C. Leroy[107], R. Les[164], A. A. J. Lesage[142], C. G. Lester[31], M. Levchenko[135], J. Levêque[5], D. Levin[103], L. J. Levinson[177], D. Lewis[90], B. Li[15b], B. Li[103], C-Q. Li[58a,am], H. Li[58a], H. Li[58b], L. Li[58c], M. Li[15a], Q. Li[15d], Q. Y. Li[58a], S. Li[58d,58c], X. Li[58c], Y. Li[148], Z. Liang[15a], B. Liberti[71a], A. Liblong[164], K. Lie[61c], S. Liem[118], A. Limosani[154], C. Y. Lin[31], K. Lin[104], T. H. Lin[97], R. A. Linck[63], J. H. Lindon[21], B. E. Lindquist[152], A. L. Lionti[52], E. Lipeles[134], A. Lipniacka[17], M. Lisovyi[59b], T. M. Liss[170,as], A. Lister[172], A. M. Litke[143], J. D. Little[8], B. Liu[76], B. L. Liu[6], H. B. Liu[29], H. Liu[103], J. B. Liu[58a], J. K. K. Liu[132], K. Liu[133], M. Liu[58a], P. Liu[18], Y. Liu[15a], Y. L. Liu[58a], Y. W. Liu[58a], M. Livan[68a,68b], A. Lleres[56], J. Llorente Merino[15a], S. L. Lloyd[90], C. Y. Lo[61b], F. Lo Sterzo[41], E. M. Lobodzinska[44], P. Loch[7], T. Lohse[19], K. Lohwasser[146], M. Lokajicek[138], J. D. Long[170], R. E. Long[87], L. Longo[65a,65b], K. A. Looper[123], J. A. Lopez[144b], I. Lopez Paz[98], A. Lopez Solis[146], J. Lorenz[112], N. Lorenzo Martinez[5], M. Losada[22], P. J. Lösel[112], A. Lösle[50], X. Lou[44], X. Lou[15a], A. Lounis[129], J. Love[6], P. A. Love[87], J. J. Lozano Bahilo[171], H. Lu[61a], M. Lu[58a], Y. J. Lu[62], H. J. Lubatti[145], C. Luci[70a,70b], A. Lucotte[56], C. Luedtke[50], F. Luehring[63], I. Luise[133], L. Luminari[70a], B. Lund-Jensen[151], M. S. Lutz[100], P. M. Luzi[133], D. Lynn[29], R. Lysak[138], E. Lytken[94], F. Lyu[15a], V. Lyubushkin[77], T. Lyubushkina[77], H. Ma[29], L. L. Ma[58b], Y. Ma[58b], G. Maccarrone[49], A. Macchiolo[113], C. M. Macdonald[146], J. Machado Miguens[134,137b], D. Madaffari[171], R. Madar[37], W. F. Mader[46], N. Madysa[46], J. Maeda[80], K. Maekawa[160], S. Maeland[17], T. Maeno[29], M. Maerker[46], A. S. Maevskiy[111], V. Magerl[50], D. J. Mahon[38], C. Maidantchik[78b], T. Maier[112], A. Maio[137a,137b,137d], O. Majersky[28a], S. Majewski[128], Y. Makida[79], N. Makovec[129], B. Malaescu[133], Pa. Malecki[82], V. P. Maleev[135], F. Malek[56], U. Mallik[75], D. Malon[6], C. Malone[31], S. Maltezos[10], S. Malyukov[35], J. Mamuzic[171], G. Mancini[49], I. Mandić[89], J. Maneira[137a], L. Manhaes de Andrade Filho[78a], J. Manjarres Ramos[46], K. H. Mankinen[94], A. Mann[112], A. Manousos[74], B. Mansoulie[142], S. Manzoni[66a,66b], A. Marantis[159], G. Marceca[30], L. March[52], L. Marchese[132], G. Marchiori[133], M. Marcisovsky[138], C. Marcon[94], C. A. Marin Tobon[35], M. Marjanovic[37], F. Marroquim[78b], Z. Marshall[18], M.U.F Martensson[169], S. Marti-Garcia[171], C. B. Martin[123], T. A. Martin[175], V. J. Martin[48], B. Martin dit Latour[17], M. Martinez[14,z], V. I. Martinez Outschoorn[100], S. Martin-Haugh[141], V. S. Martoiu[27b], A. C. Martyniuk[92], A. Marzin[35], L. Masetti[97], T. Mashimo[160], R. Mashinistov[108], J. Masik[98], A. L. Maslennikov[120a,120b], L. H. Mason[102], L. Massa[71a,71b], P. Massarotti[67a,67b], P. Mastrandrea[152], A. Mastroberardino[40b,40a], T. Masubuchi[160], P. Mättig[24], J. Maurer[27b], B. Maček[89], S. J. Maxfield[88], D. A. Maximov[120a,120b], R. Mazini[155], I. Maznas[159], S. M. Mazza[143], S. P. Mc Kee[103], A. McCarn[41], T. G. McCarthy[113], L. I. McClymont[92], W. P. McCormack[18], E. F. McDonald[102], J. A. Mcfayden[35], G. Mchedlidze[51], M. A. McKay[41], K. D. McLean[173], S. J. McMahon[141], P. C. McNamara[102], C. J. McNicol[175], R. A. McPherson[173,ad], J. E. Mdhluli[32c], Z. A. Meadows[100], S. Meehan[145], T. M. Megy[50], S. Mehlhase[112], A. Mehta[88], T. Meideck[56], B. Meirose[42], D. Melini[171,h], B. R. Mellado Garcia[32c], J. D. Mellenthin[51], M. Melo[28a], F. Meloni[44], A. Melzer[24], S. B. Menary[98], E. D. Mendes Gouveia[137a], L. Meng[88], X. T. Meng[103], S. Menke[113], E. Meoni[40b,40a], S. Mergelmeyer[19], S. A. M. Merkt[136], C. Merlassino[20], P. Mermod[52], L. Merola[67a,67b], C. Meroni[66a], F. S. Merritt[36], A. Messina[70a,70b], J. Metcalfe[6], A. S. Mete[168], C. Meyer[63], J. Meyer[157], J-P. Meyer[142], H. Meyer Zu Theenhausen[59a], F. Miano[153], R. P. Middleton[141], L. Mijović[48], G. Mikenberg[177], M. Mikestikova[138], M. Mikuž[89], M. Milesi[102], A. Milic[164], D. A. Millar[90], D. W. Miller[36], A. Milov[177], D. A. Milstead[43a,43b], R. A. Mina[150,r], A. A. Minaenko[121], M. Miñano Moya[171], I. A. Minashvili[156b], A. I. Mincer[122], B. Mindur[81a], M. Mineev[77], Y. Minegishi[160], Y. Ming[178], L. M. Mir[14], A. Mirto[65a,65b], K. P. Mistry[134], T. Mitani[176], J. Mitrevski[112], V. A. Mitsou[171], M. Mittal[58c], A. Miucci[20], P. S. Miyagawa[146], A. Mizukami[79], J. U. Mjörnmark[94], T. Mkrtchyan[181], M. Mlynarikova[140], T. Moa[43a,43b], K. Mochizuki[107], P. Mogg[50], S. Mohapatra[38], S. Molander[43a,43b], R. Moles-Valls[24], M. C. Mondragon[104], K. Mönig[44], J. Monk[39], E. Monnier[99], A. Montalbano[149],

J. Montejo Berlingen[35], F. Monticelli[86], S. Monzani[66a], N. Morange[129], D. Moreno[22], M. Moreno Llácer[35], P. Morettini[53b], M. Morgenstern[118], S. Morgenstern[46], D. Mori[149], M. Morii[57], M. Morinaga[176], V. Morisbak[131], A. K. Morley[35], G. Mornacchi[35], A. P. Morris[92], J. D. Morris[90], L. Morvaj[152], P. Moschovakos[10], M. Mosidze[156b], H. J. Moss[146], J. Moss[150,o], K. Motohashi[162], R. Mount[150], E. Mountricha[35], E. J. W. Moyse[100], S. Muanza[99], F. Mueller[113], J. Mueller[136], R. S. P. Mueller[112], D. Muenstermann[87], G. A. Mullier[94], F. J. Munoz Sanchez[98], P. Murin[28b], W. J. Murray[175,141], A. Murrone[66a,66b], M. Muškinja[89], C. Mwewa[32a], A. G. Myagkov[121,ao], J. Myers[128], M. Myska[139], B. P. Nachman[18], O. Nackenhorst[45], K. Nagai[132], K. Nagano[79], Y. Nagasaka[60], M. Nagel[50], E. Nagy[99], A. M. Nairz[35], Y. Nakahama[115], K. Nakamura[79], T. Nakamura[160], I. Nakano[124], H. Nanjo[130], F. Napolitano[59a], R. F. Naranjo Garcia[44], R. Narayan[11], D. I. Narrias Villar[59a], I. Naryshkin[135], T. Naumann[44], G. Navarro[22], R. Nayyar[7], H. A. Neal[103,*], P. Y. Nechaeva[108], T. J. Neep[142], A. Negri[68a,68b], M. Negrini[23b], S. Nektarijevic[117], C. Nellist[51], M. E. Nelson[132], S. Nemecek[138], P. Nemethy[122], M. Nessi[35,f], M. S. Neubauer[170], M. Neumann[179], P. R. Newman[21], T. Y. Ng[61c], Y. S. Ng[19], Y. W. Y. Ng[168], H. D. N. Nguyen[99], T. Nguyen Manh[107], E. Nibigira[37], R. B. Nickerson[132], R. Nicolaidou[142], D. S. Nielsen[39], J. Nielsen[143], N. Nikiforou[11], V. Nikolaenko[121,ao], I. Nikolic-Audit[133], K. Nikolopoulos[21], P. Nilsson[29], H. R. Nindhito[52], Y. Ninomiya[79], A. Nisati[70a], N. Nishu[58c], R. Nisius[113], I. Nitsche[45], T. Nitta[176], T. Nobe[160], Y. Noguchi[83], M. Nomachi[130], I. Nomidis[133], M. A. Nomura[29], T. Nooney[90], M. Nordberg[35], N. Norjoharuddeen[132], T. Novak[89], O. Novgorodova[46], R. Novotny[139], L. Nozka[127], K. Ntekas[168], E. Nurse[92], F. Nuti[102], F. G. Oakham[33,av], H. Oberlack[113], J. Ocariz[133], A. Ochi[80], I. Ochoa[38], J. P. Ochoa-Ricoux[144a], K. O'Connor[26], S. Oda[85], S. Odaka[79], S. Oerdek[51], A. Oh[98], S. H. Oh[47], C. C. Ohm[151], H. Oide[53a,53b], M. L. Ojeda[164], H. Okawa[166], Y. Okazaki[83], Y. Okumura[160], T. Okuyama[79], A. Olariu[27b], L. F. Oleiro Seabra[137a], S. A. Olivares Pino[144a], D. Oliveira Damazio[29], J. L. Oliver[1], M. J. R. Olsson[36], A. Olszewski[82], J. Olszowska[82], D. C. O'Neil[149], A. Onofre[137a,137e], K. Onogi[115], P. U. E. Onyisi[11], H. Oppen[131], M. J. Oreglia[36], G. E. Orellana[86], Y. Oren[158], D. Orestano[72a,72b], E. C. Orgill[98], N. Orlando[61b], A. A. O'Rourke[44], R. S. Orr[164], B. Osculati[53a,53b,*], V. O'Shea[55], R. Ospanov[58a], G. Otero y Garzon[30], H. Otono[85], M. Ouchrif[34d], F. Ould-Saada[131], A. Ouraou[142], Q. Ouyang[15a], M. Owen[55], R. E. Owen[21], V. E. Ozcan[12c], N. Ozturk[8], J. Pacalt[127], H. A. Pacey[31], K. Pachal[149], A. Pacheco Pages[14], L. Pacheco Rodriguez[142], C. Padilla Aranda[14], S. Pagan Griso[18], M. Paganini[180], G. Palacino[63], S. Palazzo[48], S. Palestini[35], M. Palka[81b], D. Pallin[37], I. Panagoulias[10], C. E. Pandini[35], J. G. Panduro Vazquez[91], P. Pani[35], G. Panizzo[64a,64c], L. Paolozzi[52], T. D. Papadopoulou[10], K. Papageorgiou[9,k], A. Paramonov[6], D. Paredes Hernandez[61b], S. R. Paredes Saenz[132], B. Parida[163], T. H. Park[33], A. J. Parker[87], K. A. Parker[44], M. A. Parker[31], F. Parodi[53a,53b], J. A. Parsons[38], U. Parzefall[50], V. R. Pascuzzi[164], J. M. P. Pasner[143], E. Pasqualucci[70a], S. Passaggio[53b], F. Pastore[91], P. Pasuwan[43a,43b], S. Pataraia[97], J. R. Pater[98], A. Pathak[178,l], T. Pauly[35], B. Pearson[113], M. Pedersen[131], L. Pedraza Diaz[117], R. Pedro[137a,137b], S. V. Peleganchuk[120a,120b], O. Penc[138], C. Peng[15d], H. Peng[58a], B. S. Peralva[78a], M. M. Perego[129], A. P. Pereira Peixoto[137a], D. V. Perepelitsa[29], F. Peri[19], L. Perini[66a,66b], H. Pernegger[35], S. Perrella[67a,67b], V. D. Peshekhonov[77,*], K. Peters[44], R. F. Y. Peters[98], B. A. Petersen[35], T. C. Petersen[39], E. Petit[56], A. Petridis[1], C. Petridou[159], P. Petroff[129], M. Petrov[132], F. Petrucci[72a,72b], M. Pettee[180], N. E. Pettersson[100], A. Peyaud[142], R. Pezoa[144b], T. Pham[102], F. H. Phillips[104], P. W. Phillips[141], M. W. Phipps[170], G. Piacquadio[152], E. Pianori[18], A. Picazio[100], R. H. Pickles[98], R. Piegaia[30], J. E. Pilcher[36], A. D. Pilkington[98], M. Pinamonti[71a,71b], J. L. Pinfold[3], M. Pitt[177], L. Pizzimento[71a,71b], M.-A. Pleier[29], V. Pleskot[140], E. Plotnikova[77], D. Pluth[76], P. Podberezko[120a,120b], R. Poettgen[94], R. Poggi[52], L. Poggioli[129], I. Pogrebnyak[104], D. Pohl[24], I. Pokharel[51], G. Polesello[68a], A. Poley[18], A. Policicchio[70a,70b], R. Polifka[35], A. Polini[23b], C. S. Pollard[44], V. Polychronakos[29], D. Ponomarenko[110], L. Pontecorvo[35], G. A. Popeneciu[27d], D. M. Portillo Quintero[133], S. Pospisil[139], K. Potamianos[44], I. N. Potrap[77], C. J. Potter[31], H. Potti[11], T. Poulsen[94], J. Poveda[35], T. D. Powell[146], M. E. Pozo Astigarraga[35], P. Pralavorio[99], S. Prell[76], D. Price[98], M. Primavera[65a], S. Prince[101], M. L. Proffitt[145], N. Proklova[110], K. Prokofiev[61c], F. Prokoshin[144b], S. Protopopescu[29], J. Proudfoot[6], M. Przybycien[81a], A. Puri[170], P. Puzo[129], J. Qian[103], Y. Qin[98], A. Quadt[51], M. Queitsch-Maitland[44], A. Qureshi[1], P. Rados[102], F. Ragusa[66a,66b], G. Rahal[95], J. A. Raine[52], S. Rajagopalan[29], A. Ramirez Morales[90], K. Ran[15a], T. Rashid[129], S. Raspopov[5], M. G. Ratti[66a,66b], D. M. Rauch[44], F. Rauscher[112], S. Rave[97], B. Ravina[146], I. Ravinovich[177], J. H. Rawling[98], M. Raymond[35], A. L. Read[131], N. P. Readioff[56], M. Reale[65a,65b], D. M. Rebuzzi[68a,68b], A. Redelbach[174], G. Redlinger[29], R. Reece[143], R. G. Reed[32c], K. Reeves[42], L. Rehnisch[19], J. Reichert[134], D. Reikher[158], A. Reiss[97], A. Rej[148], C. Rembser[35], H. Ren[15d], M. Rescigno[70a], S. Resconi[66a], E. D. Resseguie[134], S. Rettie[172], E. Reynolds[21], O. L. Rezanova[120a,120b], P. Reznicek[140], E. Ricci[73a,73b], R. Richter[113], S. Richter[44], E. Richter-Was[81b], O. Ricken[24], M. Ridel[133], P. Rieck[113], C. J. Riegel[179], O. Rifki[44], M. Rijssenbeek[152], A. Rimoldi[68a,68b], M. Rimoldi[20], L. Rinaldi[23b], G. Ripellino[151], B. Ristić[87], E. Ritsch[35], I. Riu[14], J. C. Rivera Vergara[144a], F. Rizatdinova[126], E. Rizvi[90], C. Rizzi[14], R. T. Roberts[98], S. H. Robertson[101,ad], D. Robinson[31], J. E. M. Robinson[44], A. Robson[55], E. Rocco[97], C. Roda[69a,69b], Y. Rodina[99], S. Rodriguez Bosca[171], A. Rodriguez Perez[14], D. Rodriguez Rodriguez[171], A. M. Rodríguez Vera[165b], S. Roe[35], C. S. Rogan[57], O. Røhne[131], R. Röhrig[113], C. P. A. Roland[63], J. Roloff[57], A. Romaniouk[110], M. Romano[23a,23b],

N. Rompotis[88], M. Ronzani[122], L. Roos[133], S. Rosati[70a], K. Rosbach[50], N-A. Rosien[51], B. J. Rosser[134], E. Rossi[44], E. Rossi[72a,72b], E. Rossi[67a,67b], L. P. Rossi[53b], L. Rossini[66a,66b], J. H. N. Rosten[31], R. Rosten[14], M. Rotaru[27b], J. Rothberg[145], D. Rousseau[129], D. Roy[32c], A. Rozanov[99], Y. Rozen[157], X. Ruan[32c], F. Rubbo[150], F. Rühr[50], A. Ruiz-Martinez[171], Z. Rurikova[50], N. A. Rusakovich[77], H. L. Russell[101], J. P. Rutherfoord[7], E. M. Rüttinger[44,m], Y. F. Ryabov[135], M. Rybar[38], G. Rybkin[129], S. Ryu[6], A. Ryzhov[121], G. F. Rzehorz[51], P. Sabatini[51], G. Sabato[118], S. Sacerdoti[129], H.F-W. Sadrozinski[143], R. Sadykov[77], F. Safai Tehrani[70a], P. Saha[119], M. Sahinsoy[59a], A. Sahu[179], M. Saimpert[44], M. Saito[160], T. Saito[160], H. Sakamoto[160], A. Sakharov[122,an], D. Salamani[52], G. Salamanna[72a,72b], J. E. Salazar Loyola[144b], P. H. Sales De Bruin[169], D. Salihagic[113], A. Salnikov[150], J. Salt[171], D. Salvatore[40b,40a], F. Salvatore[153], A. Salvucci[61a,61b,61c], A. Salzburger[35], J. Samarati[35], D. Sammel[50], D. Sampsonidis[159], D. Sampsonidou[159], J. Sánchez[171], A. Sanchez Pineda[64a,64c], H. Sandaker[131], C. O. Sander[44], M. Sandhoff[179], C. Sandoval[22], D. P. C. Sankey[141], M. Sannino[53a,53b], Y. Sano[115], A. Sansoni[49], C. Santoni[37], H. Santos[137a], I. Santoyo Castillo[153], A. Santra[171], A. Sapronov[77], J. G. Saraiva[137a,137d], O. Sasaki[79], K. Sato[166], E. Sauvan[5], P. Savard[164,av], N. Savic[113], R. Sawada[160], C. Sawyer[141], L. Sawyer[93,al], C. Sbarra[23b], A. Sbrizzi[23a], T. Scanlon[92], J. Schaarschmidt[145], P. Schacht[113], B. M. Schachtner[112], D. Schaefer[36], L. Schaefer[134], J. Schaeffer[97], S. Schaepe[35], U. Schäfer[97], A. C. Schaffer[129], D. Schaile[112], R. D. Schamberger[152], N. Scharmberg[98], V. A. Schegelsky[135], D. Scheirich[140], F. Schenck[19], M. Schernau[168], C. Schiavi[53a,53b], S. Schier[143], L. K. Schildgen[24], Z. M. Schillaci[26], E. J. Schioppa[35], M. Schioppa[40b,40a], K. E. Schleicher[50], S. Schlenker[35], K. R. Schmidt-Sommerfeld[113], K. Schmieden[35], C. Schmitt[97], S. Schmitt[44], S. Schmitz[97], J. C. Schmoeckel[44], U. Schnoor[50], L. Schoeffel[142], A. Schoening[59b], E. Schopf[132], M. Schott[97], J. F. P. Schouwenberg[117], J. Schovancova[35], S. Schramm[52], A. Schulte[97], H-C. Schultz-Coulon[59a], M. Schumacher[50], B. A. Schumm[143], Ph. Schune[142], A. Schwartzman[150], T. A. Schwarz[103], Ph. Schwemling[142], R. Schwienhorst[104], A. Sciandra[24], G. Sciolla[26], M. Scornajenghi[40b,40a], F. Scuri[69a], F. Scutti[102], L. M. Scyboz[113], C. D. Sebastiani[70a,70b], P. Seema[19], S. C. Seidel[116], A. Seiden[143], T. Seiss[36], J. M. Seixas[78b], G. Sekhniaidze[67a], K. Sekhon[103], S. J. Sekula[41], N. Semprini-Cesari[23a,23b], S. Sen[47], S. Senkin[37], C. Serfon[131], L. Serin[129], L. Serkin[64a,64b], M. Sessa[58a], H. Severini[125], F. Sforza[167], A. Sfyrla[52], E. Shabalina[51], J. D. Shahinian[143], N. W. Shaikh[43a,43b], D. Shaked Renous[177], L. Y. Shan[15a], R. Shang[170], J. T. Shank[25], M. Shapiro[18], A. S. Sharma[1], A. Sharma[132], P. B. Shatalov[109], K. Shaw[153], S. M. Shaw[98], A. Shcherbakova[135], Y. Shen[125], N. Sherafati[33], A. D. Sherman[25], P. Sherwood[92], L. Shi[155,ar], S. Shimizu[79], C. O. Shimmin[180], Y. Shimogama[176], M. Shimojima[114], I. P. J. Shipsey[132], S. Shirabe[85], M. Shiyakova[77], J. Shlomi[177], A. Shmeleva[108], D. Shoaleh Saadi[107], M. J. Shochet[36], S. Shojaii[102], D. R. Shope[125], S. Shrestha[123], E. Shulga[110], P. Sicho[138], A. M. Sickles[170], P. E. Sidebo[151], E. Sideras Haddad[32c], O. Sidiropoulou[35], A. Sidoti[23a,23b], F. Siegert[46], Dj. Sijacki[16], J. Silva[137a], M. Silva Jr.[178], M. V. Silva Oliveira[78a], S. B. Silverstein[43a], S. Simion[129], E. Simioni[97], M. Simon[97], R. Simoniello[97], P. Sinervo[164], N. B. Sinev[128], M. Sioli[23a,23b], I. Siral[103], S. Yu. Sivoklokov[111], J. Sjölin[43a,43b], P. Skubic[125], M. Slater[21], T. Slavicek[139], M. Slawinska[82], K. Sliwa[167], R. Slovak[140], V. Smakhtin[177], B. H. Smart[5], J. Smiesko[28a], N. Smirnov[110], S. Yu. Smirnov[110], Y. Smirnov[110], L. N. Smirnova[111], O. Smirnova[94], J. W. Smith[51], M. Smizanska[87], K. Smolek[139], A. Smykiewicz[82], A. A. Snesarev[108], I. M. Snyder[128], S. Snyder[29], R. Sobie[173,ad], A. M. Soffa[168], A. Soffer[158], A. Søgaard[48], F. Sohns[51], G. Sokhrannyi[89], C. A. Solans Sanchez[35], M. Solar[139], E. Yu. Soldatov[110], U. Soldevila[171], A. A. Solodkov[121], A. Soloshenko[77], O. V. Solovyanov[121], V. Solovyev[135], P. Sommer[146], H. Son[167], W. Song[141], W. Y. Song[165b], A. Sopczak[139], F. Sopkova[28b], C. L. Sotiropoulou[69a,69b], S. Sottocornola[68a,68b], R. Soualah[64a,64c,j], A. M. Soukharev[120a,120b], D. South[44], S. Spagnolo[65a,65b], M. Spalla[113], M. Spangenberg[175], F. Spanò[91], D. Sperlich[19], T. M. Spieker[59a], R. Spighi[23b], G. Spigo[35], L. A. Spiller[102], D. P. Spiteri[55], M. Spousta[140], A. Stabile[66a,66b], R. Stamen[59a], S. Stamm[19], E. Stanecka[82], R. W. Stanek[6], C. Stanescu[72a], B. Stanislaus[132], M. M. Stanitzki[44], B. Stapf[118], S. Stapnes[131], E. A. Starchenko[121], G. H. Stark[143], J. Stark[56], S. H. Stark[39], P. Staroba[138], P. Starovoitov[59a], S. Stärz[101], R. Staszewski[82], M. Stegler[44], P. Steinberg[29], B. Stelzer[149], H. J. Stelzer[35], O. Stelzer-Chilton[165a], H. Stenzel[54], T. J. Stevenson[90], G. A. Stewart[35], M. C. Stockton[35], G. Stoicea[27b], P. Stolte[51], S. Stonjek[113], A. Straessner[46], J. Strandberg[151], S. Strandberg[43a,43b], M. Strauss[125], P. Strizenec[28b], R. Ströhmer[174], D. M. Strom[128], R. Stroynowski[41], A. Strubig[48], S. A. Stucci[29], B. Stugu[17], J. Stupak[125], N. A. Styles[44], D. Su[150], J. Su[136], S. Suchek[59a], Y. Sugaya[130], M. Suk[139], V. V. Sulin[108], M. J. Sullivan[88], D. M. S. Sultan[52], S. Sultansoy[4c], T. Sumida[83], S. Sun[103], X. Sun[3], K. Suruliz[153], C. J. E. Suster[154], M. R. Sutton[153], S. Suzuki[79], M. Svatos[138], M. Swiatlowski[36], S. P. Swift[2], A. Sydorenko[97], I. Sykora[28a], M. Sykora[140], T. Sykora[140], D. Ta[97], K. Tackmann[44,aa], J. Taenzer[158], A. Taffard[168], R. Tafirout[165a], E. Tahirovic[90], N. Taiblum[158], H. Takai[29], R. Takashima[84], E. H. Takasugi[113], K. Takeda[80], T. Takeshita[147], Y. Takubo[79], M. Talby[99], A. A. Talyshev[120a,120b], J. Tanaka[160], M. Tanaka[162], R. Tanaka[129], B. B. Tannenwald[123], S. Tapia Araya[144b], S. Tapprogge[97], A. Tarek Abouelfadl Mohamed[133], S. Tarem[157], G. Tarna[27b,e], G. F. Tartarelli[66a], P. Tas[140], M. Tasevsky[138], T. Tashiro[83], E. Tassi[40b,40a], A. Tavares Delgado[137a,137b], Y. Tayalati[34e], A. C. Taylor[116], A. J. Taylor[48], G. N. Taylor[102], P. T. E. Taylor[102], W. Taylor[165b], A. S. Tee[87],

R. Teixeira De Lima[150], P. Teixeira-Dias[91], H. Ten Kate[35], J. J. Teoh[118], S. Terada[79], K. Terashi[160], J. Terron[96], S. Terzo[14], M. Testa[49], R. J. Teuscher[164,ad], S. J. Thais[180], T. Theveneaux-Pelzer[44], F. Thiele[39], D. W. Thomas[91], J. P. Thomas[21], A. S. Thompson[55], P. D. Thompson[21], L. A. Thomsen[180], E. Thomson[134], Y. Tian[38], R. E. Ticse Torres[51], V. O. Tikhomirov[108,ap], Yu. A. Tikhonov[120a,120b], S. Timoshenko[110], P. Tipton[180], S. Tisserant[99], K. Todome[162], S. Todorova-Nova[5], S. Todt[46], J. Tojo[85], S. Tokár[28a], K. Tokushuku[79], E. Tolley[123], K. G. Tomiwa[32c], M. Tomoto[115], L. Tompkins[150,r], K. Toms[116], B. Tong[57], P. Tornambe[50], E. Torrence[128], H. Torres[46], E. Torró Pastor[145], C. Tosciri[132], J. Toth[99,ac], F. Touchard[99], D. R. Tovey[146], C. J. Treado[122], T. Trefzger[174], F. Tresoldi[153], A. Tricoli[29], I. M. Trigger[165a], S. Trincaz-Duvoid[133], W. Trischuk[164], B. Trocmé[56], A. Trofymov[129], C. Troncon[66a], M. Trovatelli[173], F. Trovato[153], L. Truong[32b], M. Trzebinski[82], A. Trzupek[82], F. Tsai[44], J.C-L. Tseng[132], P. V. Tsiareshka[105,aj], A. Tsirigotis[159], N. Tsirintanis[9], V. Tsiskaridze[152], E. G. Tskhadadze[156a], I. I. Tsukerman[109], V. Tsulaia[18], S. Tsuno[79], D. Tsybychev[152,163], Y. Tu[61b], A. Tudorache[27b], V. Tudorache[27b], T. T. Tulbure[27a], A. N. Tuna[57], S. Turchikhin[77], D. Turgeman[177], I. Turk Cakir[4b,u], R. Turra[66a], P. M. Tuts[38], S Tzamarias[159], E. Tzovara[97], G. Ucchielli[45], I. Ueda[79], M. Ughetto[43a,43b], F. Ukegawa[166], G. Unal[35], A. Undrus[29], G. Unel[168], F. C. Ungaro[102], Y. Unno[79], K. Uno[160], J. Urban[28b], P. Urquijo[102], G. Usai[8], J. Usui[79], L. Vacavant[99], V. Vacek[139], B. Vachon[101], K. O. H. Vadla[131], A. Vaidya[92], C. Valderanis[112], E. Valdes Santurio[43a,43b], M. Valente[52], S. Valentinetti[23a,23b], A. Valero[171], L. Valéry[44], R. A. Vallance[21], A. Vallier[5], J. A. Valls Ferrer[171], T. R. Van Daalen[14], H. Van der Graaf[118], P. Van Gemmeren[6], I. Van Vulpen[118], M. Vanadia[71a,71b], W. Vandelli[35], A. Vaniachine[163], P. Vankov[118], R. Vari[70a], E. W. Varnes[7], C. Varni[53a,53b], T. Varol[41], D. Varouchas[129], K. E. Varvell[154], G. A. Vasquez[144b], J. G. Vasquez[180], F. Vazeille[37], D. Vazquez Furelos[14], T. Vazquez Schroeder[35], J. Veatch[51], V. Vecchio[72a,72b], L. M. Veloce[164], F. Veloso[137a,137c], S. Veneziano[70a], A. Ventura[65a,65b], N. Venturi[35], V. Vercesi[68a], M. Verducci[72a,72b], C. M. Vergel Infante[76], C. Vergis[24], W. Verkerke[118], A. T. Vermeulen[118], J. C. Vermeulen[118], M. C. Vetterli[149,av], N. Viaux Maira[144b], M. Vicente Barreto Pinto[52], I. Vichou[170,*], T. Vickey[146], O. E. Vickey Boeriu[146], G. H. A. Viehhauser[132], S. Viel[18], L. Vigani[132], M. Villa[23a,23b], M. Villaplana Perez[66a,66b], E. Vilucchi[49], M. G. Vincter[33], V. B. Vinogradov[77], A. Vishwakarma[44], C. Vittori[23a,23b], I. Vivarelli[153], S. Vlachos[10], M. Vogel[179], P. Vokac[139], G. Volpi[14], S. E. von Buddenbrock[32c], E. Von Toerne[24], V. Vorobel[140], K. Vorobev[110], M. Vos[171], J. H. Vossebeld[88], N. Vranjes[16], M. Vranjes Milosavljevic[16], V. Vrba[139], M. Vreeswijk[118], T. Šfiligoj[89], R. Vuillermet[35], I. Vukotic[36], T. Ženiš[28a], L. Živković[16], P. Wagner[24], W. Wagner[179], J. Wagner-Kuhr[112], H. Wahlberg[86], S. Wahrmund[46], K. Wakamiya[80], V. M. Walbrecht[113], J. Walder[87], R. Walker[112], S. D. Walker[91], W. Walkowiak[148], V. Wallangen[43a,43b], A. M. Wang[57], C. Wang[58b], F. Wang[178], H. Wang[18], H. Wang[3], J. Wang[154], J. Wang[59b], P. Wang[41], Q. Wang[125], R.-J. Wang[133], R. Wang[58a], R. Wang[6], S. M. Wang[155], W. T. Wang[58a], W. Wang[15c,ae], W. X. Wang[58a,ae], Y. Wang[58a,am], Z. Wang[58c], C. Wanotayaroj[44], A. Warburton[101], C. P. Ward[31], D. R. Wardrope[92], A. Washbrook[48], P. M. Watkins[21], A. T. Watson[21], M. F. Watson[21], G. Watts[145], S. Watts[98], B. M. Waugh[92], A. F. Webb[11], S. Webb[97], C. Weber[180], M. S. Weber[20], S. A. Weber[33], S. M. Weber[59a], A. R. Weidberg[132], J. Weingarten[45], M. Weirich[97], C. Weiser[50], P. S. Wells[35], T. Wenaus[29], T. Wengler[35], S. Wenig[35], N. Wermes[24], M. D. Werner[76], P. Werner[35], M. Wessels[59a], T. D. Weston[20], K. Whalen[128], N. L. Whallon[145], A. M. Wharton[87], A. S. White[103], A. White[8], M. J. White[1], R. White[144b], D. Whiteson[168], B. W. Whitmore[87], F. J. Wickens[141], W. Wiedenmann[178], M. Wielers[141], C. Wiglesworth[39], L. A. M. Wiik-Fuchs[50], F. Wilk[98], H. G. Wilkens[35], L. J. Wilkins[91], H. H. Williams[134], S. Williams[31], C. Willis[104], S. Willocq[100], J. A. Wilson[21], I. Wingerter-Seez[5], E. Winkels[153], F. Winklmeier[128], O. J. Winston[153], B. T. Winter[50], M. Wittgen[150], M. Wobisch[93], A. Wolf[97], T. M. H. Wolf[118], R. Wolff[99], J. Wollrath[50], M. W. Wolter[82], H. Wolters[137a,137c], V. W. S. Wong[172], N. L. Woods[143], S. D. Worm[21], B. K. Wosiek[82], K. W. Woźniak[82], K. Wraight[55], M. Wu[36], S. L. Wu[178], X. Wu[52], Y. Wu[58a], T. R. Wyatt[98], B. M. Wynne[48], S. Xella[39], Z. Xi[103], L. Xia[175], D. Xu[15a], H. Xu[58a,e], L. Xu[29], T. Xu[142], W. Xu[103], Z. Xu[150], B. Yabsley[154], S. Yacoob[32a], K. Yajima[130], D. P. Yallup[92], D. Yamaguchi[162], Y. Yamaguchi[162], A. Yamamoto[79], T. Yamanaka[160], F. Yamane[80], M. Yamatani[160], T. Yamazaki[160], Y. Yamazaki[80], Z. Yan[25], H. J. Yang[58c,58d], H. T. Yang[18], S. Yang[75], Y. Yang[160], Z. Yang[17], W-M. Yao[18], Y. C. Yap[44], Y. Yasu[79], E. Yatsenko[58c,58d], J. Ye[41], S. Ye[29], I. Yeletskikh[77], E. Yigitbasi[25], E. Yildirim[97], K. Yorita[176], K. Yoshihara[134], C. J. S. Young[35], C. Young[150], J. Yu[8], J. Yu[76], X. Yue[59a], S. P. Y. Yuen[24], B. Zabinski[82], G. Zacharis[10], E. Zaffaroni[52], R. Zaidan[14], A. M. Zaitsev[121,ao], T. Zakareishvili[156b], N. Zakharchuk[33], S. Zambito[57], D. Zanzi[35], D. R. Zaripovas[55], S. V. Zeißner[45], C. Zeitnitz[179], G. Zemaityte[132], J. C. Zeng[170], Q. Zeng[150], O. Zenin[121], D. Zerwas[129], M. Zgubič[132], D. F. Zhang[58b], D. Zhang[103], F. Zhang[178], G. Zhang[58a], G. Zhang[15b], H. Zhang[15c], J. Zhang[6], L. Zhang[15c], L. Zhang[58a], M. Zhang[170], P. Zhang[15c], R. Zhang[58a], R. Zhang[24], X. Zhang[58b], Y. Zhang[15d], Z. Zhang[129], P. Zhao[47], Y. Zhao[58b,129,ak], Z. Zhao[58a], A. Zhemchugov[77], Z. Zheng[103], D. Zhong[170], B. Zhou[103], C. Zhou[178], M. S. Zhou[15d], M. Zhou[152], N. Zhou[58c], Y. Zhou[7], C. G. Zhu[58b], H. L. Zhu[58a], H. Zhu[15a], J. Zhu[103], Y. Zhu[58a], X. Zhuang[15a], K. Zhukov[108], V. Zhulanov[120a,120b], A. Zibell[174], D. Zieminska[63], N. I. Zimine[77], S. Zimmermann[50], Z. Zinonos[113], M. Ziolkowski[148], G. Zobernig[178], A. Zoccoli[23a,23b], K. Zoch[51], T. G. Zorbas[146], R. Zou[36], M. Zur Nedden[19], L. Zwalinski[35]

[1] Department of Physics, University of Adelaide, Adelaide, Australia
[2] Physics Department, SUNY Albany, Albany, NY, USA
[3] Department of Physics, University of Alberta, Edmonton, AB, Canada
[4] [(a)]Department of Physics, Ankara University, Ankara, Turkey; [(b)]Istanbul Aydin University, Istanbul, Turkey; [(c)]Division of Physics, TOBB University of Economics and Technology, Ankara, Turkey
[5] LAPP, Université Grenoble Alpes, Université Savoie Mont Blanc, CNRS/IN2P3, Annecy, France
[6] High Energy Physics Division, Argonne National Laboratory, Argonne, IL, USA
[7] Department of Physics, University of Arizona, Tucson, AZ, USA
[8] Department of Physics, University of Texas at Arlington, Arlington, TX, USA
[9] Physics Department, National and Kapodistrian University of Athens, Athens, Greece
[10] Physics Department, National Technical University of Athens, Zografou, Greece
[11] Department of Physics, University of Texas at Austin, Austin, TX, USA
[12] [(a)]Bahcesehir University, Faculty of Engineering and Natural Sciences, Istanbul, Turkey; [(b)]Istanbul Bilgi University, Faculty of Engineering and Natural Sciences, Istanbul, Turkey; [(c)]Department of Physics, Bogazici University, Istanbul, Turkey; [(d)]Department of Physics Engineering, Gaziantep University, Gaziantep, Turkey
[13] Institute of Physics, Azerbaijan Academy of Sciences, Baku, Azerbaijan
[14] Institut de Física d'Altes Energies (IFAE), Barcelona Institute of Science and Technology, Barcelona, Spain
[15] [(a)]Institute of High Energy Physics, Chinese Academy of Sciences, Beijing, China; [(b)]Physics Department, Tsinghua University, Beijing, China; [(c)]Department of Physics, Nanjing University, Nanjing, China; [(d)]University of Chinese Academy of Science (UCAS), Beijing, China
[16] Institute of Physics, University of Belgrade, Belgrade, Serbia
[17] Department for Physics and Technology, University of Bergen, Bergen, Norway
[18] Physics Division, Lawrence Berkeley National Laboratory and University of California, Berkeley, CA, USA
[19] Institut für Physik, Humboldt Universität zu Berlin, Berlin, Germany
[20] Albert Einstein Center for Fundamental Physics and Laboratory for High Energy Physics, University of Bern, Bern, Switzerland
[21] School of Physics and Astronomy, University of Birmingham, Birmingham, UK
[22] Centro de Investigaciónes, Universidad Antonio Nariño, Bogota, Colombia
[23] [(a)]Dipartimento di Fisica e Astronomia, Università di Bologna, Bologna, Italy; [(b)]INFN Sezione di Bologna, Bologna, Italy
[24] Physikalisches Institut, Universität Bonn, Bonn, Germany
[25] Department of Physics, Boston University, Boston, MA, USA
[26] Department of Physics, Brandeis University, Waltham, MA, USA
[27] [(a)]Transilvania University of Brasov, Brasov, Romania; [(b)]Horia Hulubei National Institute of Physics and Nuclear Engineering, Bucharest, Romania; [(c)]Department of Physics, Alexandru Ioan Cuza University of Iasi, Iasi, Romania; [(d)]National Institute for Research and Development of Isotopic and Molecular Technologies, Physics Department, Cluj-Napoca, Romania; [(e)]University Politehnica Bucharest, Bucharest, Romania; [(f)]West University in Timisoara, Timisoara, Romania
[28] [(a)]Faculty of Mathematics, Physics and Informatics, Comenius University, Bratislava, Slovak Republic; [(b)]Department of Subnuclear Physics, Institute of Experimental Physics of the Slovak Academy of Sciences, Kosice, Slovak Republic
[29] Physics Department, Brookhaven National Laboratory, Upton, NY, USA
[30] Departamento de Física, Universidad de Buenos Aires, Buenos Aires, Argentina
[31] Cavendish Laboratory, University of Cambridge, Cambridge, UK
[32] [(a)]Department of Physics, University of Cape Town, Cape Town, South Africa; [(b)]Department of Mechanical Engineering Science, University of Johannesburg, Johannesburg, South Africa; [(c)]School of Physics, University of the Witwatersrand, Johannesburg, South Africa
[33] Department of Physics, Carleton University, Ottawa, ON, Canada
[34] [(a)]Faculté des Sciences Ain Chock, Réseau Universitaire de Physique des Hautes Energies-Université Hassan II, Casablanca, Morocco; [(b)]Centre National de l'Energie des Sciences Techniques Nucleaires (CNESTEN), Rabat, Morocco; [(c)]Faculté des Sciences Semlalia, Université Cadi Ayyad, LPHEA-Marrakech, Morocco; [(d)]Faculté des Sciences, Université Mohamed Premier and LPTPM, Oujda, Morocco; [(e)]Faculté des sciences, Université Mohammed V, Rabat, Morocco
[35] CERN, Geneva, Switzerland

[36] Enrico Fermi Institute, University of Chicago, Chicago, IL, USA
[37] LPC, Université Clermont Auvergne, CNRS/IN2P3, Clermont-Ferrand, France
[38] Nevis Laboratory, Columbia University, Irvington, NY, USA
[39] Niels Bohr Institute, University of Copenhagen, Copenhagen, Denmark
[40] [(a)]Dipartimento di Fisica, Università della Calabria, Rende, Italy; [(b)]INFN Gruppo Collegato di Cosenza, Laboratori Nazionali di Frascati, Italy
[41] Physics Department, Southern Methodist University, Dallas, TX, USA
[42] Physics Department, University of Texas at Dallas, Richardson, TX, USA
[43] [(a)]Department of Physics, Stockholm University, Sweden; [(b)]Oskar Klein Centre, Stockholm, Sweden
[44] Deutsches Elektronen-Synchrotron DESY, Hamburg and Zeuthen, Germany
[45] Lehrstuhl für Experimentelle Physik IV, Technische Universität Dortmund, Dortmund, Germany
[46] Institut für Kern- und Teilchenphysik, Technische Universität Dresden, Dresden, Germany
[47] Department of Physics, Duke University, Durham, NC, USA
[48] SUPA-School of Physics and Astronomy, University of Edinburgh, Edinburgh, UK
[49] INFN e Laboratori Nazionali di Frascati, Frascati, Italy
[50] Physikalisches Institut, Albert-Ludwigs-Universität Freiburg, Freiburg, Germany
[51] II. Physikalisches Institut, Georg-August-Universität Göttingen, Göttingen, Germany
[52] Département de Physique Nucléaire et Corpusculaire, Université de Genève, Genève, Switzerland
[53] [(a)]Dipartimento di Fisica, Università di Genova, Genova, Italy; [(b)]INFN Sezione di Genova, Genoa, Italy
[54] II. Physikalisches Institut, Justus-Liebig-Universität Giessen, Giessen, Germany
[55] SUPA-School of Physics and Astronomy, University of Glasgow, Glasgow, UK
[56] LPSC, Université Grenoble Alpes, CNRS/IN2P3, Grenoble INP, Grenoble, France
[57] Laboratory for Particle Physics and Cosmology, Harvard University, Cambridge, MA, USA
[58] [(a)]Department of Modern Physics and State Key Laboratory of Particle Detection and Electronics, University of Science and Technology of China, Hefei, China; [(b)]Institute of Frontier and Interdisciplinary Science and Key Laboratory of Particle Physics and Particle Irradiation (MOE), Shandong University, Qingdao, China; [(c)]School of Physics and Astronomy, Shanghai Jiao Tong University, KLPPAC-MoE, SKLPPC, Shanghai, China; [(d)]Tsung-Dao Lee Institute, Shanghai, China
[59] [(a)]Kirchhoff-Institut für Physik, Ruprecht-Karls-Universität Heidelberg, Heidelberg, Germany; [(b)]Physikalisches Institut, Ruprecht-Karls-Universität Heidelberg, Heidelberg, Germany
[60] Faculty of Applied Information Science, Hiroshima Institute of Technology, Hiroshima, Japan
[61] [(a)]Department of Physics, Chinese University of Hong Kong, Shatin, N.T., Hong Kong, China; [(b)]Department of Physics, University of Hong Kong, Hong Kong, China; [(c)]Department of Physics and Institute for Advanced Study, Hong Kong University of Science and Technology, Clear Water Bay, Kowloon, Hong Kong, China
[62] Department of Physics, National Tsing Hua University, Hsinchu, Taiwan
[63] Department of Physics, Indiana University, Bloomington, IN, USA
[64] [(a)]INFN Gruppo Collegato di Udine, Sezione di Trieste, Udine, Italy; [(b)]ICTP, Trieste, Italy; [(c)]Dipartimento di Chimica, Fisica e Ambiente, Università di Udine, Udine, Italy
[65] [(a)]INFN Sezione di Lecce, Zona Monte, Italy; [(b)]Dipartimento di Matematica e Fisica, Università del Salento, Lecce, Italy
[66] [(a)]INFN Sezione di Milano, Milan, Italy; [(b)]Dipartimento di Fisica, Università di Milano, Milano, Italy
[67] [(a)]INFN Sezione di Napoli, Naples, Italy; [(b)]Dipartimento di Fisica, Università di Napoli, Napoli, Italy
[68] [(a)]INFN Sezione di Pavia, Pavia, Italy; [(b)]Dipartimento di Fisica, Università di Pavia, Pavia, Italy
[69] [(a)]INFN Sezione di Pisa, Pisa, Italy; [(b)]Dipartimento di Fisica E. Fermi, Università di Pisa, Pisa, Italy
[70] [(a)]INFN Sezione di Roma, Rome, Italy; [(b)]Dipartimento di Fisica, Sapienza Università di Roma, Roma, Italy
[71] [(a)]INFN Sezione di Roma, Tor Vergata, Italy; [(b)]Dipartimento di Fisica, Università di Roma Tor Vergata, Roma, Italy
[72] [(a)]INFN Sezione di Roma Tre, Rome, Italy; [(b)]Dipartimento di Matematica e Fisica, Università Roma Tre, Roma, Italy
[73] [(a)]INFN-TIFPA, Povo, Italy; [(b)]Università degli Studi di Trento, Trento, Italy
[74] Institut für Astro- und Teilchenphysik, Leopold-Franzens-Universität, Innsbruck, Austria
[75] University of Iowa, Iowa City, IA, USA
[76] Department of Physics and Astronomy, Iowa State University, Ames, IA, USA
[77] Joint Institute for Nuclear Research, Dubna, Russia

[78] [(a)]Departamento de Engenharia Elétrica, Universidade Federal de Juiz de Fora (UFJF), Juiz de Fora, Brazil; [(b)]Universidade Federal do Rio De Janeiro COPPE/EE/IF, Rio de Janeiro, Brazil; [(c)]Universidade Federal de São João del Rei (UFSJ), São João del Rei, Brazil; [(d)]Instituto de Física, Universidade de São Paulo, São Paulo, Brazil
[79] KEK, High Energy Accelerator Research Organization, Tsukuba, Japan
[80] Graduate School of Science, Kobe University, Kobe, Japan
[81] [(a)]AGH University of Science and Technology, Faculty of Physics and Applied Computer Science, Krakow, Poland; [(b)]Marian Smoluchowski Institute of Physics, Jagiellonian University, Krakow, Poland
[82] Institute of Nuclear Physics Polish Academy of Sciences, Krakow, Poland
[83] Faculty of Science, Kyoto University, Kyoto, Japan
[84] Kyoto University of Education, Kyoto, Japan
[85] Research Center for Advanced Particle Physics and Department of Physics, Kyushu University, Fukuoka , Japan
[86] Instituto de Física La Plata, Universidad Nacional de La Plata and CONICET, La Plata, Argentina
[87] Physics Department, Lancaster University, Lancaster, UK
[88] Oliver Lodge Laboratory, University of Liverpool, Liverpool, UK
[89] Department of Experimental Particle Physics, Jožef Stefan Institute and Department of Physics, University of Ljubljana, Ljubljana, Slovenia
[90] School of Physics and Astronomy, Queen Mary University of London, London, UK
[91] Department of Physics, Royal Holloway University of London, Egham, UK
[92] Department of Physics and Astronomy, University College London, London, UK
[93] Louisiana Tech University, Ruston, LA, USA
[94] Fysiska institutionen, Lunds universitet, Lund, Sweden
[95] Centre de Calcul de l'Institut National de Physique Nucléaire et de Physique des Particules (IN2P3), Villeurbanne, France
[96] Departamento de Física Teorica C-15 and CIAFF, Universidad Autónoma de Madrid, Madrid, Spain
[97] Institut für Physik, Universität Mainz, Mainz, Germany
[98] School of Physics and Astronomy, University of Manchester, Manchester, UK
[99] CPPM, Aix-Marseille Université, CNRS/IN2P3, Marseille, France
[100] Department of Physics, University of Massachusetts, Amherst, MA, USA
[101] Department of Physics, McGill University, Montreal, QC, Canada
[102] School of Physics, University of Melbourne, Victoria, Australia
[103] Department of Physics, University of Michigan, Ann Arbor, MI, USA
[104] Department of Physics and Astronomy, Michigan State University, East Lansing, MI, USA
[105] B.I. Stepanov Institute of Physics, National Academy of Sciences of Belarus, Minsk, Belarus
[106] Research Institute for Nuclear Problems of Byelorussian State University, Minsk, Belarus
[107] Group of Particle Physics, University of Montreal, Montreal, QC, Canada
[108] P.N. Lebedev Physical Institute of the Russian Academy of Sciences, Moscow, Russia
[109] Institute for Theoretical and Experimental Physics (ITEP), Moscow, Russia
[110] National Research Nuclear University MEPhI, Moscow, Russia
[111] D.V. Skobeltsyn Institute of Nuclear Physics, M.V. Lomonosov Moscow State University, Moscow, Russia
[112] Fakultät für Physik, Ludwig-Maximilians-Universität München, München, Germany
[113] Max-Planck-Institut für Physik (Werner-Heisenberg-Institut), München, Germany
[114] Nagasaki Institute of Applied Science, Nagasaki, Japan
[115] Graduate School of Science and Kobayashi-Maskawa Institute, Nagoya University, Nagoya, Japan
[116] Department of Physics and Astronomy, University of New Mexico, Albuquerque, NM, USA
[117] Institute for Mathematics, Astrophysics and Particle Physics, Radboud University Nijmegen/Nikhef, Nijmegen, The Netherlands
[118] Nikhef National Institute for Subatomic Physics and University of Amsterdam, Amsterdam, The Netherlands
[119] Department of Physics, Northern Illinois University, DeKalb, IL, USA
[120] [(a)]Budker Institute of Nuclear Physics and NSU, SB RAS, Novosibirsk, Russia; [(b)]Novosibirsk State University Novosibirsk, Novosibirsk, Russia
[121] Institute for High Energy Physics of the National Research Centre Kurchatov Institute, Protvino, Russia
[122] Department of Physics, New York University, New York, NY, USA
[123] Ohio State University, Columbus, OH, USA

[124] Faculty of Science, Okayama University, Okayama, Japan
[125] Homer L. Dodge Department of Physics and Astronomy, University of Oklahoma, Norman, OK, USA
[126] Department of Physics, Oklahoma State University, Stillwater, OK, USA
[127] Palacký University, RCPTM, Joint Laboratory of Optics, Olomouc, Czech Republic
[128] Center for High Energy Physics, University of Oregon, Eugene, OR, USA
[129] LAL, Université Paris-Sud, CNRS/IN2P3, Université Paris-Saclay, Orsay, France
[130] Graduate School of Science, Osaka University, Osaka, Japan
[131] Department of Physics, University of Oslo, Oslo, Norway
[132] Department of Physics, Oxford University, Oxford, UK
[133] LPNHE, Sorbonne Université, Paris Diderot Sorbonne Paris Cité, CNRS/IN2P3, Paris, France
[134] Department of Physics, University of Pennsylvania, Philadelphia, PA, USA
[135] Konstantinov Nuclear Physics Institute of National Research Centre "Kurchatov Institute", PNPI, St. Petersburg, Russia
[136] Department of Physics and Astronomy, University of Pittsburgh, Pittsburgh, PA, USA
[137] [(a)]Laboratório de Instrumentação e Física Experimental de Partículas-LIP, Lisbon, Portugal; [(b)]Departamento de Física, Faculdade de Ciências, Universidade de Lisboa, Lisboa, Portugal; [(c)]Departamento de Física, Universidade de Coimbra, Coimbra, Portugal; [(d)]Centro de Física Nuclear da Universidade de Lisboa, Lisboa, Portugal; [(e)]Departamento de Física, Universidade do Minho, Braga, Portugal; [(f)]Departamento de Física Teorica y del Cosmos, Universidad de Granada, Granada (Spain), Portugal; [(g)]Dep Física and CEFITEC of Faculdade de Ciências e Tecnologia, Universidade Nova de Lisboa, Caparica, Portugal
[138] Institute of Physics, Academy of Sciences of the Czech Republic, Prague, Czech Republic
[139] Czech Technical University in Prague, Prague, Czech Republic
[140] Charles University, Faculty of Mathematics and Physics, Prague, Czech Republic
[141] Particle Physics Department, Rutherford Appleton Laboratory, Didcot, UK
[142] IRFU, CEA, Université Paris-Saclay, Gif-sur-Yvette, France
[143] Santa Cruz Institute for Particle Physics, University of California Santa Cruz, Santa Cruz, CA, USA
[144] [(a)]Departamento de Física, Pontificia Universidad Católica de Chile, Santiago, Chile; [(b)]Departamento de Física, Universidad Técnica Federico Santa María, Valparaíso, Chile
[145] Department of Physics, University of Washington, Seattle, WA, USA
[146] Department of Physics and Astronomy, University of Sheffield, Sheffield, UK
[147] Department of Physics, Shinshu University, Nagano, Japan
[148] Department Physik, Universität Siegen, Siegen, Germany
[149] Department of Physics, Simon Fraser University, Burnaby, BC, Canada
[150] SLAC National Accelerator Laboratory, Stanford, CA, USA
[151] Physics Department, Royal Institute of Technology, Stockholm, Sweden
[152] Departments of Physics and Astronomy, Stony Brook University, Stony Brook, NY, USA
[153] Department of Physics and Astronomy, University of Sussex, Brighton, UK
[154] School of Physics, University of Sydney, Sydney, Australia
[155] Institute of Physics, Academia Sinica, Taipei, Taiwan
[156] [(a)]E. Andronikashvili Institute of Physics, Iv. Javakhishvili Tbilisi State University, Tbilisi, Georgia; [(b)]High Energy Physics Institute, Tbilisi State University, Tbilisi, Georgia
[157] Department of Physics, Technion, Israel Institute of Technology, Haifa, Israel
[158] Raymond and Beverly Sackler School of Physics and Astronomy, Tel Aviv University, Tel Aviv, Israel
[159] Department of Physics, Aristotle University of Thessaloniki, Thessaloniki, Greece
[160] International Center for Elementary Particle Physics and Department of Physics, University of Tokyo, Tokyo, Japan
[161] Graduate School of Science and Technology, Tokyo Metropolitan University, Tokyo, Japan
[162] Department of Physics, Tokyo Institute of Technology, Tokyo, Japan
[163] Tomsk State University, Tomsk, Russia
[164] Department of Physics, University of Toronto, Toronto, ON, Canada
[165] [(a)]TRIUMF, Vancouver, BC, Canada; [(b)]Department of Physics and Astronomy, York University, Toronto, ON, Canada
[166] Division of Physics and Tomonaga Center for the History of the Universe, Faculty of Pure and Applied Sciences, University of Tsukuba, Tsukuba, Japan
[167] Department of Physics and Astronomy, Tufts University, Medford, MA, USA
[168] Department of Physics and Astronomy, University of California Irvine, Irvine, CA, USA

[169] Department of Physics and Astronomy, University of Uppsala, Uppsala, Sweden
[170] Department of Physics, University of Illinois, Urbana, IL, USA
[171] Instituto de Física Corpuscular (IFIC), Centro Mixto Universidad de Valencia-CSIC, Valencia, Spain
[172] Department of Physics, University of British Columbia, Vancouver, BC, Canada
[173] Department of Physics and Astronomy, University of Victoria, Victoria, BC, Canada
[174] Fakultät für Physik und Astronomie, Julius-Maximilians-Universität Würzburg, Würzburg, Germany
[175] Department of Physics, University of Warwick, Coventry, UK
[176] Waseda University, Tokyo, Japan
[177] Department of Particle Physics, Weizmann Institute of Science, Rehovot, Israel
[178] Department of Physics, University of Wisconsin, Madison, WI, USA
[179] Fakultät für Mathematik und Naturwissenschaften, Fachgruppe Physik, Bergische Universität Wuppertal, Wuppertal, Germany
[180] Department of Physics, Yale University, New Haven, CT, USA
[181] Yerevan Physics Institute, Yerevan, Armenia

[a] Also at Borough of Manhattan Community College, City University of New York, NY, USA
[b] Also at California State University, East Bay, USA
[c] Also at Centre for High Performance Computing, CSIR Campus, Rosebank, Cape Town, South Africa
[d] Also at CERN, Geneva, Switzerland
[e] Also at CPPM, Aix-Marseille Université, CNRS/IN2P3, Marseille, France
[f] Also at Département de Physique Nucléaire et Corpusculaire, Université de Genève, Genève, Switzerland
[g] Also at Departament de Fisica de la Universitat Autonoma de Barcelona, Barcelona, Spain
[h] Also at Departamento de Física Teorica y del Cosmos, Universidad de Granada, Granada (Spain), Spain
[i] Also at Departamento de Física, Instituto Superior Técnico, Universidade de Lisboa, Lisboa, Portugal
[j] Also at Department of Applied Physics and Astronomy, University of Sharjah, Sharjah, United Arab Emirates
[k] Also at Department of Financial and Management Engineering, University of the Aegean, Chios, Greece
[l] Also at Department of Physics and Astronomy, University of Louisville, Louisville, KY, USA
[m] Also at Department of Physics and Astronomy, University of Sheffield, Sheffield, UK
[n] Also at Department of Physics, California State University, Fresno CA, USA
[o] Also at Department of Physics, California State University, Sacramento CA, USA
[p] Also at Department of Physics, King's College London, London, UK
[q] Also at Department of Physics, St. Petersburg State Polytechnical University, St. Petersburg, Russia
[r] Also at Department of Physics, Stanford University, USA
[s] Also at Department of Physics, University of Fribourg, Fribourg, Switzerland
[t] Also at Department of Physics, University of Michigan, Ann Arbor MI, USA
[u] Also at Giresun University, Faculty of Engineering, Giresun, Turkey
[v] Also at Graduate School of Science, Osaka University, Osaka, Japan
[w] Also at Hellenic Open University, Patras, Greece
[x] Also at Horia Hulubei National Institute of Physics and Nuclear Engineering, Bucharest, Romania
[y] Also at II. Physikalisches Institut, Georg-August-Universität Göttingen, Göttingen, Germany
[z] Also at Institucio Catalana de Recerca i Estudis Avancats, ICREA, Barcelona, Spain
[aa] Also at Institut für Experimentalphysik, Universität Hamburg, Hamburg, Germany
[ab] Also at Institute for Mathematics, Astrophysics and Particle Physics, Radboud University Nijmegen/Nikhef, Nijmegen, The Netherlands
[ac] Also at Institute for Particle and Nuclear Physics, Wigner Research Centre for Physics, Budapest, Hungary
[ad] Also at Institute of Particle Physics (IPP), Canada
[ae] Also at Institute of Physics, Academia Sinica, Taipei, Taiwan
[af] Also at Institute of Physics, Azerbaijan Academy of Sciences, Baku, Azerbaijan
[ag] Also at Institute of Theoretical Physics, Ilia State University, Tbilisi, Georgia
[ah] Also at Instituto de Física Teórica de la Universidad Autónoma de Madrid, Spain
[ai] Also at Istanbul University, Dept. of Physics, Istanbul, Turkey
[aj] Also at Joint Institute for Nuclear Research, Dubna, Russia
[ak] Also at LAL, Université Paris-Sud, CNRS/IN2P3, Université Paris-Saclay, Orsay, France

[al] Also at Louisiana Tech University, Ruston LA, USA
[am] Also at LPNHE, Sorbonne Université, Paris Diderot Sorbonne Paris Cité, CNRS/IN2P3, Paris, France
[an] Also at Manhattan College, New York NY, USA
[ao] Also at Moscow Institute of Physics and Technology State University, Dolgoprudny, Russia
[ap] Also at National Research Nuclear University MEPhI, Moscow, Russia
[aq] Also at Physikalisches Institut, Albert-Ludwigs-Universität Freiburg, Freiburg, Germany
[ar] Also at School of Physics, Sun Yat-sen University, Guangzhou, China
[as] Also at The City College of New York, New York NY, USA
[at] Also at The Collaborative Innovation Center of Quantum Matter (CICQM), Beijing, China
[au] Also at Tomsk State University, Tomsk, and Moscow Institute of Physics and Technology State University, Dolgoprudny, Russia
[av] Also at TRIUMF, Vancouver BC, Canada
[aw] Also at Universita di Napoli Parthenope, Napoli, Italy
*Deceased